

Higher-Order Electroweak Corrections to Dark Matter Direct Detection in the Dark Complex Scalar Extension of the Standard Model

Master Thesis
of

Tizian Marco Römer

at the Institute for Theoretical Physics (ITP)
of the Karlsruhe Institute of Technology (KIT)

Reviewer: Prof. Dr. M. M. Mühlleitner
Second Reviewer: Prof. Dr. U. Nierste
Advisor: M. Sc. Jonas Müller

Duration: June 01, 2019 – June 03, 2020

Declaration of Authorship

I hereby certify that the thesis I am submitting is entirely my own work except otherwise indicated. I am aware of the University's regulations concerning plagiarism, including those regulations concerning disciplinary actions that may result from plagiarism. Any use of the works of any other author, in any form, is properly acknowledged at their point of use.

Karlsruhe, June 03, 2020

Tizian Marco Römer

Accepted as Master Thesis

Karlsruhe, June 03, 2020

Prof. Dr. M. M. Mühlleitner

Contents

| | | |
|----------|---|-----------|
| 1 | Introduction | 1 |
| 2 | The Lagrangian and Parameters of the DCxSM | 3 |
| 3 | Dark Matter Direct Detection | 7 |
| 3.1 | Kinematics | 8 |
| 3.2 | The Detection Rate | 10 |
| 3.3 | The Cross Section | 11 |
| 3.4 | The Nucleon Cross Section in Effective Field Theory | 13 |
| 3.5 | Current Limits of Direct Detection Experiments | 16 |
| 3.6 | The Relic Abundance | 17 |
| 4 | Renormalization of the DCxSM | 19 |
| 4.1 | Principles of Regularization and Renormalization | 20 |
| 4.2 | Higgs Self-Energy | 25 |
| 4.3 | Tadpole Renormalization | 27 |
| 4.4 | Mixing Angle Renormalization | 31 |
| 4.5 | Renormalization of the Dark Matter Particle | 33 |
| 4.6 | χ^2 -Higgs Vertex Renormalization | 33 |
| 4.7 | Renormalization of Fermions | 34 |
| 4.8 | Renormalization of the Gauge Sector | 37 |
| 4.9 | $\bar{q}q$ -Higgs Vertex Renormalization | 43 |
| 4.10 | Overview: Counter Propagators and Vertices | 44 |
| 5 | The Amplitude of Dark Matter Direct Detection in the DCxSM | 49 |
| 5.1 | Tree Level | 49 |
| 5.2 | NLO Diagrams with External Quarks | 50 |
| 5.3 | NLO Diagrams with External Gluons | 54 |
| 5.4 | Matching the Amplitude to the Effective Operators | 64 |
| 6 | Numerical Analysis | 67 |
| 6.1 | Numerical Values of the Parameters | 67 |
| 6.2 | Parameter Scan | 68 |
| 6.3 | Behavior with Respect to Selected Parameters and Gauge Dependence | 71 |
| 7 | Conclusion | 75 |

| | |
|--|-----------|
| Appendix | 77 |
| A The Higgs Mass Mixing Angle | 77 |
| B Vanishing Propagator and Vertex Corrections | 79 |
| Glossary | 83 |
| List of Figures | 84 |
| List of Tables | 85 |
| List of Used Software | 86 |
| Bibliography | 87 |
| Acknowledgements | 94 |

CHAPTER 1

Introduction

By the end of the establishment of Quantum Mechanics during the first three decades of the 20th century, describing electromagnetic radiation in atoms within the framework of Quantum Mechanics required a formalism that was able to describe the creation and annihilation of particles as well as the interaction between electrons and photons. It was Paul Dirac who provided a first proper treatment of this problem in his paper *The Quantum Theory of the Emission and Absorption of Radiation* in 1927 [1]. By combining Quantum Mechanics, the Special Theory of Relativity as well as Classical Field Theory, Dirac, Pascual Jordan, Eugene Wigner and others laid the foundation for *Quantum Electrodynamics* (QED), the first kind of a *Quantum Field Theory* (QFT). It describes the electron and the photon as well as their interactions and naturally gives rise to the antiparticle of the electron, the positron [2].

The 1930s and 1940s were dominated by the challenge of handling the infinities which Robert Oppenheimer found to be a generic feature of computations for any higher-order correction to observables of QFTs [3]. The breakthrough came around 1950 with a series of papers by Richard Feynman, Julian Schwinger, Sin-Itiro Tomonaga and Freeman Dyson, in which the procedure of *renormalization* was developed to consistently cancel all infinities (see [4] and references therein).

In order to theoretically describe the experimentally established observations of the weak and the strong interaction, generalizations of QED were proposed, in particular theories with non-Abelian gauge symmetries. Until the early 1970s, this process had led to the discovery of the Electroweak Theory – describing the weak interaction by using the mechanism of symmetry breaking that gives rise to the Higgs boson [5–7] – as well as *Quantum Chromodynamics* (QCD), which describes the strong interaction between quarks. At the same time, also the *Standard Model of Elementary Particles* (SM) started taking shape [2].

Meanwhile, particle accelerators were constructed that allowed for the observation of particle collisions at higher and higher energies. Their findings accompanied the development of the theories or confirmed their predictions retrospectively. In this way, more and more new particles were experimentally discovered and appropriately built into the framework of the SM. Finally, with the discovery of the Higgs boson in 2012 at the Large Hadron Collider (LHC) at CERN, the last piece of the SM was experimentally confirmed [8, 9].

Together, QFT and the SM have been very successful in predicting experimental results to a high precision (see for example [10, 11]), yet there are still phenomena they cannot explain. One of the outstanding problems in modern physics is *Dark Matter* (DM).

In 1933, Fritz Zwicky used the virial theorem to determine the mass of the Coma galaxy cluster and was the first who found that the density of luminous matter is much smaller than the density of DM [12, 13]. Until today, by various methods, astronomers have found striking

evidence for the existence of considerable amounts of gravitationally interacting (i. e. massive) and non-luminous (i. e. electrically neutral) matter in the universe: Dark Matter. While in the early stages of DM research DM was mainly thought of as non-luminous ordinary matter, such as planets, nebulae or gases [13], these possibilities were eventually ruled out (see for example [14]). In the 1980s it became the leading paradigm that DM consists of non-baryonic particles [13]. However, the specific nature of DM remains unclear until today.

A promising DM candidate class is the *weakly interacting massive particle* (WIMP). In order to produce the observed DM relic abundance through the freeze-out mechanism, the DM particles must self-annihilate with a cross section σ of about $\langle\sigma v\rangle \sim 10^{-26} \text{ cm}^3\text{s}^{-1}$ [15], where v is the relative velocity of the annihilating particles and $\langle\cdot\rangle$ the thermal expectation value. The fact that this order of magnitude corresponds to the cross section of interactions transmitted by the weak force has been referred to as the *WIMP miracle* and serves as an excellent motivation for the study of WIMPs [13].

In order to incorporate such a DM candidate, the SM needs to be extended. The Higgs potential of the weak sector of the SM Lagrangian is so far experimentally only weakly constrained and extending it leads to a rich spectrum of phenomenological characteristics [16].

In this work, a specific minimal extension of the SM is studied, the *Dark Complex Scalar Extension of the Standard Model* (DCxSM), in which a new complex singlet is added to the Higgs sector of the SM Lagrangian, which – after electroweak symmetry breaking – gives rise to a scalar field describing a DM particle candidate [17]. For this candidate, the spin-independent cross section for DM Direct Detection experiments is computed, which aim for detecting the scattering of a DM particle with a nucleus from some target material. Since the tree-level contribution to this cross section vanishes in the non-relativistic limit (see Sec. 5.1), higher-order corrections have to be taken into account.

The DCxSM is introduced in Chapter 2. In Chapter 3, an overview over the experiments that have been and are currently conducted to detect DM is provided, focusing in particular on DM Direct Detection experiments, for which the kinematics and the connection between experimental measurements and theoretical calculations is presented in detail. The renormalization of DCxSM, which is required for the higher-order calculations, is presented in Chapter 4. In Chapter 5 it is explained which diagrams are taken into account and which techniques have been applied to compute them. Finally, the results are analyzed and compared to current experimental exclusion limits in Chapter 6, and in Chapter 7 the work and the results are summarized.

CHAPTER 2

The Lagrangian and Parameters of the DCxSM

In this chapter the *Dark Complex Scalar Extension of the Standard Model* (DCxSM) is introduced. The DCxSM is a modification of the SM that exclusively affects the Higgs sector, where a new complex scalar field S is added as a singlet under the gauge group. Being a singlet, it comes with the kinetic term $|\partial^\mu S|^2$, which does not contain a covariant derivative, and therefore S does not couple to any gauge bosons.

The Higgs sector potential in the DCxSM is given by [17]

$$V = -\frac{\mu_H^2}{2}|H|^2 + \frac{\lambda_H}{2}|H|^4 - \frac{\mu_S^2}{2}|S|^2 + \frac{\lambda_S}{2}|S|^4 + \lambda_{HS}|H|^2|S|^2 - \frac{m_\chi^2}{4}(S^2 + S^{*2}). \quad (2.1)$$

Here, H is the SM Higgs doublet and the first two terms of V are precisely as in the SM. Adding the latter four terms yields the Higgs potential of the DCxSM. The DCxSM has a global $U(1)$ symmetry corresponding to the transformation $S \rightarrow e^{i\alpha}S$ that is softly broken by the last two terms of the potential (2.1).

For the potential to be stable (that is, to tend to plus infinity for $|H|, |S| \rightarrow \infty$), it is required that [18]

$$\lambda_H > 0, \quad \lambda_S > 0, \quad \lambda_{HS} > -\sqrt{\lambda_H \lambda_S}. \quad (2.2)$$

The vacuum expectation values (VEVs) of the fields H and S are chosen to be

$$\langle H \rangle = \frac{1}{\sqrt{2}} \begin{pmatrix} 0 \\ v \end{pmatrix}, \quad \langle S \rangle = \frac{v_S}{\sqrt{2}}, \quad (2.3)$$

with v and v_S being real and positive. By definition, the VEVs are minima of the potential and thus fulfill the *tadpole conditions*

$$\begin{aligned} \left. \frac{\partial V}{\partial H} \right|_{\text{VEV}} = 0 &\iff T_H \equiv \frac{v}{2} (-\mu_H^2 + \lambda_H v^2 + \lambda_{HS} v_S^2) = 0, \\ \left. \frac{\partial V}{\partial S} \right|_{\text{VEV}} = 0 &\iff T_S \equiv \frac{v_S}{2} (-\mu_S^2 + \lambda_S v_S^2 + \lambda_{HS} v^2 - m_\chi^2) = 0. \end{aligned} \quad (2.4)$$

The specification ‘‘VEV’’ in these equations means that H and S are replaced by their VEVs $\langle H \rangle$ and $\langle S \rangle$ from Eq. (2.3), respectively. As at higher-order in perturbation theory the tadpole parameters T_H and T_S need to be renormalized (see Sec. 4.3), which is why we will not set them to zero in the subsequent equations.

Expanding the fields H and S about their VEVs yields

$$H = \left(\begin{array}{c} G^+ \\ \frac{1}{\sqrt{2}} (v + \phi_H + iG^0) \end{array} \right), \quad S = \frac{1}{\sqrt{2}} (v_S + \phi_S + i\chi) \quad (2.5)$$

in terms of real fields ϕ_H , G^0 , ϕ_S and χ and a complex field G^+ . ϕ_H and ϕ_S are the Higgs boson fields in the gauge basis. G^+ and G^0 are the massless charged and neutral Goldstone bosons, respectively.

Plugging the expansion (2.5) into the potential (2.1) and using the definitions (2.4) to replace μ_H and μ_S by T_H , T_S , v and v_S , the potential becomes

$$V = V_0 + V_1 + V_2 + V_3 + V_4, \quad (2.6)$$

where

$$V_1 = T_H \phi_H + T_S \phi_S, \quad (2.7)$$

$$V_2 = \frac{1}{2} (\phi_H, \phi_S) \mathcal{M}_T^2 \begin{pmatrix} \phi_H \\ \phi_S \end{pmatrix} + \frac{1}{2} \left(m_\chi^2 + \frac{1}{v_S} T_S \right) \chi^2 + \frac{1}{v} T_H |G^+|^2 + \frac{1}{2v} T_H (G^0)^2, \quad (2.8)$$

$$V_3 = \frac{1}{2} (\lambda_H v \phi_H^3 + \lambda_S v_S \phi_S^3) + \frac{1}{2} \lambda_{HS} (v_S \phi_H^2 \phi_S + v \phi_H \phi_S^2 + v \phi_H \chi^2) + \frac{1}{2} \lambda_S v_S \phi_S \chi^2 + \frac{1}{2} (\lambda_H v \phi_H + \lambda_{HS} v_S \phi_S) (2|G^+|^2 + (G^0)^2), \quad (2.9)$$

$$V_4 = \frac{1}{8} (\lambda_H \phi_H^4 + \lambda_S \phi_S^4 + \lambda_S \chi^4 + 4\lambda_H |G^+|^4 + \lambda_H (G^0)^4) + \frac{1}{4} (\lambda_{HS} \phi_H^2 \phi_S^2 + \lambda_{HS} \phi_H^2 \chi^2 + \lambda_S \phi_S^2 \chi^2) + \frac{1}{4} (\lambda_H \phi_H^2 + \lambda_{HS} \phi_S^2 + \lambda_{HS} \chi^2) (2|G^+|^2 + (G^0)^2) + \frac{1}{2} \lambda_H |G^+|^2 (G^0)^2 \quad (2.10)$$

and V_0 contains all constant terms (without any fields). The squared mass matrix \mathcal{M}_T^2 in Eq. (2.8) is given by

$$\mathcal{M}_T^2 = \mathcal{M}^2 + \mathcal{T}, \quad \mathcal{M}^2 = \begin{pmatrix} \lambda_H v^2 & \lambda_{HS} v v_S \\ \lambda_{HS} v v_S & \lambda_S v_S^2 \end{pmatrix}, \quad \mathcal{T} = \begin{pmatrix} T_H/v & 0 \\ 0 & T_S/v_S \end{pmatrix}. \quad (2.11)$$

The matrix \mathcal{M}^2 can be diagonalized by an orthogonal matrix

$$R(\alpha) \equiv \begin{pmatrix} \cos \alpha & \sin \alpha \\ -\sin \alpha & \cos \alpha \end{pmatrix} \quad (2.12)$$

such that

$$M^2 \equiv R(\alpha) \mathcal{M}^2 R^{-1}(\alpha) = \begin{pmatrix} m_1^2 & 0 \\ 0 & m_2^2 \end{pmatrix}, \quad \begin{pmatrix} h_1 \\ h_2 \end{pmatrix} \equiv R(\alpha) \begin{pmatrix} \phi_H \\ \phi_S \end{pmatrix}, \quad (2.13)$$

where h_1 and h_2 are the Higgs mass eigenstates. The eigenvalues of \mathcal{M}^2 , i. e. the squared mass values of the Higgs mass eigenstates, are given by

$$m_{1,2}^2 = \frac{1}{2}\lambda_H v^2 + \frac{1}{2}\lambda_S v_S^2 \mp \frac{1}{2}\sqrt{(\lambda_H v^2 - \lambda_S v_S^2)^2 + (2\lambda_{HS} v v_S)^2}, \quad (2.14)$$

such that $m_1^2 < m_2^2$. Finally, the following identities for the Higgs mass mixing angle α can be derived from (2.13) (see App. A),

$$\begin{aligned} \tan 2\alpha &= \frac{2\lambda_{HS} v v_S}{\lambda_H v^2 - \lambda_S v_S^2}, \\ \sin 2\alpha &= \frac{-2\lambda_{HS} v v_S}{m_2^2 - m_1^2}, \\ \cos 2\alpha &= \frac{\lambda_S v_S^2 - \lambda_H v^2}{m_2^2 - m_1^2}. \end{aligned} \quad (2.15)$$

The Higgs sector potential (2.1) of the DCxSM has six independent real parameters: The mass parameters μ_H^2 , μ_S^2 and m_χ^2 as well as the quartic couplings λ_H , λ_S and λ_{HS} . By the minimization conditions (2.4), the parameters μ_H^2 and μ_S^2 can be replaced by a combination of v , v_S , T_H and T_S . Furthermore, due to the Eqs. (2.14) and (2.15), it is possible to exchange λ_H , λ_S and λ_{HS} in favor of m_1^2 , m_2^2 and α as follows,

$$\begin{aligned} \lambda_{HS} &= -\frac{m_2^2 - m_1^2}{2v v_S} \sin 2\alpha, \\ \lambda_H &= \frac{m_2^2 \sin^2 \alpha + m_1^2 \cos^2 \alpha}{v^2}, \\ \lambda_S &= \frac{m_2^2 \cos^2 \alpha + m_1^2 \sin^2 \alpha}{v_S^2}. \end{aligned} \quad (2.16)$$

This leads to the following set of eight independent parameters in the Higgs sector,

$$v, v_S, \alpha, m_1^2, m_2^2, m_\chi^2, T_H, T_S. \quad (2.17)$$

The tadpoles T_H and T_S are fixed during renormalization in Sec. 4.3. Moreover, $v \approx 246$ GeV [11] is the VEV of the SM-like Higgs boson and one of the masses m_1 or m_2 is identified as its mass of 125 GeV [19]. Therefore, only the following four parameters of the DCxSM are truly free in the sense that their values are yet unknown and would have to be fixed by future experiments,

$$v_S, \alpha, m_1^2 \text{ or } m_2^2, m_\chi^2. \quad (2.18)$$

The Higgs sector potential (2.1) is symmetric under the transformation $S \rightarrow S^*$. Consequently, the potential in the form of Eqs. (2.6)–(2.10) (that is, after electroweak symmetry breaking) is symmetric under the transformation $\chi \rightarrow -\chi$. This \mathbb{Z}_2 symmetry ensures that the particle represented by the field χ cannot decay into other particles: it is stable. Moreover, χ has a non-zero mass m_χ . Hence, χ represents a stable DM candidate [17].

Since χ is a pseudo Goldstone boson, this type of a DM particle is also called *pseudo Goldstone Dark Matter* [17]. In the DCxSM, the DM candidate χ interacts with particles of the Higgs sector only, which is why the DCxSM is a *Higgs-portal model* [20]. Being introduced as a particle of the weak sector, the DCxSM DM candidate χ also falls into the category of WIMPs.

CHAPTER 3

Dark Matter Direct Detection

It is assumed that galaxies are generally enveloped by a DM halo, in which all visible structures of the galaxy are embedded [21, 22]. While traveling around the sun and together with the sun around the center of the milky way, the earth moves through this DM halo. Since DM is only weakly interacting, most of the DM goes through the earth without any effect. In order to investigate the properties of the DM particles, the rare interactions between them and ordinary matter have to be observed.

There are three distinctive types of DM–SM interactions that require different experimental setups to detect the effect of a DM particle: Production at colliders, Indirect Detection and Direct Detection. These three different processes are visualized in Fig. 3.1.

The *Production* channel can be exploited using particle colliders: The scattering of two SM particles might produce DM particles; although they cannot be directly detected by the particle detectors of the collider, one can infer their existence and properties from the missing energy–momentum that they carry away. Such searches are carried out for example at the LHC at CERN. So far, the observations are consistent with the SM expectations and no production of DM particles has been observed. Future runs of the LHC will further increase the sensitivity for the detection of DM production [24].

DM searches making use of the *Indirect Detection* channel look for SM particles that have been produced by the annihilation or decay of DM particles. Such events happen most probably in dense regions of the universe – like the center of the Milky Way or our sun – and might for example produce gamma rays that can be detected by telescopes like VERITAS [25]. Neutrino detectors like IceCube or Super-Kamiokande are currently looking for DM annihilation into neutrinos [26, 27].

In this thesis, the channel of *Direct Detection* is considered. Direct Detection experiments aim for detecting the rare events when a DM particle does *not* go through the earth without

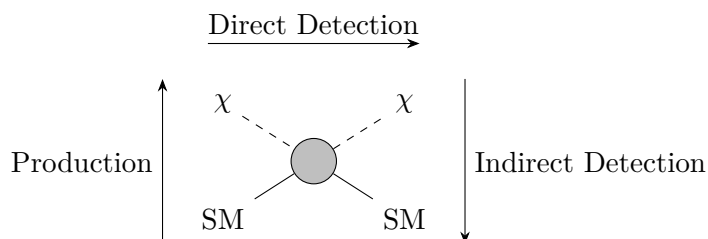


Figure 3.1: Channels for DM detection. χ is the DM particle and SM stands for any SM particle (or a nucleus or nucleon that is composed of SM particles). Diagram inspired by [23].

any effect but scatters off a nucleus from the target material of the detector. The target material can be either solid, like for example the NaI(Tl) crystals of the DAMA experiment [28], or liquid, like the xenon of the XENON100 experiment [29]. In both cases, the atoms of the target material are excited by the scattering with a DM particle and the subsequent de-excitation causes the emission of light, which is in turn measured by photomultipliers that are installed around the target material [23]. Some more details about these experiments as well as their current results are given in Sec. 3.5.

In Sec. 3.1, the kinematics of Direct Detection scattering is examined. After that, in Secs. 3.2 and 3.3, it is worked out how the measurable detection rate is linked to the scattering cross section and amplitude. In this work, the formalism of Effective Field Theory is employed to handle the results standardized way and to incorporate nuclear physics. This formalism and its application to the computation of the Direct Detection cross section in the DCxSM is introduced in Sec. 3.4. Finally, Sec. 3.6 provides a short introduction about the consideration of the relic density.

3.1 Kinematics

The detector material of typical Direct Detection experiments is kept at a low temperature. For example, the detector material of the XENON100 experiment uses 62 kg of liquid xenon as a target material that is kept at a temperature of $T = -91^\circ\text{C}$ [29]. Therefore, the target nuclei can be treated at rest initially [30].

Since the DM halo is a gravitationally bound object, the velocity of the DM particles can be assumed to be smaller than the escape velocity of the galaxy. In 2006, the RAVE survey found a likeliest value for this escape velocity of $v_{\text{esc}} = 544\text{ km/s} \approx 2 \cdot 10^{-3} c$ [31], implying that a non-relativistic treatment of the Direct Detection kinematics is justified.

Let \mathbf{p} be the initial three-momentum¹ of the DM particle, \mathbf{p}' its final momentum, $\mathbf{q}_0 = \mathbf{0}$ the vanishing initial momentum of the nucleus and $\mathbf{q}_N \equiv \mathbf{p} - \mathbf{p}'$ the momentum transfer, which equals the final momentum of the nucleus. In this chapter, the letter N will represent the nucleus and χ will be the DM particle. The generic Feynman diagram of this process is depicted in Fig. 3.2.

The initial and final energies of the system are

$$E_i = \frac{\mathbf{p}^2}{2m_\chi}, \quad E_f = \frac{(\mathbf{p} - \mathbf{q}_N)^2}{2m_\chi} + \frac{\mathbf{q}_N^2}{2m_N}, \quad (3.1)$$

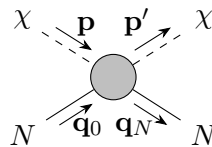


Figure 3.2: The process of Direct Detection. A DM particle χ interacts with a nucleus N , which is initially at rest, i. e. $\mathbf{q}_0 = \mathbf{0}$. By transferring the momentum \mathbf{q}_N on the nucleus, the momentum of the DM particle is changed from \mathbf{p} to \mathbf{p}' .

¹ In contrast to four-momenta, three-momenta are printed in bold type in this work.

where m_N is the mass of the nucleus and m_χ is the mass of the DM particle. Using these expressions, it immediately follows from energy conservation $E_i = E_f$ that

$$2\mu_N \mathbf{p} \cdot \mathbf{q}_N = m_\chi \mathbf{q}_N^2, \quad (3.2)$$

where μ_N is the reduced mass of the nucleus and the DM particle. If θ is the angle between \mathbf{p} and \mathbf{q}_N (note that this is not the scattering angle as it is usually defined), then $\mathbf{p} \cdot \mathbf{q}_N = |\mathbf{p}||\mathbf{q}_N| \cos \theta$ implies that

$$|\mathbf{q}_N| = 2\mu_N v \cos \theta, \quad (3.3)$$

where $v \equiv |\mathbf{p}|/m_\chi$ is the initial velocity of the DM particle. The recoil energy E_R , which equals the final kinetic energy of the nucleus in this case, can thus be given by [30]

$$E_R = \frac{|\mathbf{q}_N|^2}{2m_N} = \frac{2\mu_N^2 v^2}{m_N} \cos^2 \theta. \quad (3.4)$$

The larger this recoil energy is, the easier is its detection. The recoil energy depends on the mass of the target nucleon m_N and it is therefore an obvious goal to choose a suitable target that maximizes the recoil energy. The maximum of E_R w. r. t. m_N is easily found by solving $dE_R/dm_N = 0$ for m_N , the result being $m_N = m_\chi$ [32]. Hence, under the assumption that the DM particle is heavy (like for the well-motivated WIMPs [29]), heavy target nuclei – such as xenon, which is the heaviest non-radioactive noble gas – are required to obtain a large recoil energy.

The largest possible recoil energy in a Direct Detection experiment is therefore given by²

$$E_R^{\max} = E_R|_{m_N \rightarrow m_\chi}^{\theta \rightarrow 0} = \frac{1}{2} m_\chi v^2 < 2 \cdot 10^{-6} m_\chi, \quad (3.5)$$

where in the last step $v < v_{\text{esc}}$ was assumed. This maximum recoil energy corresponds to a maximum momentum transfer of

$$|\mathbf{q}_N|^{\max} = m_\chi v < 2 \cdot 10^{-3} m_\chi. \quad (3.6)$$

The momentum transfer is therefore small compared to the DM mass. The approximation of setting the momentum transfer to zero is perfectly valid. While the derivations in the rest of this chapter will be kept general, this approximation will be employed for the computation of the matrix elements in Chapter 5.

For a given (measured) recoil energy E_R , the minimum DM velocity v_{\min} that can lead to this recoil energy (at $\theta = 0$) is given by [30]

$$v_{\min} = \sqrt{\frac{m_N}{2\mu_N^2} E_R}, \quad (3.7)$$

² In [32] the same estimation is done with a slightly different upper bound for v and hence slightly different results.

as can be derived from Eq. (3.4).

Note that the possibility of the nucleus being raised to an excited state due to the scattering or any influence of the electrons of the target atom are usually neglected in Direct Detection computations. An introductory discussion and further references on these aspects can be found in [30].

3.2 The Detection Rate

In an (ideal) Direct Detection experiment each scattering between a DM particle and a target nucleus is detected and the recoil energy of this scattering is measured. This data corresponds to the physical quantity *differential detection rate per recoil energy* $d\mathcal{R}/dE_R$.

On the theory side, the detection rate \mathcal{R} of a scattering experiment with incoming scatter particles χ scattering and target particles N is given by [33]

$$\mathcal{R} = N_N j_\chi \sigma_N, \quad (3.8)$$

where N_N is the total number of target particles, j_χ is the particle flux (the rate of incoming DM particles per area) and σ_N is the scattering cross section. The particle flux can be given as particle number density n_χ times their velocity v , that is $j_\chi = n_\chi v$. The velocity of the DM particles is described by some velocity distribution $f(\mathbf{v})$. For Direct Detection, one is interested in the distribution $f(\mathbf{v})$ in the reference frame of the detector. Thus, also effects like the velocity modulation due to the rotation of the earth around the sun or the movement of the sun in the milky way should be taken into account upon proposing some specific form for $f(\mathbf{v})$ [30, p. 55].

Whatever the specific form of $f(\mathbf{v})$ may be, one needs to take the average over v to find the total detection rate \mathcal{R} . Since σ_N generally also depends on the velocity of the incoming particles, it needs to be included in this average [33],

$$\mathcal{R} = N_N n_\chi \langle v \sigma_N \rangle \equiv N_N n_\chi \int_{v > v_{\min}} d^3v v \sigma_N f(\mathbf{v}). \quad (3.9)$$

The integral has a lower bound because velocities smaller than v_{\min} are kinematically excluded, as it was derived in the end of Sec. 3.1. In principle, the integral does not have an upper bound, but effectively there will be some upper integration bound due to the fact that $f(\mathbf{v})$ vanishes for velocities that correspond to velocities larger than v_{esc} in the reference frame of the milky way.

In practice, one is usually more interested in the differential detection rate per recoil energy *per total target mass*. Let us therefore define the detection rate per target mass $R \equiv \mathcal{R}/M$. The quantity of interest will then be [23]

$$\frac{dR}{dE_R} = \frac{1}{M} \frac{d\mathcal{R}}{dE_R} = \frac{\rho_\chi}{m_N m_\chi} \left\langle v \frac{d\sigma_N}{dE_R} \right\rangle, \quad (3.10)$$

where $m_N = M/N_N$ is the mass of a single target nucleus and $\rho_\chi = n_\chi m_\chi$ is the (local) DM mass density. The value for ρ_χ needs to be taken from cosmological measurements (for details see Sec. 3.6). The present work only deals with the particle physics content of this detection rate, namely the cross section σ_N .

3.3 The Cross Section

The differential cross section for $2 \rightarrow 2$ scattering with the associated four-momenta $p, q_0 \rightarrow p', q_N$ of the external particles is given by [34, 35]

$$d\sigma_N = \frac{|\mathcal{M}_N|^2}{4E_\chi E_N |v - v_N|} \frac{d^3 p'}{(2\pi)^3 2E'_\chi} \frac{d^3 q_N}{(2\pi)^3 2E'_N} \cdot (2\pi)^4 \delta^{(4)}(p + q_0 - p' - q_N), \quad (3.11)$$

where \mathcal{M}_N is the corresponding scattering amplitude. For the case of Direct Detection scattering, E_χ and E_N are the initial energies of the DM particle and the nucleon, respectively, and E'_χ and E'_N are their final energies. In the non-relativistic limit, these energies can be approximated by the corresponding masses. The momenta p, q_0, p' and q_N are the four-momenta corresponding to the three-momenta from Fig. 3.2.³ Since the nucleus is at rest, one can also set $v_N \approx 0$. Using the abbreviation $\tilde{\mathcal{M}}_N \equiv \mathcal{M}_N/(4m_\chi m_N)$ and spherical coordinates for the integration over \mathbf{q}_N , Eq. (3.11) can be brought into the following form [30]:

$$\begin{aligned} d\sigma_N &= \frac{|\tilde{\mathcal{M}}_N|^2}{2\pi v} d^3 p' (|\mathbf{q}_N|^2 d\cos\theta d|\mathbf{q}_N|) \delta^{(4)}(p + q_0 - p' - q_N) \\ &= \frac{|\tilde{\mathcal{M}}_N|^2}{4\pi v} d^3 p' (|\mathbf{q}_N| d\cos\theta d|\mathbf{q}_N|^2) \delta(E_i - E_f) \delta^{(3)}(\mathbf{p} + \mathbf{p}' - \mathbf{q}_N) \\ &= \frac{|\tilde{\mathcal{M}}_N|^2}{4\pi v} (|\mathbf{q}_N| d\cos\theta d|\mathbf{q}_N|^2) \delta(E_i - E_f) \\ &= \frac{|\tilde{\mathcal{M}}_N|^2}{4\pi v} (d\cos\theta d|\mathbf{q}_N|^2) \delta(\cos\theta - |\mathbf{q}_N|/(2\mu_N v)). \end{aligned} \quad (3.12)$$

The implicit integral over the polar angle was already evaluated in the first step. In the last step, it was used that

$$E_i - E_f = v|\mathbf{q}_N| \left(\cos\theta - \frac{|\mathbf{q}_N|}{2\mu_N v} \right) \quad (3.13)$$

as well as $\delta(ax) = a^{-1}\delta(x)$.

The total cross section is now easily obtained by integration [30],

$$\begin{aligned} \sigma_N &= \frac{|\tilde{\mathcal{M}}_N|^2}{4\pi v^2} \int_{-1}^1 d\cos\theta \int_0^\infty d|\mathbf{q}_N|^2 \delta(\cos\theta - |\mathbf{q}_N|/(2\mu_N v)) \\ &= \frac{|\tilde{\mathcal{M}}_N|^2}{4\pi v^2} \int_0^\infty d|\mathbf{q}_N|^2 \theta(2\mu_N v - |\mathbf{q}_N|) \\ &= \frac{\mu_N^2}{\pi} |\tilde{\mathcal{M}}_N|^2. \end{aligned} \quad (3.14)$$

Note that the integration range of $\cos\theta$ restricts the integration range of $d|\mathbf{q}_N|^2$ to the

³ Note that here, in contrast to Sec. 3.1, all energies are not only the kinetic energies but the total relativistic energies that include the rest energy. The four-momentum of the incoming nucleon is $q_0 = (m_N, \mathbf{0})$ in the approximation of the nucleon being at rest initially.

kinematically allowed values of $|\mathbf{q}_N|$ according to Eq. (3.3). In Sec. 3.1 it was shown that this interval is much smaller than the scale of the scattering process. Hence, it can be assumed that the amplitude $\tilde{\mathcal{M}}_N$ is approximately constant within the integration range – more specifically, the momentum transfer can be set to zero in the amplitude $\tilde{\mathcal{M}}_N$. Furthermore, this justifies that $\tilde{\mathcal{M}}_N$ was pulled out of the integral in Eq. (3.14).

For the differential detection rate (3.10), the derivative $d\sigma_N/dE_R$ is required. Using $d|\mathbf{q}_N|^2/dE_R = 2m_N$, which follows from Eq. (3.4), this derivative is easily obtained from Eq. (3.12),

$$\begin{aligned} \frac{d\sigma_N}{dE_R} &= \frac{m_N}{2\pi v^2} |\tilde{\mathcal{M}}|^2 d\cos\theta \delta(\cos\theta - |\mathbf{q}_N|/(2\mu_N v)) \\ &= \frac{m_N}{2\pi v^2} |\tilde{\mathcal{M}}|^2 \theta(2\mu_N v - |\mathbf{q}_N|) \\ &= \frac{m_N \sigma_N}{2v^2 \mu_N^2} \theta(v - v_{\min}). \end{aligned} \quad (3.15)$$

In the last step, the amplitude was replaced by the cross section using Eq. (3.14). v_{\min} has been given in Eq. (3.7). This result can now be plugged into the formula for the differential detection rate, Eq. (3.10). Note that the lower limit for the velocity as dictated by the heaviside θ function in Eq. (3.15) has already been implemented in the definition of the velocity average in Eq. (3.9).

So far, the specific interactions that lead to the interaction of the DM particle with the nucleon have been treated as a black box on the level of the nucleon. That black box was called “amplitude \mathcal{M}_N ” or alternatively “cross section σ_N ”. It is desirable, however, to rather work on the level of *nucleons* n instead of *nuclei* N because the results will then be independent of the used target material. Interestingly, the whole derivation of this section works exactly in the same way also for the scattering between DM and a nucleon instead of a nucleus. Simply replace all N by n . One can therefore conclude that Eq. (3.14) can be translated directly to the level of nucleon scattering [30],

$$\sigma_n = \frac{\mu_n^2}{\pi} |\tilde{\mathcal{M}}_n|^2, \quad (3.16)$$

where μ_n is the reduced mass of the DM particle and the nucleon. Further steps on how the amplitude \mathcal{M}_n is computed are provided in Sec. 3.4. The remainder of the current section is dedicated to the question of how σ_N is related to σ_n .

An effective Lagrangian for the scattering of two DM particles χ and a nucleon n and its antinucleon \bar{n} looks like

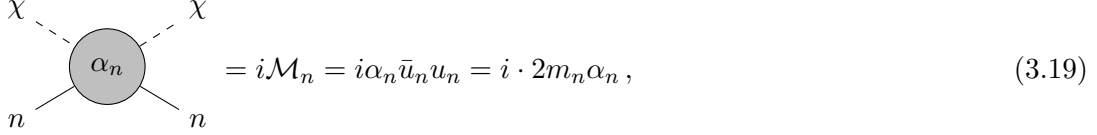
$$\mathcal{L}_{\text{eff}} = \alpha_n \chi^2 \bar{n} n, \quad (3.17)$$

where n is the nucleon spinor field and

$$\alpha_n = \frac{\partial^4 \mathcal{L}_{\text{eff}}}{\partial \chi^2 \partial \bar{n} \partial n} \quad (3.18)$$

is the effective coupling. The amplitude \mathcal{M}_n that follows from a Lagrangian (3.17) for the

scattering of the DM particle and the nucleon is



$$= i\mathcal{M}_n = i\alpha_n \bar{u}_n u_n = i \cdot 2m_n \alpha_n, \quad (3.19)$$

where it was used that the spinors of the nucleon \bar{u}_n and u_n depend on the same momentum due to the limit of vanishing momentum transfer and hence $\bar{u}_n u_n$ can simply be replaced by its normalization $2m_n$. By analogy, let the effective coupling of the *nucleus* scattering be related to the nucleus amplitude as $\mathcal{M}_N = 2m_N \alpha_N$.

For spin-independent scattering, the couplings to the nucleon α_n and to the nucleus α_N can be related by a form factor $F(q)$ as $\alpha_N = A_n \alpha_n F(q)$ and hence the amplitudes obey $\tilde{\mathcal{M}}_N = A_n \tilde{\mathcal{M}}_n F(q)$, where A_n is the number of nucleons of type n in the nucleus. If one distinguishes between protons and neutrons, a sum over $n \in \{\text{proton, neutron}\}$ is implied. Using Eq. (3.14), one arrives at [36]

$$\sigma_N = \frac{\mu_N^2}{\pi} |Z \tilde{\mathcal{M}}_{\text{proton}} + (A - Z) \tilde{\mathcal{M}}_{\text{neutron}}|^2 |F(q)|^2, \quad (3.20)$$

where $Z \equiv A_{\text{proton}}$ is the number of protons and $A - Z \equiv A_{\text{neutron}}$ the number of neutrons in the nucleus.⁴ The approximation $\tilde{\mathcal{M}}_{\text{neutron}} \approx \tilde{\mathcal{M}}_{\text{proton}}$ yields with Eq. (3.16)

$$\sigma_N = \frac{\mu_N^2}{\mu_n^2} A^2 \sigma_n |F(q)|^2 \quad (3.21)$$

for either $n = \text{proton}$ or $n = \text{neutron}$. In the limit of small momentum transfer, the approximation $F(q \approx 0) \approx 1$ is valid [36].

In terms of the effective coupling α_n , the nucleon cross section from Eq. (3.16) reads

$$\sigma_n = \frac{1}{4\pi} \left(\frac{m_n}{m_\chi + m_n} \right)^2 |\alpha_n|^2. \quad (3.22)$$

In order to give a result that is independent of detector properties (like the isotope of the target nucleus), only results for the nucleon cross section σ_n are given in this thesis. Using Eqs. (3.10), (3.15) and (3.21), it is straightforward to obtain the corresponding differential detection rate dR/dE_R for specific experimental setups and assumptions for cosmological quantities.

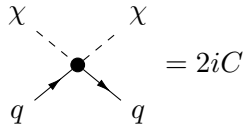
3.4 The Nucleon Cross Section in Effective Field Theory

Microscopically, when DM particles scatter off nucleons, they scatter off quarks or gluons, since those are the elementary constituents. In this section, the connection between the nucleon cross section σ_n and amplitudes of scattering processes of elementary particles, which can be computed by QFT is presented.

⁴ The spin-dependent pendant to Eq. (3.20) is given in [36].

For the purpose of a standardized handling of results and the incorporation of nuclear physics, the formalism of Effective Field Theory (EFT) will be employed in this work. The following lines give a brief introduction to how the computational results of Direct Detection are matched to in an effective Lagrangian.⁵

Effectively, the scattering of a DM particle χ and a quark q can be described by an interaction term $C\chi^2\bar{q}q$ in an effective Lagrangian, where C is some constant, called *Wilson Coefficient*. This term describes a $\chi^2\bar{q}q$ vertex that comes with the Feynman rule



$$= 2iC. \quad (3.23)$$

Then, matching the full process of the scattering $\chi + q \rightarrow \chi + q$ to the corresponding term in the effective Lagrangian requires that the amplitude is computed twice: Once simply with the effective vertex (which is trivial; the result is simply $2iC$) and once within the actual model, DCxSM in this thesis (which is not trivial, since loop corrections occur). By equating both results, C can be extracted. Thereby, the previously unknown parameter of the effective Lagrangian has been found explicitly and the EFT is set up.

The explicit computation of the diagrams and hence the computation of C is done in the subsequent chapters. In the remainder of the present chapter, C is assumed to be known and it is investigated how the nucleon cross section σ_n is constructed from C .

In practice, a few complications arise in the picture of the EFT that has been drawn in the paragraph above. To begin with, not only the coupling of the DM to quarks is relevant, but also the one to gluons. Thus, a term like $C\chi^2\bar{q}q$ will not be the only one that appears in the effective Lagrangian, but there will also be a term proportional to $\chi^2 G_{\mu\nu}^a G^{a\mu\nu}$, where $G_{\mu\nu}^a$ is the field-strength tensor of the gluon. And secondly, the amplitude that is computed from the actual DCxSM might (and will) depend on external momenta. These momentum dependent terms of the amplitude are described by derivatives of fields in the Lagrangian. Hence, yet more terms have to be added to the effective Lagrangian.

For this work, the following effective Lagrangian is sufficient to describe all the possible diagrams that will be encountered in the DCxSM Direct Detection spin-independent scattering process [17],⁶

$$\mathcal{L}_{\text{eff}} = \sum_q C_S^q \mathcal{O}_S^q + C_S^g \mathcal{O}_S^g + \sum_q C_T^q \mathcal{O}_T^q, \quad (3.24)$$

where

$$\mathcal{O}_S^q = m_q \chi^2 \bar{q}q, \quad (3.25)$$

$$\mathcal{O}_S^g = \frac{\alpha_s}{\pi} \chi^2 G_{\mu\nu}^a G^{a\mu\nu}, \quad (3.26)$$

⁵ For a detailed introduction see [36] and the references therein.

⁶ In general also a twist term for the gluons exists (see [17]), but for the computation in this work it does not contribute.

$$\mathcal{O}_T^q = \frac{1}{m_\chi^2} \chi i\partial^\mu i\partial^\nu \chi \underbrace{\frac{1}{2} i\bar{q} \left(\partial_\mu \gamma_\nu + \partial_\nu \gamma_\mu - \frac{1}{2} g_{\mu\nu} \not{\partial} \right)}_{\equiv \mathcal{O}_{\mu\nu}^q} q. \quad (3.27)$$

Here, γ_μ is the Dirac gamma matrix and $g_{\mu\nu}$ the metric tensor. The index S denotes scalar contributions and the index T stands for twist contributions. $\mathcal{O}_{\mu\nu}^q$ is the twist-2 operator [35, 37].

By differentiating the individual terms of \mathcal{L}_{eff} twice w. r. t. χ and dropping the fields of the nucleon particles (i. e. quarks and gluons), the Wilson coefficients $C_S^{q,g}$ can be related to the “ χ part” of the corresponding effective couplings $\alpha_S^{q,g}$,

$$C_S^q \mathcal{O}_S^q = C_S^q m_q \chi^2 \bar{q} q \quad \Longrightarrow \quad \alpha_S^q = 2C_S^q m_q, \quad (3.28)$$

$$C_S^g \mathcal{O}_S^g = C_S^g \frac{\alpha_s}{\pi} \chi^2 G_{\mu\nu}^a G^{a\mu\nu} \quad \Longrightarrow \quad \alpha_S^g = C_S^g \frac{2\alpha_s}{\pi}. \quad (3.29)$$

If the current state of the nucleon is denoted as a ket $|n\rangle$, then $\langle n|\bar{q}q|n\rangle$ can be interpreted as the probability to find a quark q in a nucleon n [36]. The effective coupling to the nucleon, α_n , receives contributions from the coupling to the quark α_S^q and from the coupling to the gluon α_S^g . These contributions are given by

$$\alpha_n \supset \langle n|\bar{q}q|n\rangle \alpha_S^q = 2m_n f_q^n C_S^q, \quad (3.30)$$

$$\alpha_n \supset \langle n|G_{\mu\nu}^a G^{a\mu\nu}|n\rangle \alpha_S^g = -\frac{16m_n}{9} f_g^n C_S^g, \quad (3.31)$$

where [37]

$$m_n f_q^n \equiv \langle n|m_q \bar{q}q|n\rangle, \quad (3.32)$$

$$\frac{2m_n}{27} f_g^n \equiv \left\langle n \left| -\frac{\alpha_s}{12\pi} G_{\mu\nu}^a G^{a\mu\nu} \right| n \right\rangle. \quad (3.33)$$

f_q^n and f_g^n are form factors that are obtained from lattice QCD simulations [38]. In this work, their values were taken from [37] and are given in Sec. 6.1.

Finally, consider the twist term of the effective Lagrangian (3.24). The contributions to α_n in Eqs. (3.30) and (3.31) were written as the coupling prefactor of the effective Lagrangian times the matrix element of the quark and gluon part, respectively. For the twist contribution, this implies [37]

$$\begin{aligned} \alpha_n &\supset C_T^q \frac{2}{m_\chi^2} p^\mu p^\nu \langle n|\mathcal{O}_{\mu\nu}^q|n\rangle \\ &= C_T^q \frac{2}{m_\chi^2} p^\mu p^\nu \left(\frac{1}{m_n} \left(P_\mu P_\nu - \frac{1}{4} m_n^2 g_{\mu\nu} \right) (q^n(2) + \bar{q}^n(2)) \right) \\ &\approx \frac{3}{2} m_n (q^n(2) + \bar{q}^n(2)) C_T^q, \end{aligned} \quad (3.34)$$

where p is the four-momentum of the DM particle, P is the four-momentum of the nucleon and hence $p \cdot P \approx m_n m_\chi$ in the non-relativistic approximation. $q^n(2)$ and $\bar{q}^n(2)$ are the

second moments of a quark q or an antiquark \bar{q} , respectively. Just like f_q^n and $f_{\bar{q}}^n$ they are numerical factors, whose values were taken from [37] in this work.

After adding up all these contributions to α_n and plugging them into Eq. (3.22), the final result is [17]

$$\sigma_n = \frac{1}{\pi} \left(\frac{m_n}{m_\chi + m_n} \right)^2 \left| \sum_{q=u,d,s} m_n f_q^n C_S^q - \frac{8}{9} m_n f_g^n C_S^g + \frac{3}{4} m_n \sum_{q=u,d,s,c,b} (q^n(2) + \bar{q}^n(2)) C_T^q \right|^2. \quad (3.35)$$

The major contribution to this cross section comes from the light quarks $q = u, d, s$. The leading-order interaction between two gluons and two DM particles is mediated by a Higgs boson and a quark loop (see Fig. 5.8). Since the masses of the heavy quarks $Q = c, t, b$ are larger than the relevant mass scale of Direct Detection, they need to be integrated out (see Sec. 5.3.1). In the contribution from the twist-2 operator, that is in the last term of the absolute square in Eq. (3.35), all quarks below an energy scale of ~ 1 GeV have to be included, i. e. all quarks but the top quark [39].

3.5 Current Limits of Direct Detection Experiments

Until today, none of the experiments aiming for the detection of DM has produced evidence for the existence of a DM particle [48]. However, not finding a detection signal in a given experimental constellation excludes certain regions of parameter spaces.

The first experiment that produced an exclusion limit in the DM mass–cross section space was carried out in 1986 [13, 49]. Since then, many more experiments with increasing sensitivity have been designed. Currently the experiments with the highest sensitivity are based on liquid xenon detectors. Especially the LUX experiment in South Dakota, USA [41], the PANDAX experiment in Sichuan, China [40], and the XENON experiments in Abruzzo, Italy [29], have further and further increased the sensitivity of Direct Detection.

The most obvious way to increase the sensitivity of a Direct Detection experiment is to increase the target mass. Thus, the XENON collaboration started off with XENON10 and a target mass of 15 kg in 2006–2007 [42], went on with XENON100 and a target mass of 62 kg in 2010–2014 [43] and arrived at XENON1T with a target mass of 2 t in 2016–2017. With the XENON1T experiment, the detection limit for the cross section has come down to $5 \times 10^{-47} \text{ cm}^2$ for a DM mass of 50 GeV [44]. Since no signal has been detected, the parameter space leading to higher cross sections can be excluded. The solid lines in Fig. 3.3 show the exclusion limits of several xenon based Direct Detection experiments. They can be deduced from the measured differential detection rate using Eq. (3.10) [23].

Currently, the next-generation XENON10T experiment is constructed in Italy. It is expected to lower the limit of the cross section by another order of magnitude [45]. Its prospective limit is plotted as a dashed line in Fig. 3.3.

At even smaller cross sections (for example 10^{-49} cm^2 at 50 GeV), a given signal could also stem from the scattering between a neutrino and a target nucleus. Therefore, it would be practically impossible to detect a DM particle using the Direct Detection channel if its cross section lies within the gray neutrino background region (also called the *neutrino floor*) in Fig. 3.3 [46].

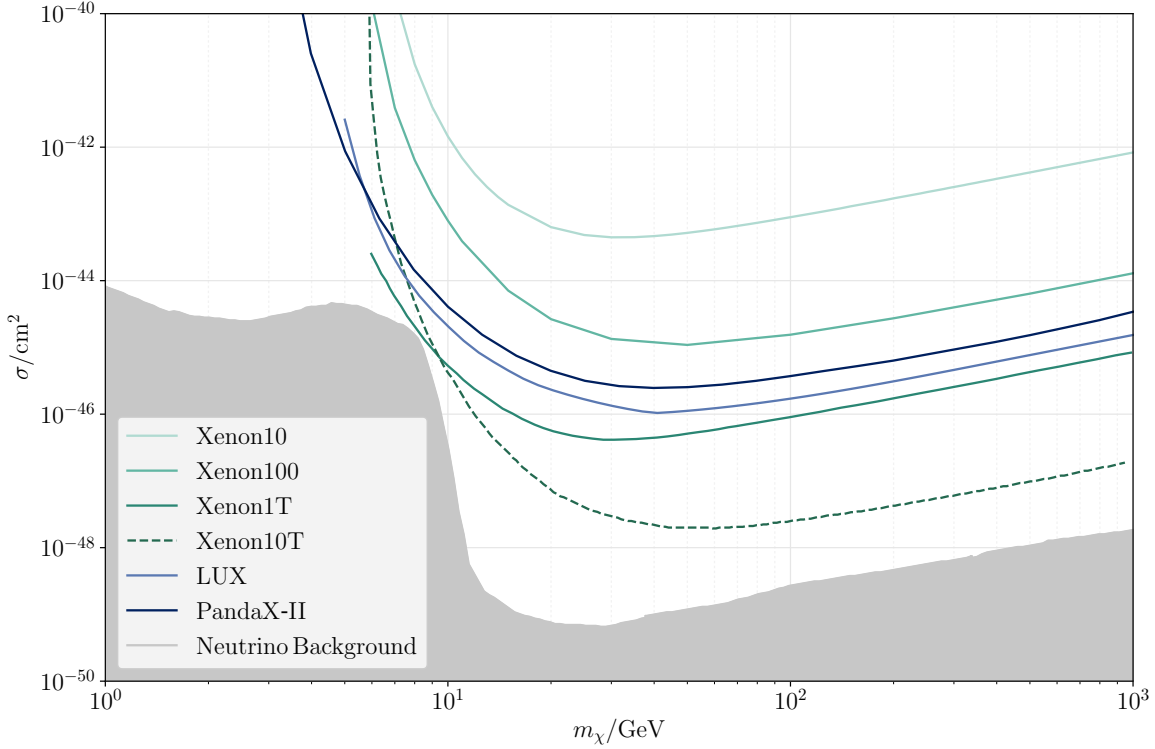


Figure 3.3: Limits of liquid xenon based Direct Detection Experiments. The parameter space above the solid and dashed lines is excluded by the corresponding experiments. The dashed line shows the prospective limit of the XENON10T experiment. The gray region on the bottom of the diagram is the neutrino floor, below which a signal could not be assigned to the influence of DM any more due to the background from neutrino–xenon scattering. Data taken from [40–46], using the tool [47].

3.6 The Relic Abundance

The *relic abundance* of DM $(\Omega h^2)_{\text{DM}}$ is a measure for the density of DM in the universe. It is defined as the absolute DM density ρ_{DM} divided by the critical density ρ_c times the squared dimensionless Hubble parameter h ,

$$(\Omega h^2)_{\text{DM}} \equiv \frac{\rho_{\text{DM}}}{\rho_c} h^2. \quad (3.36)$$

This relic density of the total amount of DM is measured by the Planck Collaboration, yielding a value of [50]

$$(\Omega h^2)_{\text{DM}} = 0.1186 \pm 0.002. \quad (3.37)$$

The relic abundance $(\Omega h^2)_\chi$ for a specific DM candidate can be determined in the standard freeze-out framework, for which the program library MICROMEGAS [51] is used to calculate the predicted relic abundance for a specific model set-up. If the predicted relic density $(\Omega h^2)_\chi$ is smaller than the observed relic density $(\Omega h^2)_{\text{DM}}$, the candidate χ may make up for only a

portion of the total DM in the universe. Thus, the local mass density ρ_χ of the DM candidate χ is given by

$$\rho_\chi = \rho_{\text{DM}} \frac{\rho_\chi}{\rho_{\text{DM}}} \approx \rho_{\text{DM}} \frac{(\Omega h^2)_\chi}{(\Omega h^2)_{\text{DM}}}, \quad (3.38)$$

where ρ_{DM} is the local mass density of all DM. A value of $\rho_{\text{DM}} \approx 0.4 \text{ GeV}/\text{cm}^3$ complies with many recent measurements [52].

Since experimental limits on DM–nucleon scattering (such as those in Fig. 3.3) are derived assuming that the DM candidate is responsible for all the DM abundance in the universe, it is the *effective cross section* [39]

$$\sigma_n^{\text{eff}} \equiv f_{\chi\chi} \sigma_n, \quad \text{where} \quad f_{\chi\chi} \equiv \frac{(\Omega h^2)_\chi}{(\Omega h^2)_{\text{DM}}}, \quad (3.39)$$

that can directly be compared with these limits.

CHAPTER 4

Renormalization of the DCxSM

In this work, higher-order electroweak corrections to the Direct Detection process in the DCxSM are computed. When turned into analytical expressions, the Feynman diagrams of higher-order corrections contain integrals that typically diverge. However, it can be shown that if all diagrams that describe a given physical process up to a given order in perturbation theory are taken into account, these divergences always cancel in measurable observables [34]. In order to handle these divergences and to systematically organize their cancellations, it is crucial to apply the machinery of renormalization.

This chapter presents how renormalization is applied to the next-to-leading-order (NLO) corrections of the Direct Detection process in the DCxSM. In Sec. 4.1, the basic procedure of renormalization is introduced for a simple toy model, the ϕ^4 theory. The subsequent sections introduce the various generalizations and adjustments of this basic procedure that are required to renormalize the DCxSM Direct Detection process.

The tree-level diagram of Direct Detection in the DCxSM is shown in Fig. 4.1a. The higher-order corrections to this process that require renormalization can be classified into three categories: Corrections to the Higgs propagator, corrections to the DM–Higgs vertices $\chi\chi h_i$ ($i = 1, 2$) as well as corrections to the quark–Higgs vertices $\bar{q}qh_i$, as shown in Fig. 4.1b.

There are diagrams that contribute to the DCxSM Direct Detection but fall into neither of these three categories: Box diagrams, which are finite and do not require renormalization, and diagrams with external gluons, which can be related to corresponding diagrams with external quarks and therefore do not require additional renormalization procedures. An overview over *all* diagrams that contribute to DCxSM Direct Detection as well as the treatment of Box diagrams and diagrams with external gluons is given in Chapter 5.

As it will be worked out in Sec. 4.1, during renormalization, all parameters of the theory are split up into renormalized parameters and counterterms. The counterterms give rise to a counterterm diagram for each of the corrections in Fig. 4.1b. They are presented in Fig. 4.2. The goal of the current chapter is to compute these counterterm diagrams.

The renormalization of the Higgs propagator is presented in Sec. 4.2. In order to compute

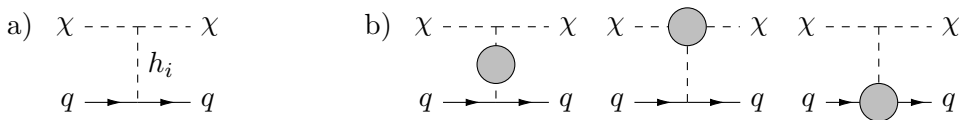


Figure 4.1: The tree-level diagram of Direct Detection in the DCxSM (a) as well as the three types of higher-order corrections that require renormalization (b): Propagator corrections and corrections to each of the two vertices of the tree-level diagram. The mediator is in any case a Higgs boson, either h_1 or h_2 .

The full propagator of a scalar field, including all possible forms of its self-interactions, is then given by [34]

$$G(p^2) \equiv \text{---} + \text{---} \circlearrowleft \text{1PI} \text{---} + \text{---} \circlearrowleft \text{1PI} \text{---} \circlearrowleft \text{1PI} \text{---} + \dots$$

$$= \frac{i}{p^2 - m_0^2 + \Sigma(p^2)} . \quad (4.7)$$

It is known from the *Källén–Lehmann spectral decomposition* [34] that $-iG(p^2)$ has a pole with residue Z at the physical mass m^2 ,

$$-iG(p^2) \rightarrow \frac{Z}{p^2 - m^2} \quad \text{for} \quad p^2 \rightarrow m^2 . \quad (4.8)$$

Z is the *field-strength renormalization constant* and m is the measurable particle mass [34].

In the vicinity of this pole, the denominator of $G(p^2)$ of Eq. (4.7) has the form

$$iG^{-1}(p^2) = m^2 - m_0^2 + \Sigma(m^2) + \left(1 + \left. \frac{\partial \Sigma(p^2)}{\partial p^2} \right|_{p^2=m^2} \right) (p^2 - m^2) + \mathcal{O}((p^2 - m^2)^2) . \quad (4.9)$$

Comparing this expression with Eq. (4.8) reveals that [34]

$$m^2 - m_0^2 + \Sigma(m^2) = 0, \quad Z^{-1} = 1 + \left. \frac{\partial \Sigma(p^2)}{\partial p^2} \right|_{p^2=m^2} . \quad (4.10)$$

Hence, taking higher-order corrections into account, the physical mass m obviously differs from the mass parameter m_0 in the Lagrangian, which is referred to as the *bare mass* [34]. By a similar procedure, a physical coupling constant λ is introduced that differs from the bare coupling constant λ_0 (see [35]).

After computing the amplitude for a given process of the Lagrangian of ϕ^4 theory (4.1) in terms of the bare parameters m_0 and λ_0 , these bare parameters can be replaced by their physical counterparts m and λ by Eq. (4.10) and an analog equation for λ_0 and the resulting expression of the amplitude will be finite [34]. While this procedure always works, there is a more systematic approach for consistently canceling all infinities. It is based on constructing the *renormalized Lagrangian* from the *bare Lagrangian* in Eq. (4.1).

For that purpose, the renormalized field ϕ is introduced as

$$\phi \equiv Z^{-1/2} \phi_0 \quad (4.11)$$

and all free bare parameters as well as the field-strength renormalization constant are split into renormalized parameters and counterterms,

$$m_0^2 = m_R^2 + \delta m^2, \quad \lambda_0 = \lambda_R + \delta \lambda, \quad Z = 1 + \delta Z . \quad (4.12)$$

While the renormalized parameters m_R^2 and λ_R are finite, the counterterms δm^2 , $\delta \lambda$ and δZ and hence also the bare parameters are infinite. In general, the value of m_R can differ from

the physical mass m and depends on the *renormalization scheme* that is used. Equivalently, by Eq. (4.12), the choice of a certain renormalization scheme also fixes the finite parts of the counterterms.

The renormalized Lagrangian is constructed from the bare Lagrangian (4.1) by renormalizing the field according to Eq. (4.11) and expressing the bare parameters by their renormalized counterparts and the counterterms using Eq. (4.12),

$$\mathcal{L} = \frac{1}{2}Z(\partial^\mu\phi)^2 - \frac{m_0^2}{2}Z\phi^2 - \frac{\lambda_0}{4!}Z^2\phi^4 \quad (4.13)$$

$$\begin{aligned} &= \frac{1}{2}(\partial^\mu\phi)^2 - \frac{m_R^2}{2}\phi^2 - \frac{\lambda_R}{4!}\phi^4 \\ &\quad + \frac{1}{2}\delta Z(\partial^\mu\phi)^2 - \frac{1}{2}(m_R^2\delta Z + \delta m^2)\phi^2 - \frac{1}{4!}(2\lambda_R\delta Z + \delta\lambda)\phi^4. \end{aligned} \quad (4.14)$$

Since the counterterms are of order $\lambda_0 = \lambda_R + \mathcal{O}(\lambda^2)$ or higher, all terms in the second line of Eq. (4.14) can be treated perturbatively, assuming that the coupling constant λ_R is small. Diagrammatically, they are given as a counterterm propagator and a counterterm vertex, respectively, which give rise to the Feynman rules

$$\text{---}\otimes\text{---} = i(p^2\delta Z - m_R^2\delta Z - \delta m^2), \quad (4.15)$$

$$\begin{array}{c} | \\ \text{---}\otimes\text{---} \\ | \end{array} = -i(2\lambda_R\delta Z + \delta\lambda). \quad (4.16)$$

The 1PI function $\hat{\Sigma}(p^2)$ of the scalar propagator in the renormalized theory not only contains loop diagrams but also counterterms and is given by

$$\begin{aligned} i\hat{\Sigma}(p^2) &= \text{---}\text{---} + \text{---}\otimes\text{---} + \mathcal{O}(\lambda^2) \\ &= i\Sigma(p^2) + i\delta Z(p^2 - m_R^2) - i\delta m^2 + \mathcal{O}(\lambda^2). \end{aligned} \quad (4.17)$$

By the analog derivation, the full propagator of the renormalized theory has the same form as the full propagator of the bare theory in Eq. (4.7), but with m_0 replaced by m_R and $\Sigma(p^2)$ replaced by $\hat{\Sigma}(p^2)$,

$$\hat{G}(p^2) = \frac{i}{p^2 - m_R^2 + \hat{\Sigma}(p^2)}. \quad (4.18)$$

Plugging in Eq. (4.17) one finds for the denominator of $\hat{G}(p^2)$

$$\begin{aligned} -i\hat{G}^{-1}(p^2) &= Z(p^2 - m_R^2) + \Sigma(p^2) - \delta m + \mathcal{O}(\lambda^2) \\ &= Z(p^2 - m_0^2 + \Sigma(p^2)) + \mathcal{O}(\lambda^2) \\ &= -iZG^{-1}(p^2) + \mathcal{O}(\lambda^2), \end{aligned} \quad (4.19)$$

where Eq. (4.12) was used. Hence, the factor Z in the Källén–Lehmann spectral decomposi-

tion (4.8) drops out in the equivalent condition for the renormalized full propagator $\hat{G}(p^2)$ [34], for which holds

$$-i\hat{G}(p^2) \rightarrow \frac{1}{p^2 - m^2} \quad \text{for} \quad p^2 \rightarrow m^2. \quad (4.20)$$

For the propagator $\hat{G}(p^2)$ in Eq. (4.18) to comply with Eq. (4.20), the *renormalization conditions*

$$\text{Re } \hat{\Sigma}(m^2) = m_R^2 - m^2, \quad \text{Re } \left. \frac{\partial \hat{\Sigma}(p^2)}{\partial p^2} \right|_{p^2=m^2} = 0. \quad (4.21)$$

need to be employed [35]. The real parts in these equations are required for the case where the energy threshold for the loop particles going on-shell has been exceeded, since $\Sigma(p^2)$ and hence also $\hat{\Sigma}(p^2)$ will then acquire an imaginary part [34].

As stated before, the renormalization scheme determines the finite parts of the counterterms. For example, in the *minimal subtraction (MS) renormalization scheme* the counterterms are chosen in such a way that they contain exactly the infinite terms that cancel the infinities of $\Sigma(p^2)$ in Eq. (4.17) but do not contain any finite parts. In this case, the first renormalization condition in Eq. (4.21) is required to relate the renormalized mass m_R to the physical mass m [35]. In the *on-shell renormalization scheme*, the renormalized mass m_R is identified with the physical mass m , i. e. $m_R = m$, such that the renormalization conditions (4.21) fix the counterterms using Eq. (4.17) as follows [35],

$$\delta m^2 = \text{Re } \Sigma(m^2) + \mathcal{O}(\lambda^2), \quad \delta Z = -\text{Re } \left. \frac{\partial \Sigma(p^2)}{\partial p^2} \right|_{p^2=m^2} + \mathcal{O}(\lambda^2), \quad (4.22)$$

assuming the counterterms have no imaginary part. Also in the on-shell renormalization scheme, the infinite parts of the counterterms cancel the infinities of the loop diagram in Eq. (4.17) and thereby rendering $\hat{\Sigma}(p^2)$ finite. All subsequent derivations in this work will be performed in the on-shell renormalization scheme.

For Direct Detection in the DCxSM, the following parameters need to be renormalized,

| | | |
|---------------------|--|-------------------|
| Higgs masses: | $m_{i0}^2 = m_i^2 + \delta m_i^2,$ | see Sec. 4.2–4.3, |
| Tadpoles: | $T_{H0} = T_H + \delta T_H,$ | see Sec. 4.3, |
| | $T_{S0} = T_S + \delta T_S,$ | see Sec. 4.3, |
| Higgs mixing angle: | $\alpha_0 = \alpha + \delta\alpha,$ | see Sec. 4.4, |
| DM mass: | $m_{\chi 0}^2 = m_\chi^2 + \delta m_\chi^2,$ | see Sec. 4.5, |
| Quark mass: | $m_{q0} = m_q + \delta m_q,$ | see Sec. 4.7, |
| W boson mass: | $m_{W0}^2 = m_W^2 + \delta m_W^2,$ | see Sec. 4.8, |
| Z boson mass: | $m_{Z0}^2 = m_Z^2 + \delta m_Z^2,$ | see Sec. 4.8, |
| Weak coupling: | $g_0 = g + \delta g,$ | see Sec. 4.8, |
| Elementary charge: | $e_0 = e - \delta Z_e e/2,$ | see Sec. 4.8. |

Moreover, the following fields have to be renormalized,

$$\begin{aligned}
\text{Higgs boson:} \quad h_{i0} &= \left(\delta_{ij} + \frac{1}{2} \delta Z_{ij} \right) h_j, & \text{see Sec. 4.2, 4.3,} \\
\text{DM particle:} \quad \chi_0 &= \left(1 + \frac{1}{2} \delta Z_\chi \right) \chi, & \text{see Sec. 4.5,} \\
\text{Quarks:} \quad q^{R,L} &= \left(1 + \frac{1}{2} \delta Z^{R,L} \right) q^{R,L}, & \text{see Sec. 4.7,} \\
\text{Gauge bosons:} \quad V_a^\mu &= \left(1 + \frac{1}{2} \delta Z_{ab} \right) V_b^\mu, & \text{see Sec. 4.8.}
\end{aligned}$$

Here, $i, j = 1, 2$ is the index of the Higgs bosons, R and L mark right- and left-handed fermion fields and a, b indicate the mass eigenstates of the gauge fields.

4.2 Higgs Self-Energy

It is known from Chapter 2 that the DCxSM contains two types of Higgs particles, whose mass-eigenstates are described by the bare fields h_{10} and h_{20} . They arise from a mixing of the gauge eigenstates that are described by the bare fields ϕ_{H0} and ϕ_{S0} as described in Eq. (2.13).¹ The renormalization of those fields is more subtle than the renormalization procedure for a single scalar field that was presented in Sec. 4.1. This is due to the fact that an h_{10} particle can be turned into an h_{20} particle only by “self-interaction” (and vice versa). In other words, the diagrams

$$i\Sigma_{12}(p^2) \equiv h_{10} \text{---} \text{1PI} \text{---} h_{20} \quad \text{and} \quad i\Sigma_{21}(p^2) \equiv h_{20} \text{---} \text{1PI} \text{---} h_{10} \quad (4.23)$$

exist and are non-vanishing. Consequently, the field-strength renormalization constant Z as well as its counterterm δZ are promoted to 2×2 matrices that link the bare fields h_{10} and h_{20} with the renormalized fields h_1 and h_2 as follows,

$$\begin{pmatrix} h_{10} \\ h_{20} \end{pmatrix} = \sqrt{Z} \begin{pmatrix} h_1 \\ h_2 \end{pmatrix} \approx \left(1 + \frac{1}{2} \delta Z \right) \begin{pmatrix} h_1 \\ h_2 \end{pmatrix}. \quad (4.24)$$

In analogy to Eq. (4.19), the inverse of the renormalized propagator $\hat{G}(p^2)$ is given by²

$$\begin{aligned}
i\hat{G}^{-1}(p^2) &= \sqrt{Z}^\dagger (p^2 - M_0^2 + \Sigma(p^2)) \sqrt{Z} \\
&= p^2 - M^2 + \hat{\Sigma}(p^2).
\end{aligned} \quad (4.25)$$

Here, M^2 is the diagonal mass matrix that has been introduced in Eq. (2.13) and M_0^2 is the

¹ All fields and parameters in Chapter 2 are bare. Since distinguishing between bare and renormalized fields and parameters is critical solely in the current chapter, only now bare quantities are labeled explicitly by an index 0.

² For the moment, let us neglect the matrix \mathcal{T} from Eq. (2.11), such that M_0^2 and M^2 rather than M_{T0}^2 and M_T^2 are actually the diagonal mass matrices for the fields h_1 and h_2 . Sec. 4.3 will be dedicated to handle the matrix \mathcal{T} .

corresponding bare mass matrix with the bare masses m_{10}^2 and m_{20}^2 as diagonal elements. Evidently, also the propagator as well as $\Sigma(p^2)$ and $\hat{\Sigma}(p^2)$ are matrices. Due to the symmetry of the diagrams in Eq. (4.23), these matrices are symmetric, i.e.

$$\Sigma_{12}(p^2) = \Sigma_{21}(p^2). \quad (4.26)$$

Expanding M_0^2 and Z in the first line of Eq. (4.25) in terms of their counterterms and comparing this expansion with its second line leads to

$$\hat{\Sigma}(p^2) \approx \Sigma(p^2) - \delta M^2 + \frac{1}{2} \delta Z^\dagger (p^2 - M^2) + \frac{1}{2} (p^2 - M^2) \delta Z. \quad (4.27)$$

Here, δM^2 is a diagonal matrix whose diagonal elements are the mass counterterms δm_1^2 and δm_2^2 , respectively, such that

$$M_0^2 = M^2 + \delta M^2. \quad (4.28)$$

In the ϕ^4 theory of Sec. 4.1, the renormalization conditions of Eq. (4.21) were chosen in such a way that the physical mass was the real part of the pole of the renormalized full propagator $\hat{G}(p^2)$ and the residue of $-i\hat{G}(p^2)$ was 1. Similarly, the diagonal elements of $-i$ times the Higgs doublet propagator $\hat{G}(p^2)$ should also have poles with residue 1 at the physical masses m_1^2 and m_2^2 , respectively, in order to comply with the Källén–Lehmann spectral decomposition. For the off-diagonal elements, a new condition is imposed that simply requires them to vanish for both $p^2 \rightarrow m_1^2$ and $p^2 \rightarrow m_2^2$. Explicitly, the renormalized propagator should obey [55]

$$-\text{Re } i\hat{G}(p^2) = \begin{cases} \begin{pmatrix} (p^2 - m_1^2)^{-1} & 0 \\ 0 & C_1 \end{pmatrix}, & \text{for } p^2 \rightarrow m_1^2, \\ \begin{pmatrix} C_2 & 0 \\ 0 & (p^2 - m_2^2)^{-1} \end{pmatrix}, & \text{for } p^2 \rightarrow m_2^2, \end{cases} \quad (4.29)$$

where C_i is some non-zero constant. For the inverse propagator, this implies

$$\text{Re } i\hat{G}^{-1}(p^2) = \begin{cases} \begin{pmatrix} p^2 - m_1^2 & 0 \\ 0 & C_1^{-1} \end{pmatrix}, & \text{for } p^2 \rightarrow m_1^2, \\ \begin{pmatrix} C_2^{-1} & 0 \\ 0 & p^2 - m_2^2 \end{pmatrix}, & \text{for } p^2 \rightarrow m_2^2. \end{cases} \quad (4.30)$$

In order to impose this behavior on the renormalized propagator, it is sufficient to employ

the following renormalization conditions:

$$\operatorname{Re} i\hat{G}_{ij}^{-1}(p^2) \Big|_{p^2 \rightarrow m_k^2} \stackrel{!}{=} \operatorname{Re} \hat{\Sigma}_{ij}(m_k^2) \stackrel{!}{=} 0, \quad \text{for } i \neq j, \quad (4.31)$$

$$\operatorname{Re} i\hat{G}_{ii}^{-1}(p^2) \Big|_{p^2 \rightarrow m_i^2} \approx \operatorname{Re} \hat{\Sigma}_{ii}(m_i^2) + \left(1 + \operatorname{Re} \frac{\partial \hat{\Sigma}_{ii}(p^2)}{\partial p^2} \Big|_{p^2=m_i^2} \right) (p^2 - m_i^2) \stackrel{!}{=} p^2 - m_i^2. \quad (4.32)$$

Here, Eq. (4.25) was used; in Eq. (4.32) a Taylor expansion at $p^2 = m_i^2$ was applied. It is straightforward to translate the renormalization conditions on the inverse propagator (4.31) and (4.32) to conditions on the renormalized 1PI function $i\hat{\Sigma}(p^2)$. Explicitly, it is required that

$$\operatorname{Re} \hat{\Sigma}_{11}(m_1^2) \stackrel{!}{=} 0, \quad \operatorname{Re} \hat{\Sigma}_{12}(m_1^2) \stackrel{!}{=} 0, \quad \operatorname{Re} \hat{\Sigma}_{21}(m_1^2) \stackrel{!}{=} 0, \quad (4.33)$$

$$\operatorname{Re} \hat{\Sigma}_{22}(m_2^2) \stackrel{!}{=} 0, \quad \operatorname{Re} \hat{\Sigma}_{12}(m_2^2) \stackrel{!}{=} 0, \quad \operatorname{Re} \hat{\Sigma}_{21}(m_2^2) \stackrel{!}{=} 0, \quad (4.34)$$

$$\operatorname{Re} \frac{\partial \hat{\Sigma}_{11}(p^2)}{\partial p^2} \Big|_{p^2=m_1^2} \stackrel{!}{=} 0, \quad \operatorname{Re} \frac{\partial \hat{\Sigma}_{22}(p^2)}{\partial p^2} \Big|_{p^2=m_2^2} \stackrel{!}{=} 0. \quad (4.35)$$

These conditions can now be employed to fix the counterterms δM^2 and δZ . For this purpose, consider the explicit form of the matrix $\hat{\Sigma}(p^2)$. Assuming Z is a real matrix³ it is found from Eq. (4.27) that

$$\begin{aligned} \hat{\Sigma}(p^2) &= \Sigma(p^2) - \delta M^2 \\ &+ \frac{1}{2} \begin{pmatrix} 2(p^2 - m_1^2)\delta Z_{11} & (p^2 - m_2^2)\delta Z_{21} + (p^2 - m_1^2)\delta Z_{12} \\ (p^2 - m_1^2)\delta Z_{12} + (p^2 - m_2^2)\delta Z_{21} & 2(p^2 - m_2^2)\delta Z_{22} \end{pmatrix}. \end{aligned} \quad (4.36)$$

Hence, the conditions (4.33)–(4.35) imply

$$\begin{aligned} \delta M_{11}^2 &= \operatorname{Re} \Sigma_{11}(m_1^2), & \delta M_{22}^2 &= \operatorname{Re} \Sigma_{22}(m_2^2), \\ \delta Z_{12} &= \frac{2}{m_2^2 - m_1^2} \operatorname{Re} (\delta M_{21}^2 - \Sigma_{21}(m_2^2)), & \delta Z_{21} &= \frac{2}{m_1^2 - m_2^2} \operatorname{Re} (\delta M_{12}^2 - \Sigma_{12}(m_1^2)), \\ \delta Z_{11} &= -\operatorname{Re} \frac{\partial \Sigma_{11}(p^2)}{\partial p^2} \Big|_{p^2=m_1^2}, & \delta Z_{22} &= -\operatorname{Re} \frac{\partial \Sigma_{22}(p^2)}{\partial p^2} \Big|_{p^2=m_2^2}. \end{aligned} \quad (4.37)$$

Here, these conditions have been given for a general matrix δM^2 – despite the fact that δM^2 is a diagonal matrix $\operatorname{diag}(\delta m_1^2, \delta m_2^2)$ – as the general formulas will be useful in Sec. 4.3.

4.3 Tadpole Renormalization

The tadpole parameters T_H and T_S have been defined as the value of the potential at the points where the fields H and S equal the parameters v and v_S , cf. Eqs. (2.3) and (2.4). Setting

³ At NLO, this assumption is sufficient [56].

$T_H = T_S = 0$ makes v and v_S the minimum of the potential and thereby the VEVs of the fields H and S , respectively.

While simply setting $T_H = T_S = 0$ works perfectly fine at tree level, the situation is more complicated when taking higher-order corrections into account. Upon renormalization, the (bare) parameters μ_{H0}^2 , μ_{S0}^2 , λ_{H0} , λ_{S0} , λ_{HS0} and $m_{\chi 0}^2$ that appear in the definition of the tadpole parameters (2.4) are split into physical parameters and corresponding counterterms, that is

$$p_0 = p + \delta p, \quad (4.38)$$

where p denotes any parameter of the Lagrangian. Consequently, also the tadpole parameters are expanded in the same way:

$$T_{H0} = T_H + \delta T_H, \quad T_{S0} = T_S + \delta T_S. \quad (4.39)$$

At NLO, simply setting all these tadpole parameters to zero comes with severe consequences. In order to understand these consequences, consider the tadpole terms V_1 in the Lagrangian, that are given in Eq. (2.7). In this work all computations are done in the mass basis defined by Eq. (2.13) and it is therefore convenient to define

$$\begin{pmatrix} T_{10} \\ T_{20} \end{pmatrix} \equiv R(\alpha_0) \begin{pmatrix} T_{H0} \\ T_{S0} \end{pmatrix}, \quad (4.40)$$

such that the tadpole terms can be translated into the mass basis as follows:

$$\mathcal{L} \supset -V_1 = -(T_{H0}, T_{S0}) \begin{pmatrix} \phi_{H0} \\ \phi_{S0} \end{pmatrix} = -(T_{10}, T_{20}) \begin{pmatrix} h_{10} \\ h_{20} \end{pmatrix} = -T_{i0} h_{i0}. \quad (4.41)$$

These tadpole terms correspond to ‘‘vertices’’ with a single external line h_{i0} that come with factors of $-iT_{i0}$. These vertices receive higher-order corrections in form of a 1PI function that we are going to call $i\Xi_i$. It is the analog to $i\Sigma(p^2)$ of the propagator in Eq. (4.6). Note that Ξ_i is momentum independent since the external momentum of a tadpole diagram has to vanish due to momentum conservation at the vertices.⁴ The *full* tadpole (in analogy to the full propagator $G(p^2)$) is then given by

$$K_i \equiv -iT_{i0} + i\Xi_i = h_{i0} \text{---}\bullet + h_{i0} \text{---}\bigcirc \text{1PI}. \quad (4.42)$$

Now, a *renormalized* full tadpole \hat{K}_i is introduced together with a *renormalized* tadpole 1PI function $i\hat{\Xi}$ in analogy to the renormalized propagator 1PI function $i\hat{\Sigma}(p^2)$ in Eq. (4.19):

$$\hat{K}_i = -iT_i + i\hat{\Xi}_i \equiv \sqrt{Z}_{ij} (-iT_{j0} + i\Xi_j) = \sqrt{Z}_{ij} K_j. \quad (4.43)$$

Plugging the expansion in counterterms $T_{i0} = T_i + \delta T_i$ and Eq. (4.24) into the right-hand

⁴ In this sense, it is not really a ‘‘function’’. For the sake of uniformity, we will still call it ‘‘1PI function’’, just like $\Sigma(p^2)$.

side of Eq. (4.43), one finds

$$\hat{\Xi}_i = \Xi_i - \delta T_i - \frac{1}{2} \delta Z_{ij} T_j + \mathcal{O}(\delta^2), \quad (4.44)$$

where $\mathcal{O}(\delta^2)$ stands for terms of order two (or higher) in the counterterms. This is the analog to Eq. (4.17).

Note that \hat{K}_i corresponds to a 1-point function [35],

$$\begin{aligned} \hat{K}_i &= \text{FT} \langle \Omega | \mathcal{T} h_i(x) | \Omega \rangle = \text{FT} \langle \Omega | h_i(x) | \Omega \rangle = \text{FT} \langle h_i \rangle \\ &= \text{FT} \begin{cases} \cos \alpha \langle \phi_H \rangle + \sin \alpha \langle \phi_S \rangle, & \text{for } i = 1, \\ -\sin \alpha \langle \phi_H \rangle + \cos \alpha \langle \phi_S \rangle, & \text{for } i = 2, \end{cases} \end{aligned} \quad (4.45)$$

where Ω is the interacting vacuum, \mathcal{T} is the time-ordering operator and ‘‘FT’’ is a short-hand notation for a Fourier transformation. Obviously, \hat{K}_i is precisely the vacuum expectation value of the field h_i . Even if $T_i = 0$, the full tadpole \hat{K}_i can still be non-zero due to the contributions from the tadpole 1PI function $i\hat{\Xi}_i$. Due to Eq. (4.45), this would imply that also $\langle \phi_H \rangle$ and $\langle \phi_S \rangle$ do not vanish and hence the vacuum expectation values of the fields H and S are no longer v and v_S , respectively, but $v + \langle \phi_H \rangle$ and $v_S + \langle \phi_S \rangle$, according to Eq. (2.5).

Thus, in order to ensure that v and v_S are the true vacuum expectation values of the fields H and S , respectively, it is required that $\langle \phi_H \rangle$ and $\langle \phi_S \rangle$ vanish and hence that

$$\hat{K}_i \stackrel{!}{=} 0. \quad (4.46)$$

Additionally, v and v_S are by definition only the true VEVs if they are the minima of the potential, which implies by Eq. (2.4) that the physical tadpole parameters T_H and T_S must vanish. Due to Eq. (4.39) the bare tadpole parameters must then equal their counterterms:⁵

$$T_H = 0, \quad T_S = 0 \quad \Longrightarrow \quad T_{H0} = \delta T_H, \quad T_{S0} = \delta T_S. \quad (4.47)$$

Note that setting the physical tadpole parameters to zero ensures that the physical parameters $m_{1,2}^2$ as defined by Eqs. (2.14) are the true tree-level masses of the Higgs bosons $h_{1,2}$.

Using Eq. (4.40) one can easily translate Eq. (4.47) into the mass basis,

$$T_1 = 0, \quad T_2 = 0, \quad \begin{pmatrix} \delta T_1 \\ \delta T_2 \end{pmatrix} = R(\alpha) \begin{pmatrix} \delta T_H \\ \delta T_S \end{pmatrix} + \mathcal{O}(\delta^2). \quad (4.48)$$

Using Eq. (4.43) and Eq. (4.44), the observations that \hat{K}_i and T_i must vanish lead to the conclusion

$$\hat{\Xi}_i \stackrel{!}{=} 0 \quad \Longrightarrow \quad \delta T_i = \Xi_i. \quad (4.49)$$

⁵ Since counterterms are of higher order in perturbation theory, these equations imply that the bare tadpole parameters T_{H0} and T_{S0} are of higher order as well, which is why it is still consistent to set them to zero at leading order.

In the renormalized Lagrangian, the tadpole terms (4.41) read

$$\mathcal{L} \supset -V_1 = -T_i h_i - \delta T_i h_i. \quad (4.50)$$

Thus, the renormalized Lagrangian includes a tadpole counterterm

$$-i\delta T_i = h_i \text{---} \otimes. \quad (4.51)$$

The full renormalized tadpole can then be visualized diagrammatically as

$$\begin{aligned} \hat{K}_i &= h_i \text{---} \bullet + h_i \text{---} \textcircled{\text{1PI}} + h_i \text{---} \otimes \\ &= -iT_i + i\Xi_i - i\delta T_i + \mathcal{O}(\delta^2) \\ &= 0. \end{aligned} \quad (4.52)$$

It vanishes because the renormalized tadpole parameter T_i is inherently zero and the counterterm δT_i cancels Ξ_i by construction.⁶

In this work, the *Standard Tadpole Scheme* is employed, within which it is not required to make a distinction between bare and physical VEVs (in other words, the VEV counterterms are set to zero). For the *Alternative Tadpole Scheme*, see [57].

The observation that the bare tadpole parameters T_{H_0} and T_{S_0} do not vanish at NLO entails that the (bare) tadpole matrix \mathcal{T}_0 in Eq. (2.11) can no longer be dropped as it was done in Sec. 4.2. Hence, instead of the “pure” mass matrix \mathcal{M}_0 we need to use the mass matrix $\mathcal{M}_{T_0}^2 = \mathcal{M}_0^2 + \mathcal{T}_0$ that includes the tadpoles. Correspondingly, a rotated mass matrix

$$M_{T_0}^2 = R(\alpha_0) \mathcal{M}_{T_0}^2 R^{-1}(\alpha_0) = M_0^2 + R(\alpha_0) \begin{pmatrix} T_{H_0}/v & 0 \\ 0 & T_{S_0}/v_S \end{pmatrix} R^{-1}(\alpha_0) \quad (4.53)$$

is introduced. The expansion in physical parameters and counterterms reads

$$M_{T_0}^2 = M^2 + \delta M_T^2 + \mathcal{O}(\delta^2), \quad (4.54)$$

where⁷

$$\delta M_T^2 = \delta M^2 + \delta T, \quad \delta T = R(\alpha) \begin{pmatrix} \delta T_H/v & 0 \\ 0 & \delta T_S/v_S \end{pmatrix} R^{-1}(\alpha). \quad (4.56)$$

Here, M^2 and δM^2 are diagonal matrices with the Higgs masses and Higgs mass counterterms as diagonal elements, respectively. Including the tadpole matrix \mathcal{T} has therefore the effect

⁶ Note that the difference in writing the tadpole 1PI function $i\Xi_i$ with an external renormalized field h_i as in Eq. (4.52) or with an external bare field h_{i0} as in Eq. (4.42) is an additional factor Z , which contributes to the terms in $\mathcal{O}(\delta^2)$ only.

⁷ Here it was used that

$$f(\alpha_0) \frac{T_{H_0}}{v} = f(\alpha + \delta\alpha) \frac{\delta T_H}{v} = (f(\alpha) + f(\alpha)\delta\alpha + \mathcal{O}(\delta\alpha^2)) \frac{\delta T_H}{v} = f(\alpha) \frac{\delta T_H}{v} + \mathcal{O}(\delta^2), \quad (4.55)$$

since $T_H = 0$.

that instead of M_0^2 and δM^2 , the matrices M_{T0}^2 and δM_T^2 have to be used in Sec. 4.2.

Performing the matrix multiplication in the definition of δT in Eq. (4.56) explicitly and converting $\delta T_H, \delta T_S$ into $\delta T_1, \delta T_2$ using Eq. (4.48), the elements of the matrix δT can be given as

$$\begin{aligned}\delta T_{11} &= \frac{v \sin^3 \alpha + v_S \cos^3 \alpha}{vv_S} \delta T_1 + \frac{v \sin \alpha - v_S \cos \alpha}{vv_S} \cos \alpha \sin \alpha \delta T_2, \\ \delta T_{12} &= \frac{v \sin \alpha - v_S \cos \alpha}{vv_S} \cos \alpha \sin \alpha \delta T_1 + \frac{v \cos \alpha + v_S \sin \alpha}{vv_S} \cos \alpha \sin \alpha \delta T_2, \\ \delta T_{21} &= \delta T_{12}, \\ \delta T_{22} &= \frac{v \cos \alpha + v_S \sin \alpha}{vv_S} \cos \alpha \sin \alpha \delta T_1 + \frac{v \cos^3 \alpha - v_S \sin^3 \alpha}{vv_S} \delta T_2.\end{aligned}\tag{4.57}$$

With these new insights at hand, the Eqs. (4.37) need to be adjusted; specifically, the counterterms δM_{ij}^2 need to be equipped with an index T , after which Eq. (4.56) can be employed to arrive at (see also [56])

$$\begin{aligned}\delta m_1^2 &= \text{Re}(\Sigma_{11}(m_1^2) - \delta T_{11}), & \delta m_2^2 &= \text{Re}(\Sigma_{22}(m_2) - \delta T_{22}), \\ \delta Z_{12} &= \frac{2}{m_2^2 - m_1^2} \text{Re}(\delta T_{21} - \Sigma_{21}(m_2^2)), & \delta Z_{21} &= \frac{2}{m_1^2 - m_2^2} \text{Re}(\delta T_{12} - \Sigma_{12}(m_1^2)).\end{aligned}\tag{4.58}$$

The formulas for the counterterms δZ_{11} and δZ_{22} from Eq. (4.37) remain valid without change.

4.4 Mixing Angle Renormalization

The gauge and mass eigenstates of the Higgs doublet are mixed by an angle α (see Eq. (2.12) and (2.13)). By Eq. (2.15) α is related directly to parameters like the Higgs masses that are shifted by higher-order corrections and therefore need to be renormalized. Consequently, also α will receive a shift during renormalization: One has to distinguish between the bare mixing angle α_0 and the physical mixing angle α , which differ by a counterterm $\delta\alpha$,

$$\alpha_0 = \alpha + \delta\alpha.\tag{4.59}$$

There are different schemes for how to fix the counterterm $\delta\alpha$. In this work, the *Kanemura scheme* (also named *KOSY scheme* in [58]) will be employed [59]. For other schemes see [60].

Let $\sqrt{Z_\phi}$ be the field-strength renormalization matrix of the gauge eigenstate Higgs doublet,

$$\begin{pmatrix} \phi_{H0} \\ \phi_{S0} \end{pmatrix} = \sqrt{Z_\phi} \begin{pmatrix} \phi_H \\ \phi_S \end{pmatrix}.\tag{4.60}$$

It follows from Eq. (4.24) as well as from the bare and renormalized versions of Eq. (2.13) that

$$\sqrt{Z} R(\alpha) \begin{pmatrix} \phi_H \\ \phi_S \end{pmatrix} = \sqrt{Z} \begin{pmatrix} h_1 \\ h_2 \end{pmatrix} = \begin{pmatrix} h_{10} \\ h_{20} \end{pmatrix} = R(\alpha_0) \begin{pmatrix} \phi_{H0} \\ \phi_{S0} \end{pmatrix} = R(\alpha_0) \sqrt{Z_\phi} \begin{pmatrix} \phi_H \\ \phi_S \end{pmatrix}.\tag{4.61}$$

Thus, the field-strength renormalization matrices of the mass and gauge eigenstate Higgs doublet can be related by

$$\sqrt{Z} = R(\alpha_0) \sqrt{Z_\phi} R^{-1}(\alpha). \quad (4.62)$$

By expanding the field-strength renormalization matrices in terms of their counterterms Eq. (4.62) can be brought into the form

$$\begin{aligned} 1 + \frac{1}{2}\delta Z &= R(\alpha_0) R^{-1}(\alpha) + \frac{1}{2}R(\alpha_0) \delta Z_\phi R^{-1}(\alpha) + \mathcal{O}(\delta^2) \\ \iff \frac{1}{2}R(\alpha_0) \delta Z_\phi R^{-1}(\alpha) &= 1 + \frac{1}{2}\delta Z - R(\delta\alpha) + \mathcal{O}(\delta^2), \end{aligned} \quad (4.63)$$

where it was used that $R(\alpha_0)R^{-1}(\alpha) = R(\delta\alpha) + \mathcal{O}(\delta\alpha^2)$.⁸ $\mathcal{O}(\delta^2)$ stands for terms that are of second order in the counterterms. Thus, using $R(\alpha) = R(\alpha_0) + \mathcal{O}(\delta\alpha)$ and the result (4.63), the rotation of $\sqrt{Z_\phi}$ can be given as

$$\begin{aligned} R(\alpha) \sqrt{Z_\phi} R^{-1}(\alpha) &= 1 + \frac{1}{2}R(\alpha) \delta Z_\phi R^{-1}(\alpha) + \mathcal{O}(\delta^2) \\ &= 1 + \frac{1}{2}R(\alpha_0) \delta Z_\phi R^{-1}(\alpha) + \mathcal{O}(\delta^2) \\ &= 2 + \frac{1}{2}\delta Z - R(\delta\alpha) + \mathcal{O}(\delta^2) \\ &= \begin{pmatrix} 2 + \delta Z_{11}/2 - 1 & \delta Z_{12}/2 - \delta\alpha \\ \delta Z_{21}/2 + \delta\alpha & 2 + \delta Z_{22}/2 - 1 \end{pmatrix} + \mathcal{O}(\delta^2). \end{aligned} \quad (4.65)$$

In the KOSY scheme it is assumed that $\sqrt{Z_\phi}$ is a real symmetric matrix [59]. Under this assumption, also the rotated version of this matrix is real and symmetric and hence the off-diagonals of the matrix in Eq. (4.65) need to be equal, which implies [60]

$$\delta\alpha = \frac{1}{4}(\delta Z_{12} - \delta Z_{21}) + \mathcal{O}(\delta^2). \quad (4.66)$$

Plugging in the expression for δZ_{ij} from Eq. (4.58), the mixing angle counterterm is given by

$$\delta\alpha = \frac{1}{2} \frac{1}{m_2^2 - m_1^2} \text{Re} (2\delta T_{12} - \Sigma_{21}(m_2^2) - \Sigma_{12}(m_1^2)) + \mathcal{O}(\delta^2). \quad (4.67)$$

Recall that δT_{ij} is given in Eq. (4.57) and the counterterms δT_i therein are computed directly from tadpole 1PI diagrams according to Eq. (4.49).

⁸ This relation follows from

$$R(\delta\alpha) R(\alpha) = \begin{pmatrix} \cos \alpha - \delta\alpha \sin \alpha & \sin \alpha + \delta\alpha \cos \alpha \\ -\sin \alpha - \delta\alpha \cos \alpha & \cos \alpha - \delta\alpha \sin \alpha \end{pmatrix} + \mathcal{O}(\delta\alpha^2) = R(\alpha + \delta\alpha) + \mathcal{O}(\delta\alpha^2). \quad (4.64)$$

4.5 Renormalization of the Dark Matter Particle

In the Lagrangian, the mass term for the DM candidate χ in Eq. (2.8) reads⁹

$$\mathcal{L} \supset -\frac{1}{2} \underbrace{\left(m_{\chi 0}^2 + \frac{T_{S0}}{v_{S0}} \right)}_{\equiv \tilde{m}_{\chi 0}^2} \chi_0^2. \quad (4.68)$$

Splitting the bare fields and parameters in physical fields and parameters and their counterterms, we have

$$\chi_0 = \left(1 + \frac{1}{2} \delta Z_\chi \right) \chi, \quad \tilde{m}_{\chi 0}^2 = m_\chi^2 + \underbrace{\delta m_\chi^2 + \frac{\delta T_S}{v_S}}_{\equiv \delta \tilde{m}_\chi^2} + \mathcal{O}(\delta^2). \quad (4.69)$$

With $\tilde{m}_\chi^2 \equiv m_\chi^2$, the renormalization of the field χ corresponds exactly to the renormalization of ϕ^4 theory in Sec. 4.1 with the mass parameters with a tilde playing the role of the mass m in ϕ^4 theory. In the on-shell renormalization scheme (cf. Sec. 4.1), the counterterms are given by

$$\delta \tilde{m}_\chi^2 = \Sigma_\chi(\tilde{m}_\chi^2) \iff \delta m_\chi^2 = \Sigma_\chi(m_\chi^2) - \frac{\delta T_S}{v_S}, \quad (4.70)$$

$$\delta Z_\chi = - \left. \frac{\partial \Sigma_\chi(p^2)}{\partial p^2} \right|_{p^2=\tilde{m}_\chi^2} \iff \delta Z_\chi = - \left. \frac{\partial \Sigma_\chi(p^2)}{\partial p^2} \right|_{p^2=m_\chi^2}, \quad (4.71)$$

where $i\Sigma_\chi(p^2)$ is the sum of 1PI diagrams of the χ propagator. Note that T_S can be converted into a linear combination of T_1 and T_2 using Eq. (4.48), which in turn are given in Eq. (4.49). Since χ is a stable particle, real parts are not required in these formulas.

4.6 χ^2 -Higgs Vertex Renormalization

The tree-level diagram of the Direct Detection process that is presented in Fig. 4.1a features the vertex of two DM particles χ and one Higgs particle h_1 or h_2 . These interactions are described by the terms $\sim \phi_H \chi^2$ and $\sim \phi_S \chi^2$ in Eq. (2.9). After they have been converted into the mass basis h_1, h_2 using Eq. (2.13) and after replacing λ_{HS} and λ_S using Eq. (2.16), they read

$$\mathcal{L} \supset \frac{1}{2} C_{10} h_{10} \chi_0^2 + \frac{1}{2} C_{20} h_{20} \chi_0^2, \quad (4.72)$$

where

$$C_{10} = - \frac{m_{10}^2 \sin \alpha_0}{v_{S0}}, \quad C_{20} = - \frac{m_{20}^2 \cos \alpha_0}{v_{S0}}. \quad (4.73)$$

⁹ Note that the Lagrangian contains the *negative* potential; so here we have a different sign than in Eq. (2.8).

Writing the bare vertex factors as a sum of the physical coupling and its counterterm,

$$C_{i0} = C_i + \delta C_i, \quad (4.74)$$

and using that $v_{S0} = v_S$ (see Sec. 4.3), the counterterms can be expressed as

$$\delta C_1 = -\frac{\sin \alpha \delta m_1^2 + m_1^2 \cos \alpha \delta \alpha}{v_S}, \quad \delta C_2 = -\frac{\cos \alpha \delta m_2^2 - m_2^2 \sin \alpha \delta \alpha}{v_S}. \quad (4.75)$$

The bare coupling terms in Eq. (4.72) can be turned into renormalized coupling terms as

$$\frac{1}{2} C_{i0} h_{i0} \chi_0^2 = \frac{1}{2} \hat{C}_i h_i \chi^2, \quad (4.76)$$

where plugging in the Eqs. (4.24), (4.69) and (4.74) leads to

$$\hat{C}_i = C_i + \delta C_i + \underbrace{C_i \delta Z_\chi + \frac{1}{2} C_j \delta Z_{ji}}_{\equiv \delta C_i^{\text{mix}}} + \mathcal{O}(\delta^2). \quad (4.77)$$

Recall that Z_{ij} is the field-strength renormalization matrix of the Higgs fields h_i .

4.7 Renormalization of Fermions

The fermionic kinetic and mass terms in the Lagrangian after symmetry breaking read¹⁰

$$\mathcal{L} \supset \bar{q}_0^R \not{\partial} q_0^R + \bar{q}_0^L \not{\partial} q_0^L - m_0 (\bar{q}_0^R q_0^L + \bar{q}_0^L q_0^R). \quad (4.78)$$

Here, q is the fermion spinor field and the indices R and L indicate the right- and left-handed component, respectively. They are defined using a projector $P_{R,L}$,

$$q^{R,L} \equiv P_{R,L} q, \quad \text{where} \quad P_{R,L} \equiv \frac{1 \pm \gamma^5}{2}. \quad (4.79)$$

The bare fields can be related to the physical fields by

$$q_0^R = \sqrt{Z^R} q^R, \quad q_0^L = \sqrt{Z^L} q^L. \quad (4.80)$$

Note that CKM mixing is neglected in this work. Therefore, each left- and right-handed fermion has its individual field-strength renormalization constant Z^R and Z^L , respectively, and there is no need for a field-strength renormalization *matrix* with off-diagonal elements.

Using the identities (4.79) and (4.80), the terms in the Lagrangian (4.78) can be brought into the following form,

$$\mathcal{L} \supset \bar{q} (Z^R \not{\partial} P_R + Z^L \not{\partial} P_L) q - \sqrt{Z^R Z^L} m_0 (\bar{q}^R q^L + \bar{q}^L q^R). \quad (4.81)$$

¹⁰ Of course, the full Lagrangian contains terms $\bar{q}_0^R \not{D} q_0^R + \bar{q}_0^L \not{D} q_0^L$ with a covariant derivative. Here, only the kinetic part of the covariant derivative $D = \partial + \dots$ is considered.

The field-strength renormalization constants then also appear in the fermion propagator that corresponds to this Lagrangian, just as it was encountered for ϕ^4 in Eq. (4.19). The full renormalized fermion propagator therefore reads

$$\hat{G}(p) = \frac{i}{Z^R \not{p} P_R + Z^L \not{p} P_L - \sqrt{Z^R Z^L} m_0 + (\Sigma(p) + \mathcal{O}(\delta^2))}, \quad (4.82)$$

where $i\Sigma(p)$ is the sum of all 1PI diagrams of the fermion propagator defined analogously to Eq. (4.6).¹¹ Because any four-momentum p within $\Sigma(p)$ can only be contracted to either another p forming p^2 or to a γ matrix forming \not{p} , it is always possible to decompose $\Sigma(p)$ into

$$\Sigma(p) = \not{p} A(p^2) + B(p^2) \quad (4.83)$$

by using $\not{p}^2 = p^2$. Splitting it also into right- and left-handed parts, $\Sigma(p)$ can generally be given as [61]:

$$\Sigma(p) = \not{p} P_R \Sigma^R(p^2) + \not{p} P_L \Sigma^L(p^2) + m P_R \Sigma^r(p^2) + m P_L \Sigma^l(p^2). \quad (4.84)$$

In CP conserving theories it turns out that $\Sigma^r(p^2) = \Sigma^l(p^2) \equiv \Sigma^S(p^2)$ [61], and hence the simpler decomposition

$$\Sigma(p) = \not{p} P_R \Sigma^R(p^2) + \not{p} P_L \Sigma^L(p^2) + m \Sigma^S(p^2) \quad (4.85)$$

is sufficient.

Plugging this decomposition as well as $m_0 = m + \delta m$ into Eq. (4.82), the denominator of the propagator reads

$$\begin{aligned} i\hat{G}^{-1}(p) &= \not{p} - m + \not{p} P_R (\Sigma^R(p^2) + \delta Z^R) + \not{p} P_L (\Sigma^L(p^2) + \delta Z^L) \\ &\quad - \frac{1}{2} m (\delta Z^R + \delta Z^L) - \delta m + m \Sigma^S(p^2) + \mathcal{O}(\delta^2). \end{aligned} \quad (4.86)$$

Introducing the renormalized 1PI function $\hat{\Sigma}(p)$ by writing the renormalized propagator as

$$\hat{G}(p) = \frac{i}{\not{p} - m + \hat{\Sigma}(p)} \quad (4.87)$$

and decomposing $\hat{\Sigma}(p)$ in the same way as $\Sigma(p)$ in Eq. (4.85), one finds (up to NLO) [61]

$$\begin{aligned} \hat{\Sigma}^R(p^2) &= \Sigma^R(p^2) + \delta Z^R, \\ \hat{\Sigma}^L(p^2) &= \Sigma^L(p^2) + \delta Z^L, \\ \hat{\Sigma}^S(p^2) &= \Sigma^S(p^2) - \frac{1}{2} (\delta Z^R + \delta Z^L) - \frac{\delta m}{m}. \end{aligned} \quad (4.88)$$

¹¹ Note that $\Sigma(p)$ receives overall factors of the field-strength renormalization when computed in the renormalized theory. However, since $\Sigma(p)$ is already of NLO, these additional Z -factors have no effect at NLO: $\Sigma(p) \rightarrow (Z \text{ factors}) \cdot \Sigma(p) = \Sigma(p) + \mathcal{O}(\delta^2)$, where $\mathcal{O}(\delta^2)$ stands for next-to-next-to-leading-order (NNLO) contributions.

The on-shell renormalization conditions for the full inverse renormalized fermion propagator $\hat{G}^{-1}(p)$ read [61]¹²

$$\operatorname{Re} \left(i\hat{G}^{-1}(p) \right) u(p) \Big|_{p^2=m^2} \stackrel{!}{=} 0, \quad (4.90)$$

$$\frac{\not{p} + m}{p^2 - m^2} \operatorname{Re} \left(i\hat{G}^{-1}(p) \right) u(p) \Big|_{p^2 \rightarrow m^2} \stackrel{!}{=} u(p). \quad (4.91)$$

Plugging in the propagator in terms of the renormalized 1PI function $\hat{\Sigma}(p)$ decomposed as in Eq. (4.85), the first renormalization condition (4.90) yields, exploiting the Dirac equation,

$$\begin{aligned} & \operatorname{Re} \left(P_L \left(m\hat{\Sigma}^R(p^2) + m\hat{\Sigma}^S(p^2) \right) + P_R \left(m\hat{\Sigma}^L(p^2) + m\hat{\Sigma}^S(p^2) \right) \right) u(p) \Big|_{p^2=m^2} \stackrel{!}{=} 0 \\ \implies & \operatorname{Re} \left(\hat{\Sigma}^R(m^2) + \hat{\Sigma}^S(m^2) \right) \stackrel{!}{=} 0, \quad \operatorname{Re} \left(\hat{\Sigma}^L(m^2) + \hat{\Sigma}^S(m^2) \right) \stackrel{!}{=} 0. \end{aligned} \quad (4.92)$$

The second renormalization condition (4.91) yields

$$\begin{aligned} & \frac{1}{p^2 - m^2} \operatorname{Re} \left(p^2 - m^2 + P_R \left(p^2\hat{\Sigma}^R(p^2) + m^2\hat{\Sigma}^L(p^2) + 2m^2\hat{\Sigma}^S(p^2) \right) \right. \\ & \left. + P_L \left(p^2\hat{\Sigma}^L(p^2) + m^2\hat{\Sigma}^R(p^2) + 2m^2\hat{\Sigma}^S(p^2) \right) \right) u(p) \Big|_{p^2 \rightarrow m^2} \stackrel{!}{=} u(p), \end{aligned} \quad (4.93)$$

where the Dirac equation was used again.

In order to satisfy this equation, the first and second orders of the Taylor expansions around $p^2 \approx m^2$ of the two brackets after P_R and P_L , respectively, have to vanish. The first order already vanishes by the conditions (4.92). The second order vanishes if

$$\begin{aligned} & \operatorname{Re} \frac{\partial}{\partial p^2} \left(p^2\hat{\Sigma}^R(p^2) + m^2\hat{\Sigma}^L(p^2) + 2m^2\hat{\Sigma}^S(p^2) \right) \Big|_{p^2=m^2} \stackrel{!}{=} 0, \\ & \operatorname{Re} \frac{\partial}{\partial p^2} \left(p^2\hat{\Sigma}^L(p^2) + m^2\hat{\Sigma}^R(p^2) + 2m^2\hat{\Sigma}^S(p^2) \right) \Big|_{p^2=m^2} \stackrel{!}{=} 0. \end{aligned} \quad (4.94)$$

¹² In QED, it follows from the Källén–Lehmann spectral decomposition that

$$\hat{G}(\not{p}) \stackrel{!}{=} i \frac{\not{p} + m}{p^2 - m^2} = (-i(\not{p} - m))^{-1} \quad \text{for} \quad \not{p} \rightarrow m, \quad (4.89)$$

similar to Eq. (4.8) [34]. The fact that $\hat{G}(\not{p})$ has a pole at $\not{p} \rightarrow m$ implies $\hat{G}^{-1}(\not{p}) = 0$ for $\not{p} \rightarrow m$ or, equivalently, Eq. (4.90). The form of the pole of the propagator (that is, its residue) implies $\hat{G}^{-1}(\not{p}) = -i(\not{p} - m) \iff (\not{p} + m)/(p^2 - m^2) i\hat{G}^{-1}(\not{p}) = 1$ for $\not{p} \rightarrow m$ or, equivalently, Eq. (4.91). The appearance of the real parts is discussed above Eq. (4.22).

Plugging in the relations (4.88), the conditions (4.92) and (4.94) can be transformed to

$$\begin{aligned} \operatorname{Re} \left(\left(\frac{\Sigma^R(m^2) + \delta Z^R}{\Sigma^L(m^2) + \delta Z^L} \right) + \Sigma^S(m^2) - \frac{1}{2}(\delta Z^R + \delta Z^L) - \frac{\delta m}{m} \right) &\stackrel{!}{=} 0, \\ \operatorname{Re} \left(\left(\frac{\Sigma^R(m^2) + \delta Z^R}{\Sigma^L(m^2) + \delta Z^L} \right) + m^2 \frac{\partial}{\partial p^2} (\Sigma^R(p^2) + \Sigma^L(p^2) + 2\Sigma^S(p^2)) \Big|_{p^2=m^2} \right) &\stackrel{!}{=} 0, \end{aligned} \quad (4.95)$$

respectively. These four equations can be solved consistently for the three counterterms [61]:

$$\begin{aligned} \delta m &= \frac{1}{2} m \operatorname{Re} (\Sigma^R(m^2) + \Sigma^L(m^2) + 2\Sigma^S(m^2)), \\ \delta Z^R &= -\operatorname{Re} \Sigma^R(m^2) - m^2 \operatorname{Re} \frac{\partial}{\partial p^2} (\Sigma^R(p^2) + \Sigma^L(p^2) + 2\Sigma^S(p^2)) \Big|_{p^2=m^2}, \\ \delta Z^L &= -\operatorname{Re} \Sigma^L(m^2) - m^2 \operatorname{Re} \frac{\partial}{\partial p^2} (\Sigma^L(p^2) + \Sigma^R(p^2) + 2\Sigma^S(p^2)) \Big|_{p^2=m^2}, \end{aligned} \quad (4.96)$$

where it was used that the counterterms are real.

4.8 Renormalization of the Gauge Sector

The starting point for the derivation of the on-shell counterterms has been the full propagator G for both the scalar fields and the fermion fields (see Eqs. (4.7), (4.25) and (4.82)). The derivation of these full propagators can be found in many QFT textbooks, which is why they were omitted in this work. On the other hand, textbooks rarely provide a derivation of the full propagator of massive gauge bosons. In Sec. 4.8.1 this derivation is presented, before the counterterms of the gauge sector are deduced in Sec. 4.8.2.

4.8.1 The Full Gauge Boson Propagator

In order to derive the full gauge boson propagator, let us first introduce the following notations: Let $\Delta_T^{\mu\nu}$ and $\Delta_L^{\mu\nu}$ be the transversal and longitudinal Lorentz structures, respectively, and let d_{Ta} and d_{La} be the transversal and longitudinal propagator denominators of a gauge boson a with mass m_a . More specifically, these quantities are introduced as¹³

$$\Delta_X^{\mu\nu} \equiv \begin{cases} g^{\mu\nu} - \frac{p^\mu p^\nu}{p^2}, & \text{for } X = T, \\ \frac{p^\mu p^\nu}{p^2}, & \text{for } X = L, \end{cases} \quad d_{Xa} \equiv \begin{cases} \frac{1}{p^2 - m_a^2}, & \text{for } X = T, \\ \frac{\xi}{p^2 - \xi m_a^2}, & \text{for } X = L, \end{cases} \quad (4.97)$$

where ξ is the gauge parameter of the R_ξ gauge. Note that the object $\Delta_X^{\mu\nu}$ has the property

$$\Delta_X^{\mu\sigma} \Delta_{Y,\sigma\nu} = \Delta_{X,\nu}^\mu \delta_{XY} = \begin{cases} 0, & \text{for } X \neq Y, \\ \Delta_{X,\nu}^\mu, & \text{for } X = Y. \end{cases} \quad (4.98)$$

¹³ The full propagator is derived in terms of the bare quantities. We will drop the indices zero in this section for simplicity. As soon as distinguishing between bare and physical parameters becomes relevant (which will be the case in Sec. 4.8.2), bare parameters will be equipped with an index 0 again.

In the R_ξ gauge, the kinetic and mass terms in the Lagrangian for the massive gauge bosons read [34]

$$\mathcal{L} \supset -\frac{1}{2} \mathcal{V}_\mu^a \left(\delta_{ab} \left(-g^{\mu\nu} \square + \left(1 - \frac{1}{\xi} \right) \partial^\mu \partial^\nu \right) - m_{ab}^2 g^{\mu\nu} \right) \mathcal{V}_\nu^b. \quad (4.99)$$

m_{ab}^2 is the mass matrix in the gauge basis; diagonalizing it turns the gauge eigenstates \mathcal{V}_μ^a into the mass eigenstates $V_\mu^a \in \{W_\mu^\pm, Z_\mu, A_\mu\}$ (a indicates the type of the gauge boson) with masses m_a^2 . Eq. (4.99) then reads

$$\mathcal{L} \supset -\frac{1}{2} \sum_{a,b} V_\mu^a \left(\delta_{ab} \left(-g^{\mu\nu} \square + \left(1 - \frac{1}{\xi} \right) \partial^\mu \partial^\nu \right) - \delta_{ab} m_a^2 g^{\mu\nu} \right) V_\nu^b. \quad (4.100)$$

The inverse Feynman propagator $D_{ab}^{-1,\mu\nu}(p)$ can be obtained by performing a Fourier transformation on the large bracket in Eq. (4.100) [34]:

$$\begin{aligned} -iD_{ab}^{-1,\mu\nu}(p) &= \delta_{ab} \left(g^{\mu\nu} p^2 - \left(1 - \frac{1}{\xi} \right) p^\mu p^\nu \right) - \delta_{ab} m_a^2 g^{\mu\nu} \\ &= \delta_{ab} \left(g^{\mu\nu} - \frac{p^\mu p^\nu}{p^2} \right) (p^2 - m_a^2) + \delta_{ab} \frac{p^\mu p^\nu}{p^2} \frac{1}{\xi} (p^2 - \xi m_a^2) \\ &= \delta_{ab} d_{Xa}^{-1} \Delta_X^{\mu\nu}, \end{aligned} \quad (4.101)$$

where a sum is implicit over $X \in T, L$ according to the Einstein summation convention. Inverting this expression gives the Feynman propagator,

$$iD_{ab}^{\mu\nu}(p) = \delta_{ab} d_{Xa} \Delta_X^{\mu\nu}, \quad (4.102)$$

since

$$-iD_{ac}^{-1,\mu\sigma} iD_{cb,\sigma\nu} = \sum_{c,X,Y} (\delta_{ac} d_{Xa}^{-1} \Delta_X^{\mu\sigma}) (\delta_{cb} d_{Yc} \Delta_{Y,\sigma\nu}) = \delta_{ab} \sum_X \Delta_{X,\nu}^\mu = \delta_{ab} g_\nu^\mu. \quad (4.103)$$

The last step follows immediately from the definitions (4.97).

Let $i\Sigma_{ab}^{\mu\nu}(p)$ be the sum of all 1PI diagrams of the gauge boson propagator,

$$i\Sigma_{ab}^{\mu\nu}(p) = a, \mu \text{ --- } \textcircled{\text{1PI}} \text{ --- } b, \nu. \quad (4.104)$$

Due to the mixing of the Z boson and the photon, the corresponding off-diagonal terms $\Sigma_{Z\gamma}^{\mu\nu}(p)$ and $\Sigma_{\gamma Z}^{\mu\nu}(p)$ are non-zero. Since the Lorentz indices of $\Sigma_{ab}^{\mu\nu}(p)$ can only be carried by the metric $g^{\mu\nu}$ or two four-momenta $p^\mu p^\nu$, the 1PI function must be of the form

$$i\Sigma_{ab}^{\mu\nu}(p) = A_{ab}(p^2) g^{\mu\nu} + B_{ab}(p^2) p^\mu p^\nu. \quad (4.105)$$

Rather than into terms proportional to $g^{\mu\nu}$ and $p^\mu p^\nu$, we equivalently split the 1PI function into transversal and longitudinal contributions $\Sigma_{ab}^{T,\mu\nu}(p)$ and $\Sigma_{ab}^{L,\mu\nu}(p)$ – proportional to $\Delta_T^{\mu\nu}$

and $\Delta_L^{\mu\nu}$, respectively,

$$\Sigma_{ab}^{\mu\nu}(p) = \Sigma_{ab}^{T,\mu\nu}(p) + \Sigma_{ab}^{L,\mu\nu}(p) \equiv \Delta_T^{\mu\nu} \Sigma_{ab}^T(p^2) + \Delta_L^{\mu\nu} \Sigma_{ab}^L(p^2). \quad (4.106)$$

In order to compute the full propagator $G_{ab}^{\mu\nu}(p)$, let us introduce one more abbreviation,

$$\tilde{\Sigma}_{ab}^X(p^2) \equiv d_{Xb} \Sigma_{ab}^X(p^2). \quad (4.107)$$

The full propagator is then given by¹⁴

$$\begin{aligned} G_{ab}^{\mu\nu}(p) &= \text{wavy line} + \text{wavy line} \circlearrowleft \text{1PI} \text{wavy line} + \text{wavy line} \circlearrowleft \text{1PI} \circlearrowleft \text{1PI} \text{wavy line} + \dots \\ &= D_{ab}^{\mu\nu}(p) + \sum_{c,d} (D_{ac}^{\mu\rho}(p) i\Sigma_{cd,\rho\sigma}(p) D_{db}^{\sigma\nu}(p)) \\ &\quad + \sum_{c,d,e,f} (D_{ac}^{\mu\rho}(p) i\Sigma_{cd,\rho\sigma}(p) D_{de}^{\sigma\eta}(p) i\Sigma_{ef,\eta\kappa}(p) D_{fb}^{\kappa\nu}(p)) + \dots \end{aligned} \quad (4.108)$$

Plugging in Eq. (4.102) and (4.106), the second term of Eq. (4.108) can be rewritten as

$$\begin{aligned} &\sum_{c,d} D_{ac}^{\mu\rho}(p) i\Sigma_{cd,\rho\sigma}(p) D_{db}^{\sigma\nu}(p) \\ &= \sum_{c,d} (-i\delta_{ac} d_{Xa} \Delta_X^{\mu\rho}) i(\Delta_{Y,\rho\sigma} \Sigma_{cd}^Y(p^2)) (-i\delta_{db} d_{Zb} \Delta_Z^{\sigma\nu}) \\ &= (-id_{Xa} \Delta_X^{\mu\rho}) \sum_Y (\Delta_{Y,\rho}^\nu \delta_Y d_{Zb} \Sigma_{ab}^Y(p^2)) \\ &= (-id_{Xa} \Delta_X^{\mu\rho}) (\Delta_{Y,\rho}^\nu \tilde{\Sigma}_{ab}^Y(p^2)). \end{aligned} \quad (4.109)$$

Here, also the property from Eq. (4.98) as well as the definition (4.107) was used. Similar transformations are possible for the third (and all further) terms, such that the full propagator reads

$$\begin{aligned} G_{ab}^{\mu\nu}(p) &= -id_{Xa} \Delta_X^{\mu\rho} \left(\delta_{ab} g_\rho^\nu + \Delta_{Y,\rho}^\nu \tilde{\Sigma}_{ab}^Y(p^2) + \sum_c (\Delta_{Y,\rho}^\eta \tilde{\Sigma}_{ac}^Y(p^2)) (\Delta_{Z,\eta}^\nu \tilde{\Sigma}_{cb}^Z(p^2)) + \dots \right) \\ &= \sum_X (-id_{Xa} \Delta_X^{\mu\nu}) \left(\delta_{ab} + \tilde{\Sigma}_{ab}^X(p^2) + \sum_c \tilde{\Sigma}_{ac}^X(p^2) \tilde{\Sigma}_{cb}^X(p^2) + \dots \right) \\ &= \sum_X (-id_{Xa} \Delta_X^{\mu\nu}) \left(\frac{1}{1 - \tilde{\Sigma}^X(p^2)} \right)^{ab}. \end{aligned} \quad (4.110)$$

¹⁴ The gauge indices a, b, c are *not* summed over implicitly by the Einstein summation convention in this derivation, but only if indicated explicitly by a sum symbol. On the other hand, a sum over the transversal/longitudinal indices X, Y, Z is implied in accordance with the Einstein summation convention – a sum over these indices is indicated explicitly only if there are more or less than two such indices to be summed over, where the Einstein summation convention does not imply a sum.

In the last step the geometric series for matrices was used [62].

The inverse of this full propagator is given by¹⁵

$$-iG_{ab}^{-1,\mu\nu}(p) = \sum_X d_{Xb}^{-1} \Delta_X^{\mu\nu} (\delta_{ab} - \tilde{\Sigma}_{ab}^X(p^2)) = \sum_X \Delta_X^{\mu\nu} (\delta_{ab} d_{Xb}^{-1} - \Sigma_{ab}^X(p^2)), \quad (4.111)$$

since with this expression one finds

$$\sum_c G_{ac}^{-1,\mu\sigma} G_{cb,\sigma\nu} = g_\nu^\mu \delta_{ab}. \quad (4.112)$$

4.8.2 Counterterms in the Gauge Sector

The mass eigenstates of the Z boson Z^μ and of the photon A^μ are rotated from their gauge eigenstates in the same way as the Higgs mass eigenstates h_1 and h_2 are rotated from their gauge eigenstates h and s . Thus, the bare fields of the Z boson and the photon are connected to the renormalized fields by a field-strength renormalization matrix \mathcal{Z} ,

$$\begin{pmatrix} Z_0^\mu \\ A_0^\mu \end{pmatrix} = \sqrt{\mathcal{Z}} \begin{pmatrix} Z^\mu \\ A^\mu \end{pmatrix} \approx \left(1 + \frac{1}{2} \delta\mathcal{Z}\right) \begin{pmatrix} Z^\mu \\ A^\mu \end{pmatrix}, \quad (4.113)$$

exactly as it was the case for the Higgs bosons in Eq. (4.24). On the other hand, the W^\pm bosons are each other's antiparticles and therefore have the same field-strength renormalization constant Z_W :

$$W_0^{\pm,\mu} = \sqrt{Z_W} W^{\pm,\mu}. \quad (4.114)$$

Hence, writing the field-strength renormalization constants \mathcal{Z} and Z_W into a 4×4 matrix \mathcal{A} , all matrices $\mathcal{A} = G^{\mu\nu}, \hat{G}^{\mu\nu}, \hat{\Sigma}, \Sigma, \mathcal{Z}$ are diagonal except for a 2×2 block in the lower right corner:

$$\mathcal{A} = \begin{pmatrix} \mathcal{A}_{WW} & 0 & 0 & 0 \\ 0 & \mathcal{A}_{WW} & 0 & 0 \\ 0 & 0 & \mathcal{A}_{ZZ} & \mathcal{A}_{Z\gamma} \\ 0 & 0 & \mathcal{A}_{\gamma Z} & \mathcal{A}_{\gamma\gamma} \end{pmatrix}. \quad (4.115)$$

The inverse full propagator in Eq. (4.111) is computed in terms of bare quantities and technically all the parameters it contains need to be equipped with an index 0. It is related to the corresponding renormalized full propagator $\hat{G}_{ab}^{\mu\nu}$ by

$$-i\hat{G}^{-1,\mu\nu}(p) = \sqrt{\mathcal{Z}}^\dagger (-iG^{-1,\mu\nu}(p)) \sqrt{\mathcal{Z}}, \quad (4.116)$$

where the propagators as well as the field-strength renormalizations are 4×4 matrices in gauge space. This equation is completely analogous to Eq. (4.25) from the scalar case.

Plugging in Eq. (4.111) and expanding the parameters in physical terms and counterterms

¹⁵ Except for defining $\Sigma(p^2)$ with a different overall sign, this corresponds to the equation in [56] and is the generalization to a general gauge for the result given in [63].

(note that $d_{Xa0}^{-1} = d_{Xa}^{-1} - \delta m_a^2$), it follows from Eq. (4.116) that

$$\begin{aligned}
& \sum_{c,d} \sqrt{Z_{ac}^\dagger} \left(-iG_{cd}^{-1,\mu\nu}(p) \right) \sqrt{Z_{db}} \\
&= \sum_{X,c,d} \left(\delta_{ac} + \frac{1}{2} \delta Z_{ac}^\dagger \right) \Delta_X^{\mu\nu} \left(\delta_{cd} (d_{Xd}^{-1} - \delta m_d^2) - \Sigma_{cd}^X(p^2) \right) \left(\delta_{db} + \frac{1}{2} \delta Z_{db} \right) \\
&= \sum_X \Delta_X^{\mu\nu} \left(\delta_{ab} d_{Xb}^{-1} - \Sigma_{ab}^X(p^2) - \delta_{ab} \delta m_a^2 + \frac{1}{2} d_{Xa}^{-1} \delta Z_{ab} + \frac{1}{2} d_{Xb}^{-1} \delta Z_{ab}^\dagger \right) \\
&\stackrel{!}{=} \sum_X \Delta_X^{\mu\nu} \left(\delta_{ab} d_{Xb}^{-1} - \hat{\Sigma}_{ab}^X(p^2) \right) = -i\hat{G}_{ab}^{-1,\mu\nu}(p).
\end{aligned} \tag{4.117}$$

Here, $\hat{\Sigma}_{ab}^X$ is the renormalized counterpart to Σ_{ab}^X , exactly as it was in the scalar case (see Eq. (4.19)). Since $\Delta_X^{\mu\nu}$ is orthogonal in the X space according to Eq. (4.98), one may solve for both the transverse and the longitudinal parts individually, which yields

$$\hat{\Sigma}_{ab}^X(p^2) = \Sigma_{ab}^X(p^2) + \delta_{ab} \delta m_a^2 - \frac{1}{2} d_{Xa}^{-1} \delta Z_{ab} - \frac{1}{2} d_{Xb}^{-1} \delta Z_{ab}^\dagger. \tag{4.118}$$

Imposing renormalization conditions on the transversal contributions is sufficient to fix all counterterms. The on-shell renormalization conditions on the transversal contributions of the renormalized 1PI function $\hat{\Sigma}_{ab}^T(p)$ can be derived just as in the scalar case (see Eqs. (4.29)–(4.35)) and yield

$$\text{Re } \hat{\Sigma}_{aa}^T(m_a^2) \stackrel{!}{=} 0, \quad \text{for } a = W, Z, \gamma, \tag{4.119}$$

$$\text{Re } \left. \frac{\partial \hat{\Sigma}_{aa}^T(p^2)}{\partial p^2} \right|_{p^2=m_a^2} \stackrel{!}{=} 0, \quad \text{for } a = W, Z, \gamma, \tag{4.120}$$

$$\text{Re } \hat{\Sigma}_{Z\gamma}^T(m_a^2) = \text{Re } \hat{\Sigma}_{\gamma Z}^T(m_a^2) \stackrel{!}{=} 0, \quad \text{for } a = Z, \gamma. \tag{4.121}$$

Of course, $m_\gamma^2 = 0$. Employing these conditions on Eq. (4.118), the counterterms can be fixed as follows:

$$\delta m_a^2 = -\text{Re } \Sigma_{aa}^T(m_a^2), \quad \text{for } a = W, Z, \tag{4.122}$$

$$\delta Z_{aa} = \text{Re } \left. \frac{\partial \Sigma_{aa}^T(p^2)}{\partial p^2} \right|_{p^2=m_a^2}, \quad \text{for } a = W, Z, \gamma, \tag{4.123}$$

$$\delta Z_{Z\gamma} = -\frac{2}{m_Z^2} \text{Re } \Sigma_{Z\gamma}^T(0), \tag{4.124}$$

$$\delta Z_{\gamma Z} = \frac{2}{m_Z^2} \text{Re } \Sigma_{Z\gamma}^T(m_Z^2). \tag{4.125}$$

Note that $\Sigma_{ab}^T(p^2) = \Sigma_{ba}^T(p^2)$, but $\delta Z_{ab} \neq \delta Z_{ba}$.

By definition, the elementary charge e is the coupling constant of the fermion–fermion–photon vertex. During renormalization, the bare elementary charge is split into a physical

term and a counterterm similarly to all other parameters:

$$e_0 = \frac{1}{Z_e} e \approx e - \frac{1}{2} \delta Z_e e. \quad (4.126)$$

Since each such kind of a vertex has precisely one external photon, in QED the charge renormalization can be used to cancel the (infinite) field-strength renormalization factor of the photon field $\delta Z_{\gamma\gamma}$ by choosing [34]

$$\delta Z_e = \delta Z_{\gamma\gamma}, \quad (4.127)$$

such that the sum in Fig. 4.3 is finite.

In the electroweak theory, however, the photon and the Z boson states mix at one-loop order and a photon can couple to a fermion through a Z propagator [64], as displayed in Fig. 4.4. Since this is an additional possibility for a photon to couple to a fermion, an additional term in δZ_e is required in order to cancel its infinities.

Note that the expression for the diagram in Fig. 4.4 can be derived from the first diagram in Fig. 4.3 by exchanging the full propagator $G_{\gamma\gamma}^{\mu\nu} \rightarrow G_{\gamma Z}^{\mu\nu}$ and by replacing the coupling factor of the photon–fermion–fermion vertex by the Z boson–fermion–fermion vertex. The latter is given by $g \sin^2 \theta_w / \cos \theta_w$.¹⁶ Hence, the two diagrams can be related as it is shown in Fig. 4.4

Thus, including the additional contribution that is required to cancel the full mixing propagator, δZ_e is given by [65]¹⁷

$$\delta Z_e = \delta Z_{\gamma\gamma} + \frac{1}{e} \frac{g \sin^2 \theta_w}{\cos \theta_w} \cdot \delta Z_{\gamma\gamma} \Big|_{\delta Z_{\gamma\gamma} \rightarrow \delta Z_{\gamma Z}} = \operatorname{Re} \frac{\partial \Sigma_{\gamma\gamma}^T(p^2)}{\partial p^2} \Big|_{p^2=0} - \frac{2}{m_Z^2} \frac{\sin \theta_w}{\cos \theta_w} \operatorname{Re} \Sigma_{\gamma Z}^T(0). \quad (4.128)$$

Here, Eqs. (4.123), (4.124) and $e = g \sin \theta_w$ [34] were used.

Writing the weak coupling as [34]

$$g = \frac{e}{\sqrt{1 - m_W^2/m_Z^2}}, \quad (4.129)$$



Figure 4.3: The QED vertex counterterm cancels the propagator correction of the photon if $\delta Z_e = \delta Z_{\gamma\gamma}$.

¹⁶ As a matter of fact, this is only the part of the coupling that is equal for left- and right-handed fermions [34]. Due to the Ward–Takahashi identity, all other contributions to this coupling vanish [64, 65].

¹⁷ Note that in [65], the definitions of δZ_e differ by a factor of $-1/2$ and the definitions of the 1PI functions by a factor of -1 .

$$\begin{array}{c} \text{Diagram 1} \\ \text{Diagram 2} \end{array} = \frac{1}{e \cos \theta_w} \cdot \begin{array}{c} \text{Diagram 3} \\ \text{Diagram 4} \end{array} \Big|_{G_{\gamma\gamma}^{\mu\nu} \rightarrow G_{\gamma Z}^{\mu\nu}}.$$

Figure 4.4: In the electroweak theory, the photon can couple to a fermion also through a Z boson. The expression of the corresponding diagram can be related to the expression of the diagram where a photons couples to the fermion.

its counterterm can be given as

$$\frac{\delta g}{g} = -\frac{1}{2}\delta Z_e + \frac{1}{2(m_Z^2 - m_W^2)} (\delta m_W^2 - \cos^2 \theta_w \delta m_Z^2), \quad (4.130)$$

with the mass counterterms being given in Eq. (4.122).

4.9 $\bar{q}q$ -Higgs Vertex Renormalization

The term in the Lagrangian that describes the vertex of a quark q , antiquark \bar{q} and a Higgs boson h_i reads

$$\mathcal{L} \supset D_{i0} h_{i0} (\bar{q}_0^R q_0^L + \bar{q}_0^L q_0^R), \quad (4.131)$$

where, using $v_0 = 2m_{W0}/g_0$ [34],

$$D_{10} = -\frac{m_{q0} \cos \alpha_0}{v_0} = -\frac{g_0 m_{q0} \cos \alpha_0}{2m_{W0}}, \quad D_{20} = \frac{m_{q0} \sin \alpha_0}{v_0} = \frac{g_0 m_{q0} \sin \alpha_0}{2m_{W0}}. \quad (4.132)$$

Writing these bare vertex factors as a sum of a physical term and a counterterm,

$$D_{i0} = D_i + \delta D_i, \quad (4.133)$$

the counterterms can be expressed as

$$\begin{aligned} \delta D_1 &= \frac{gm_q}{2m_W} \left(\sin \alpha \delta \alpha + \cos \alpha \left(\frac{\delta m_W^2}{2m_W^2} - \frac{\delta g}{g} - \frac{\delta m_q}{m_q} \right) \right), \\ \delta D_2 &= \frac{gm_q}{2m_W} \left(\cos \alpha \delta \alpha - \sin \alpha \left(\frac{\delta m_W^2}{2m_W^2} - \frac{\delta g}{g} - \frac{\delta m_q}{m_q} \right) \right). \end{aligned} \quad (4.134)$$

The bare coupling terms in Eq. (4.131) can be turned into renormalized coupling terms as

$$D_{i0} h_{i0} (\bar{q}_0^R q_0^L + \bar{q}_0^L q_0^R) = \hat{D}_i h_i (\bar{q}^R q^L + \bar{q}^L q^R), \quad (4.135)$$

where plugging in the expansions (4.133), (4.24) and (4.80) leads to

$$\hat{D}_i = D_i + \delta D_i + \underbrace{\frac{1}{2} D_j \delta Z_{ji} + \frac{1}{2} D_i (\delta Z^R + \delta Z^L)}_{\equiv \delta D_i^{\text{mix}}}. \quad (4.136)$$

4.10 Overview: Counter Propagators and Vertices

In the beginning of this chapter the goal was set to compute the counterterms in Fig. 4.2. This section aims for presenting the results for these counterterms that have been derived in detail in the previous sections.

As it becomes obvious by comparing Eqs. (4.15) and (4.17), the counterterm propagator is the difference between the bare 1PI function Σ or Ξ and the renormalized 1PI function $\hat{\Sigma}$ or $\hat{\Xi}$. Using Eq. (4.36), the counterterm propagators for the Higgs boson read

$$\begin{aligned} h_i \text{---}\textcircled{\otimes}\text{---} h_i &= i \left((p^2 - m_i^2) \delta Z_{ii} - \delta m_i^2 - \delta T_{ii} \right), \\ h_i \text{---}\textcircled{\otimes}\text{---} h_j &= \frac{i}{2} \left((p^2 - m_i^2) \delta Z_{ij} + (p^2 - m_j^2) \delta Z_{ji} - 2 \delta T_{ij} \right), \quad \text{for } i \neq j. \end{aligned} \quad (4.137)$$

Similarly, for the DM–Higgs boson vertex and for the quark–Higgs boson vertex it follows from Eqs. (4.77) and (4.136) that

$$\begin{aligned} \chi \text{---}\textcircled{\otimes}\text{---} \chi &= \delta C_i + \delta C_i^{\text{mix}}, \\ q \text{---}\textcircled{\otimes}\text{---} q &= \delta D_i + \delta D_i^{\text{mix}}. \end{aligned} \quad (4.138)$$

To make sense out of the expressions (4.137)–(4.138), the reader is referred to all the formulas for the diverse counterterms that have been derived in this chapter:

| | | | |
|--|-----------------|------------------------------|-----------------|
| $\delta Z_{11}, \delta Z_{22}$ | see Eq. (4.37) | δT_i | see Eq. (4.49) |
| $\delta m_i^2, \delta Z_{12}, \delta Z_{21}$ | see Eq. (4.58) | $\delta \alpha$ | see Eq. (4.67) |
| δT_{ij} | see Eq. (4.57) | δZ_χ | see Eq. (4.71) |
| δC_i | see Eq. (4.75) | $\delta m_W^2, \delta m_Z^2$ | see Eq. (4.122) |
| δC_i^{mix} | see Eq. (4.77) | δg | see Eq. (4.130) |
| δD_i | see Eq. (4.134) | δZ_e | see Eq. (4.128) |
| δD_i^{mix} | see Eq. (4.136) | $\delta m_q, dZ^R, dZ^L$ | see Eq. (4.96) |

Using these formulas it is possible to express all the diagrams (4.137)–(4.138) in terms of free parameters and the following 1PI functions (and their derivatives) only:

| | | |
|-------------------|--|---------------------|
| Higgs propagator: | $i\Sigma_{ij}(p^2) = h_i \text{---}\textcircled{\text{1PI}}\text{---} h_j$ | Sec. 4.2, Fig. 4.6, |
| Higgs tadpole: | $i\Xi_i = h_i \text{---}\textcircled{\text{1PI}}$ | Sec. 4.3, Fig. 4.7, |
| DM propagator: | $i\Sigma_\chi(p^2) = \chi \text{---}\textcircled{\text{1PI}}\text{---} \chi$ | Sec. 4.5, Fig. 4.8, |

fermion propagator: $i\Sigma(p) = f \rightarrow \text{1PI} \rightarrow f$ Sec. 4.7, Fig. 4.9,

gauge boson propagator: $i\Sigma_{ab}^{\mu\nu}(p) = a, \mu \sim \text{1PI} \sim b, \nu$ Sec. 4.8. Fig. 4.10.

The functions $\Sigma^R(p^2)$, $\Sigma^L(p^2)$ and $\Sigma^S(p^2)$ that appear in the formulas for δm_q , δZ^R and δZ^L (4.96) are the different contributions to the fermion 1PI function $i\Sigma(p)$ according to Eq. (4.85). Note that the difference in having bare or renormalized fields on the external lines in these diagrams is merely a factor Z ; since the 1PI diagrams are already of NLO, such a factor would only contribute to NNLO. The specific diagrams that contribute to these 1PI functions at one-loop order are given in Figs. 4.6–4.10.

Note that the total amplitude is independent of the factors δZ_{ij} of the internal Higgs bosons. That is, these factors cancel completely in the sum of the tree diagrams in Fig. 4.5.

$$\sum_{i,j} \begin{array}{c} \chi \text{---} \overline{h}_i \text{---} \chi \\ | \\ \text{---} \otimes \text{---} \\ | \\ q \text{---} \overline{h}_j \text{---} q \end{array} + \sum_i \begin{array}{c} \chi \text{---} \otimes \text{---} \chi \\ | \\ \text{---} h_i \text{---} \\ | \\ q \text{---} \text{---} q \end{array} + \sum_i \begin{array}{c} \chi \text{---} \text{---} \chi \\ | \\ \text{---} h_i \text{---} \\ | \\ q \text{---} \otimes \text{---} q \end{array}$$

Figure 4.5: The field-strength renormalization factors Z_{ij} of the Higgs bosons that appear in all of the counterterms in Fig. 4.2 cancel completely when all counterterm diagrams are properly summed up.

Table 4.1: In Figs. 4.6–4.10 and 5.4–5.6, Φ_i is used as an abbreviation for certain sets of particles. Their definition is given in the list below. Here, η_Z and η^+ is the Faddeev–Popov ghost of the Z and W^+ boson, respectively. $f^+ = u, c, t, d, s, b, e, \mu, \tau$ is short for all charged fermions and $f = f^+, \nu_e, \nu_\mu, \nu_\tau$ for all fermions of the SM.

$$\begin{aligned}
\Phi_1 &= h_1, h_2, \chi, G^0, G^+, Z, W^+ \\
\Phi_2 &= \chi, G^0, G^+, Z, W^+, \eta_Z, \eta^+, f^+ \\
\Phi_3 &= h_1, h_2, \chi, G^0, G^+, Z, W^+, \eta_Z, \eta^+, f^+ \\
\Phi_4 &= h_1, h_2, \chi, G^0, G^+ \\
\Phi_5 &= h_1, h_2, G^0, G^+, \gamma, Z, W^+ \\
\Phi_6 &= G^+, W^+, \eta^+, f^+ \\
\Phi_7 &= h_1, h_2, G^0, G^+, W^+ \\
\Phi_8 &= G^+, W^+, \eta^+, f \\
\Phi_9 &= h_1, h_2, G^0, \gamma, Z \\
\Phi_{10} &= h_1, h_2, \gamma, Z \\
\Phi_{11} &= \chi, G^0, G^+ \\
\Phi_{12} &= G^0, G^+, Z, W^+
\end{aligned}$$

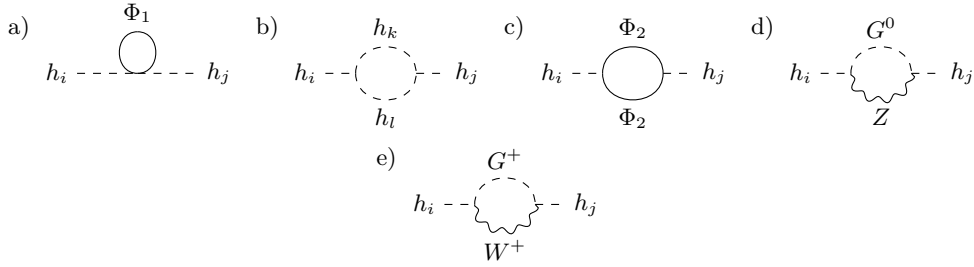


Figure 4.6: The one-loop corrections to the Higgs propagator; the 1PI function of the Higgs propagator $i\Sigma_{ij}(p^2)$ was computed as the sum of these diagrams. Here, $i, j, k, l = 1, 2$. For the definition of Φ_1 and Φ_2 see Tab. 4.1. For each combination of external Higgs bosons (i. e. each combination of i and j) one is left with 29 individual diagrams (note that the loop direction matters in diagram e, which doubles the number of diagrams of this type).

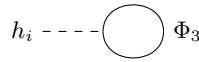


Figure 4.7: The one-loop corrections to the Higgs tadpole; the 1PI function of the Higgs tadpole $i\Xi_i(p^2)$ was computed as the sum of these diagrams. Here, $i = 1, 2$. For the definition of Φ_3 see Tab. 4.1. For each external Higgs h_i one is then left with 16 individual diagrams.

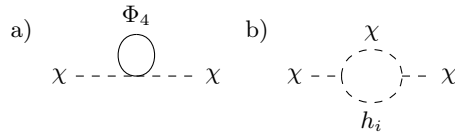


Figure 4.8: The one-loop corrections to the DM propagator; the 1PI function of the DM propagator $i\Sigma_\chi(p^2)$ was computed as the sum of these diagrams. Here, $i = 1, 2$. For the definition of Φ_4 see Tab. 4.1. In total one is left with 7 individual diagrams.

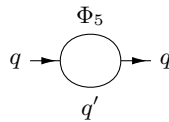


Figure 4.9: The one-loop electroweak corrections (there is also a QCD correction including a gluon, which is not taken into account) to the quark propagator; the 1PI function of the q propagator $i\Sigma(p)$ was computed as the sum of these diagrams. For the definition of Φ_5 see Tab. 4.1. In diagrams that include G^+ or W^+ particles, q' is the corresponding down-type quark for an up-type quark q and the corresponding up-type quark for a down-type quark q (in all other diagrams, $q' = q$). For each external quark q , one is left with 7 individual diagrams.

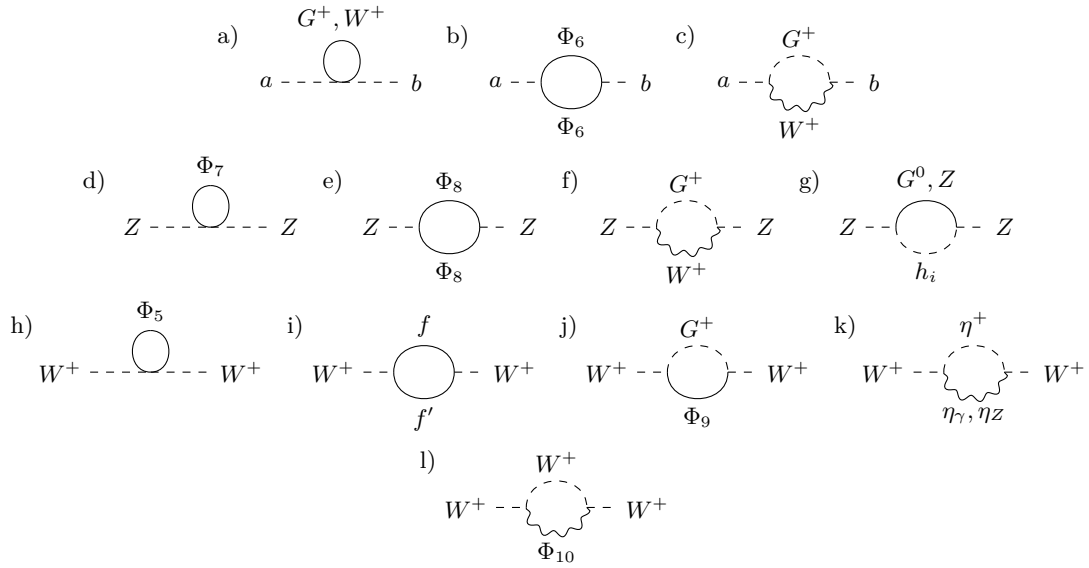


Figure 4.10: The one-loop corrections to the electroweak gauge boson propagator; the 1PI function of the gauge boson propagator $i\Sigma_{ab}^{\mu\nu}(p)$ was computed as a sum of these diagrams. Here, $(a, b) = (\gamma, \gamma), (\gamma, Z), (Z, \gamma)$. That is, the diagrams a–c contribute to $i\Sigma_{\gamma\gamma}^{\mu\nu}$, $i\Sigma_{\gamma Z}^{\mu\nu}$ and $i\Sigma_{Z\gamma}^{\mu\nu}$ only, but not to the 1PI functions of the Z and W^+ boson propagators. Their constituents are given by diagrams d–g and h–l, respectively. Here, $i = 1, 2$. For the definition of Φ_5 – Φ_{10} , f , η^+ , η_Z and η_γ see Tab. 4.1. If f is an up-type quark or a charged lepton, f' is the corresponding down-type quark or uncharged lepton, respectively, of the same generation (for example, $c' = s$, $\tau' = \nu_\tau$). For given a, b , a–c illustrate 16 individual diagrams, d–g correspond to 26 and h–l to 24 individual diagrams (note that the loop direction matters in diagrams c and f, which doubles the number of diagrams of this type).

CHAPTER 5

The Amplitude of Dark Matter Direct Detection in the DCxSM

Direct Detection experiments search for DM particles by aiming to measure their interactions with a target nucleus. In Chapter 3 it was worked out how the cross section for scattering with a nucleus can be related to scattering with a nucleon. Furthermore, in Sec. 3.4 a formalism was introduced for the computation of the scattering with a nucleon using Wilson coefficients as effective couplings between the DM particle and the elementary constituents of the nucleon: the quarks and gluons. In this chapter, we will present which diagrams are taken into account for the computation of the Wilson coefficients and which approximations are applied.

In the DCxSM, χ is the DM candidate. The interaction between χ and a quark or a gluon is schematically shown in Fig. 5.1. In Sec. 5.1, this process is examined at tree level. The NLO corrections to the process with external quarks are presented in Sec. 5.2. Higher-order diagrams with external gluons are considered in Sec. 5.3. Finally, it is shown in Sec. 5.4 how the amplitudes are matched to the effective Lagrangian of Eq. (3.24), i. e. how the Wilson coefficients are extracted.

5.1 Tree Level

At tree level, there are no diagrams where the DM particle χ scatters with a gluon g ; all tree-level contributions to the diagram in Fig. 5.1 are of the topology as shown in Fig. 4.1a. Only the Higgs bosons h_1 and h_2 are possible mediators, since only they are able to form a three-vertex with two χ particles according to Eq. (2.9) (using Eq. (2.13)). Hence, for a given quark q , the total amplitude for this process at tree level is given by

$$\begin{array}{c} \chi \text{ --- } \text{---} \chi \\ | \\ \text{---} h_1 \text{ ---} \\ | \\ q \text{ ---} \text{---} q \end{array} + \begin{array}{c} \chi \text{ --- } \text{---} \chi \\ | \\ \text{---} h_2 \text{ ---} \\ | \\ q \text{ ---} \text{---} q \end{array} = -i \frac{(m_1^2 - m_2^2) \cos \alpha \sin \alpha}{(t - m_1^2)(t - m_2^2) v v_S} m_q t \bar{u}(p_2) u(p_1), \quad (5.1)$$

where the parameters m_1 , m_2 , v , v_S and α have been introduced in Chapter 2. Furthermore, m_q is the quark mass, u is the quark spinor, \bar{u} is the antiquark spinor and p_1 and p_2 are the incoming and outgoing quark momenta, respectively, and $t = (p_2 - p_1)^2$ is the Mandelstam

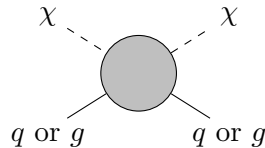


Figure 5.1: Schematic diagram of an interaction between a DM particle and a quark or gluon. The blob represents the sum of all possible diagrams with the corresponding external particles.

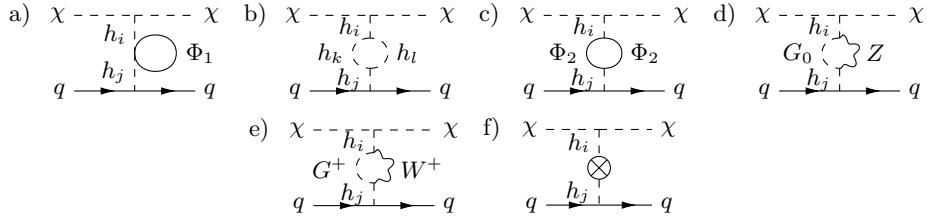


Figure 5.4: One-loop electroweak corrections to the h_i propagator. Here, $i, j, k, l = 1, 2$. For the definitions of Φ_1 and Φ_2 see Tab. 4.1. For each external quark q one is then left with 116 individual diagrams a–e (note that the loop direction matters in diagram e, which doubles the number of diagrams of this type). In addition, the four (for $i, j = 1, 2$) counter propagator diagrams f are required to renormalize these corrections.

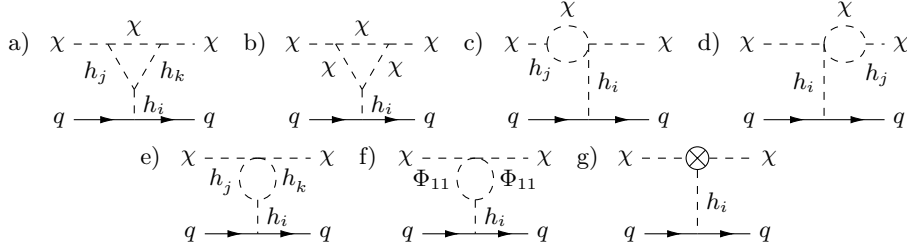


Figure 5.5: One-loop electroweak corrections to the $\chi\chi h_i$ vertex. Here, $i, j, k = 1, 2$. For the definition of Φ_{11} see Tab. 4.1. For each external quark q , one is then left with 32 individual diagrams a–f. In addition, the two (for $i = 1, 2$) counter vertex diagrams g are required to renormalize these corrections.

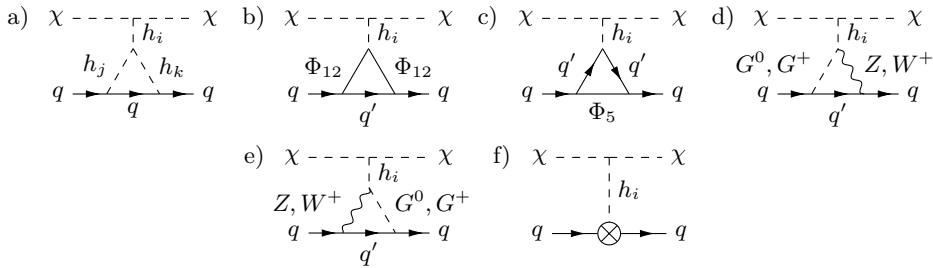


Figure 5.6: One-loop electroweak corrections to the $\bar{q}qh_i$ vertex. Here, $i, j, k = 1, 2$. For the definitions of Φ_5 and Φ_{12} see Tab. 4.1. In diagrams that include G^+ or W^+ particles, q' is the corresponding down-type quark for an up-type quark q and the corresponding up-type quark for a down-type quark q (in all other diagrams, $q' = q$). For each external quark q , one is left with 38 individual diagrams a–e. In addition, the two (for $i = 1, 2$) counter vertex diagrams f are required to renormalize these corrections.

given by

$$i\mathcal{M}_{ij}^{\square} = i^4 A_{ij} \bar{u}(p_2) \int \frac{d^4 q}{(2\pi)^4} \frac{1}{q^2 - m_i^2} \frac{1}{(p_1 - q)^2 - m_\chi^2} \frac{1}{q^2 - m_j^2} \cdot \left(\frac{\not{p}_2 + \not{q} + m_q}{(p_2 + q)^2 - m_q^2} + \frac{\not{p}_2 - \not{q} + m_q}{(p_2 - q)^2 - m_q^2} \right) u(p_2), \quad (5.3)$$

$$i\mathcal{M}_{ij}^{\triangle} = i^4 B_{ij} \bar{u}(p_2) \int \frac{d^4 q}{(2\pi)^4} \frac{1}{q^2 - m_i^2} \frac{1}{q^2 - m_j^2} \frac{\not{p}_2 + \not{q} + m_q}{(p_2 + q)^2 - m_q^2} u(p_2). \quad (5.4)$$

A_{ij} and B_{ij} are abbreviations for the couplings that occur in the diagrams in Fig. 5.7. It holds $A_{ij} = a_i a_j b_i b_j$ and $B_{ij} = a_i a_j b_{ij}$, if a_i , b_i and b_{ij} are the coefficients of $h_i \bar{q} q$, $h_i \chi^2$ and $h_i h_j \chi^2$ in the Lagrangian, respectively. Explicitly, they read

$$\begin{aligned} a_1 &= -i \frac{m_q \cos \alpha}{v}, & a_2 &= -i \frac{m_q \sin \alpha}{v}, & b_1 &= -i \frac{m_1^2 \sin \alpha}{v_S}, & b_2 &= -i \frac{m_2^2 \cos \alpha}{v_S}, \\ b_{11} &= \frac{\sin \alpha}{4v v_S^2} (v_S (m_2^2 - m_1^2) \cos^3 \alpha + v m_2^2 \cos^2 \alpha \sin \alpha + v m_1^2 \sin^3 \alpha), \\ b_{22} &= \frac{\cos \alpha}{4v v_S^2} (v m_2^2 \cos^3 \alpha + v m_1^2 \cos \alpha \sin^2 \alpha + v_S (m_2^2 - m_1^2) \sin^3 \alpha), \\ b_{12} &= \frac{\cos \alpha \sin \alpha}{4v v_S^2} (2v m_2^2 \cos^2 \alpha + 2v m_1^2 \sin^2 \alpha - v_S (m_2^2 - m_1^2) \sin 3\alpha). \end{aligned} \quad (5.5)$$

The main contributions to these integrals come from the regions close to the poles of the propagators, that is where q^2 is close to the squared Higgs masses m_1^2 and m_2^2 , which are of the GeV order. In Direct Detection experiments, the target nucleus is almost at rest and hence the energy of the nucleons can be approximated by the Fermi energy, which is in the MeV order [66]. Thus, the approximation $p_2 \ll q$ is valid in these integrals and the denominators that contain p_2 can be expanded as follows [37, 67],

$$\frac{1}{(p_2 \pm q)^2 - m_q^2} = \frac{1}{q^2 \pm 2p_2 \cdot q} = \frac{1}{q^2} \mp \frac{2p_2 \cdot q}{q^4} + \mathcal{O}\left(\left(\frac{p_2 \cdot q}{q^2}\right)^2\right). \quad (5.6)$$

Using this approximation as well as the Dirac equation $\not{p}u(p) = m_q u(p)$ yields

$$\begin{aligned} i\mathcal{M}_{ij}^{\square} &= A_{ij} \bar{u}(p_2) \int \frac{d^4 q}{(2\pi)^4} \frac{1}{q^2 - m_i^2} \frac{1}{(p_1 - q)^2 - m_\chi^2} \frac{1}{q^2 - m_j^2} \left(\frac{4m_q}{q^2} + \frac{-4p_2 \cdot q}{q^4} \not{q} \right) u(p_2), \\ i\mathcal{M}_{ij}^{\triangle} &= B_{ij} \bar{u}(p_2) \int \frac{d^4 q}{(2\pi)^4} \frac{1}{q^2 - m_i^2} \frac{1}{q^2 - m_j^2} \left(\frac{1}{q^2} - \frac{2p_2 \cdot q}{q^4} \right) (2m_q + \not{q}) u(p_2). \end{aligned} \quad (5.7)$$

These amplitudes can be reduced to the Passarino–Veltmann integral basis by the standard techniques.

Note that this approximation is required for the fact that an exact calculation would not lead to results that could be matched to the effective Lagrangian in Eq. (3.24); specifically, without using the expansion (5.6), the external momenta of the DM particle and the quark

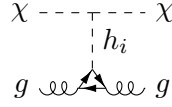


Figure 5.8: Interaction of a DM particle and a gluon via a Higgs boson mediator and a quark loop.

would appear as arguments of Passarino–Veltmann functions. Using the approximation, all expressions for the box and triangle diagrams become proportional to either $\bar{u}(p_2)u(p_2)$ or $(p_1 \cdot p_2)\bar{u}(p_2)\not{p}_1 u(p_2)$ and are otherwise momentum independent.

5.3 NLO Diagrams with External Gluons

The interaction of a DM particle χ with a gluon g is only feasible through a Higgs boson mediator and a quark loop. In the simplest case, the mediator Higgs boson can couple through a quark triangle to a gluon. This is shown in Fig. 5.8. When summed over $i = 1, 2$, this diagram is proportional to the squared momentum transfer t just as the tree-level amplitude in Eq. (5.1) and therefore vanishes in the limit of vanishing momentum transfer.

In [17], also the higher-order diagrams in Fig. 5.9 are taken into account. The coupling of a Higgs boson and a gluon through a quark triangle as in the first and second of these diagrams can be matched to the coupling of the Higgs boson to heavy quarks $Q = c, t, b$. This matching is presented in Sec. 5.3.1. However, by this matching only diagrams with electroweak corrections to the Higgs boson propagator and the (“upper”) DM–Higgs boson vertex can be taken into account; electroweak corrections to the (“lower”) quark–Higgs boson vertex would obviously interfere with the quark triangle, which makes a matching to heavy quarks non-trivial, since the loops do not factorize [37]. Thus, including these corrections to the quark triangle would require a full two-loop calculation, which is beyond the scope of this work. Then, for consistency, also the first and second diagram of the sum in Fig. 5.9 have not been taken into account for the results of this work. Taking into account only the propagator and “upper” vertex corrections also comes with the issue that the arbitrarily introduced field-strength renormalization factors of the Higgs boson fields do not cancel completely anymore, which they should as known from Fig. 4.5. Moreover, without taking into account the field-strength renormalization constants consistently, the KOSY scheme for the renormalization of the mixing angle α (see Sec. 4.4) would cause numerical instabilities for degenerate Higgs masses $m_2 \rightarrow m_1$ [60]. These effects will be further discussed in Chapter 6.

The third diagram in the sum of Fig. 5.9 represents the triangle and box diagrams with

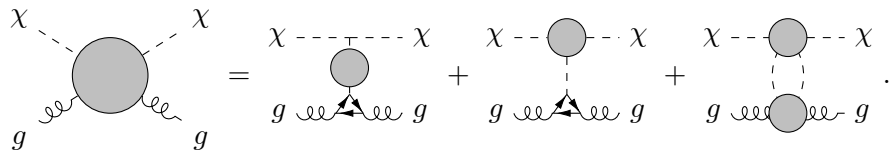


Figure 5.9: Possible higher-order electroweak corrections to DM–gluon scattering. They are given by propagator corrections, vertex corrections and a box diagrams.

external gluons. This two-loop diagram can be reduced to an effective one-loop diagram in the Fock–Schwinger gauge, as it will be derived in Sec. 5.3.2 (see this section also for the explicit meaning of the blobs in this diagram). It is of the same order of perturbation theory as the other diagrams in Fig. 5.9; its contribution to the cross section is negligible, as we will discuss in Chapter 6.

5.3.1 Vertex and Propagator Correction Diagrams with External Gluons

The propagator correction blobs for diagrams with external quarks in Fig. 5.2 and for diagrams with external gluons in Fig. 5.9 are identical. The same holds true for the vertex correction blobs to the (“upper”) DM–Higgs boson vertex. These diagrams with external quarks and external gluons only differ in the “lower” vertex, where the Higgs boson couples to a quark or via a quark triangle to a gluon. It turns out that the effective coupling of a Higgs boson to a gluon through a quark triangle can be matched to the coupling of a Higgs boson to a heavy quark $Q = c, b, t$ [68].

This matching relies on a phenomenon called *trace anomaly*. Classically, the trace of the energy–momentum tensor in QCD is given by [34]

$$\Theta^\mu{}_\mu = \sum_q m_q \bar{q}q, \quad (5.8)$$

where q is the quark field and m_q the corresponding quark mass. Upon including quantum corrections, however, this trace receives an additional contribution proportional to the β function and the γ_m function of renormalization group theory [38, 68],

$$\Theta^\mu{}_\mu = \sum_q m_q (1 - \gamma_{m_q}) \bar{q}q + \frac{\beta_n(\alpha_s)}{4\alpha_s} G_{\mu\nu}^a G_a^{\mu\nu}. \quad (5.9)$$

Here, α_s is the strong coupling constant and the index n of the β function indicates the number of quark flavors that are taken into account.

The nucleon matrix element of the trace of the energy–momentum tensor is equal to the mass of the nucleon [69],¹

$$m_n = \langle n | \Theta^\mu{}_\mu | n \rangle. \quad (5.10)$$

Under the assumption that approximately only the light quarks $q = u, d, s$ contribute significantly to the overall nucleon mass, using Eqs. (5.9) and (5.10) the nucleon mass can be written as

$$m_n \approx \sum_{q=u,d,s} \langle n | m_q (1 - \gamma_{m_q}) \bar{q}q | n \rangle + \frac{\beta_3(\alpha_s)}{4\alpha_s} \langle n | G_{\mu\nu}^a G_a^{\mu\nu} | n \rangle. \quad (5.11)$$

Consequently, the contribution of a heavy quark Q to the nucleon mass is approximately zero

¹ This neat result depends on the normalization being chosen as $\langle n | n \rangle = (2\pi)^3 \delta^{(3)}(\mathbf{0}) E / m_n$, where E is the total energy and m_n is the mass of the nucleon.

[68, 70], such that

$$m_n \approx \sum_{q=u,d,s,Q} \langle n|m_q(1 - \gamma_{m_q})\bar{q}q|n\rangle + \frac{\beta_4(\alpha_s)}{4\alpha_s} \langle n|G_{\mu\nu}^a G_a^{\mu\nu}|n\rangle \quad (5.12)$$

for any $Q = c, b, t$. Subtracting Eq. (5.11) from (5.12) yields

$$\begin{aligned} 0 &\approx \langle n|m_Q(1 - \gamma_{m_Q})\bar{Q}Q|n\rangle + \frac{\Delta\beta(\alpha_s)}{4\alpha_s} \langle n|G_{\mu\nu}^a G_a^{\mu\nu}|n\rangle \\ \Leftrightarrow \quad \langle n|m_Q\bar{Q}Q|n\rangle &\approx - \underbrace{\frac{\Delta\beta(\alpha_s)}{4\alpha_s(1 - \gamma_{m_Q})}}_{=\alpha_s/(12\pi)+\mathcal{O}(\alpha_s^2)} \langle n|G_{\mu\nu}^a G_a^{\mu\nu}|n\rangle, \end{aligned} \quad (5.13)$$

where $\Delta\beta \equiv \beta_4 - \beta_3 = \alpha_s^2/(3\pi)$.² It was also used that γ_m is of order $\mathcal{O}(\alpha_s)$.

Using this relation alongside with Eqs. (3.29) and (3.31), the contribution to the nucleon coupling α_n from the gluon term of the Lagrangian can be given as

$$\alpha_n \supset \langle n|G_{\mu\nu}^a G_a^{\mu\nu}|n\rangle \alpha_S^g = C_S^g \frac{2\alpha_s}{\pi} \langle n|G_{\mu\nu}^a G_a^{\mu\nu}|n\rangle \approx -24C_S^g \langle n|m_Q\bar{Q}Q|n\rangle. \quad (5.14)$$

If there was a term $C_S^Q m_Q \chi^2 \bar{Q}Q$ in the Lagrangian, its contribution to the nucleon coupling would be

$$\alpha_n \supset \langle n|\bar{Q}Q|n\rangle \alpha_S^Q = 2C_S^Q \langle n|m_Q\bar{Q}Q|n\rangle, \quad (5.15)$$

where Eqs. (3.28) and (3.30) were used. Thus, the gluon contribution can also be described by such a heavy quark term in the Lagrangian, where the Wilson coefficients need to be related by $2C_S^Q = -24C_S^g$. In practice this means that one can compute the Wilson coefficient C_S^Q from diagrams with external heavy quarks and thereby also find the value for the gluon Wilson coefficient as

$$C_S^g = -\frac{1}{12}C_S^Q, \quad (5.16)$$

without computing any diagram with external gluons explicitly. C_S^g then enters the cross section as described by Eq. (3.35).

5.3.2 Triangle and Box Diagrams with External Gluons

The third diagram in the sum in Fig. 5.9 represents the triangle and box diagrams with external gluons. More explicitly, it represents the diagrams in Fig. 5.10. All non-redundant combinations of h_i and h_j ($i, j = 1, 2$) have to be taken into account.

In principle, all quark flavors can appear in the quark loop in these diagrams. However, since all of the diagrams contain two quark–Higgs vertices, each of which is proportional to the quark mass, the contributions of all other quark flavors can be neglected in comparison to

² Note that $\Delta\beta = \beta_{n+1} - \beta_n = \alpha_s^2/(3\pi)$ for any n .

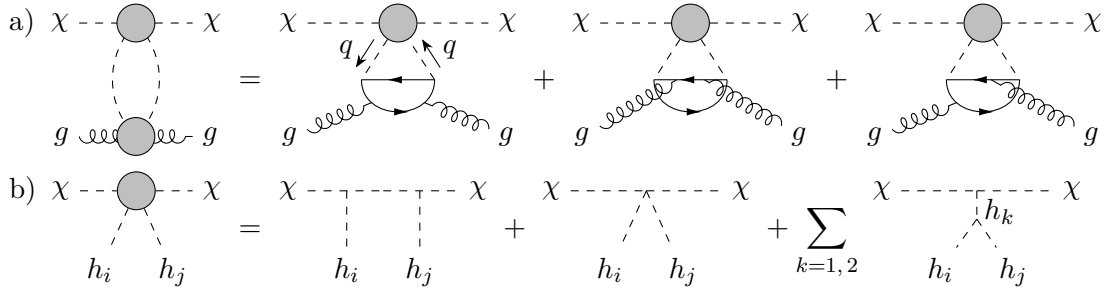


Figure 5.10: Triangle and box diagrams with external gluons. a) shows the meaning of the lower blob, whereas in b) the meaning of the upper blob is presented.

the top quark. Therefore, only the case of the top quark loop is considered, which will allow for significant simplifications due to approximations that are valid for large quark masses.

Following [37], in the first step the quark loop integral will be performed in the Fock–Schwinger gauge (see Sec. 5.3.2.1). After constructing the loop amplitude, where the gluon legs are described in terms of background field contributions to the full quark propagator (see Secs. 5.3.2.2–5.3.2.4), the loop integral is computed using Feynman parameters in Sec. 5.3.2.5. After arriving at this result, the approximation of a heavy quark mass will reduce the result of the loop integral – which is so far a function of the second loop momentum q – to a constant effective coupling between two gluons and two Higgs bosons. The sum of the diagrams in Fig 5.10a can then be given in terms of an effective coupling between two Higgs bosons and two gluons as shown in Fig. 5.11 In this way, the top quark that foremost contributes to these diagrams has been integrated out and the full two-loop computation has been simplified to two separate one-loop computations.

5.3.2.1 The Fock–Schwinger Gauge

The general Fock–Schwinger gauge condition on a gluon field $A_\mu^a(x)$ with Lorentz index μ and SU(3) index a is given by [71]³

$$(x^\mu - x_0^\mu) A_\mu^a(x) = 0, \tag{5.17}$$

where x_0^μ serves as an arbitrary gauge parameter. In what follows, we will choose $x_0^\mu = 0$ for simplicity.

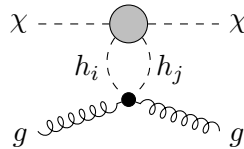


Figure 5.11: Box diagram with effective gluon Higgs coupling.

³ This whole section follows [71] quite tightly.

The Fock–Schwinger gauge comes with the useful feature that the gluon field $A_\mu^a(x)$ can be expressed uniquely in terms of the field-strength tensor $G_{\mu\nu}^a(x)$. In order to derive this relation explicitly, one may start off by differentiating Eq. (5.17),

$$0 = \partial_\mu (x^\nu A_\nu^a(x)) = A_\mu^a(x) + x^\nu \partial_\mu A_\nu^a(x) = A_\mu^a(x) + x^\nu (G_{\mu\nu}^a(x) + \partial_\nu A_\mu(x)). \quad (5.18)$$

Note that the last step in Eq. (5.18) is valid because in the Fock–Schwinger gauge the third term of the field strength tensor

$$G_{\mu\nu}^a = \partial_\mu A_\nu^a - \partial_\nu A_\mu^a + gf^{abc} A_\mu^b A_\nu^c \quad (5.19)$$

vanishes upon multiplication with x^ν . Substituting $x \rightarrow \alpha x$ yields

$$0 = A_\mu^a(\alpha x) + x^\nu \partial_\nu A_\mu^a(\alpha x) + \alpha x^\nu G_{\mu\nu}^a(\alpha x) = \frac{d}{d\alpha} \alpha A_\mu^a(\alpha x) + \alpha x^\nu G_{\mu\nu}^a(\alpha x). \quad (5.20)$$

Finally, integrating both sides from $\alpha = 0$ to $\alpha = 1$ leads to the sought-after relation

$$A_\mu^a(x) = -x^\nu \int_0^1 d\alpha \alpha G_{\mu\nu}^a(\alpha x). \quad (5.21)$$

It is possible to perform the integral over α explicitly by writing $G_{\mu\nu}^a(\alpha x)$ as a Taylor series around $x = 0$,⁴

$$\begin{aligned} A_\mu^a(x) &= -x^\nu \int_0^1 d\alpha \alpha \sum_{n=0}^{\infty} \frac{1}{n!} \left(\prod_{i=1}^n \frac{\partial}{\partial x^{\sigma_i}} \right) G_{\mu\nu}^a(\alpha x) \Big|_{x=0} (\prod_{i=1}^n x^{\sigma_i}) \\ &= -x^\nu \int_0^1 d\alpha \alpha \sum_{n=0}^{\infty} \frac{\alpha^n}{n!} \left(\prod_{i=1}^n \frac{\partial}{\partial (\alpha x)^{\sigma_i}} \right) G_{\mu\nu}^a(\alpha x) \Big|_{x=0} (\prod_{i=1}^n x^{\sigma_i}) \\ &= -x^\nu \sum_{n=0}^{\infty} \frac{1}{n!} \int_0^1 d\alpha \alpha^{n+1} \left(\prod_{i=1}^n \frac{\partial}{\partial x^{\sigma_i}} \right) G_{\mu\nu}^a(x) \Big|_{x=0} (\prod_{i=1}^n x^{\sigma_i}) \\ &= -x^\nu \sum_{n=0}^{\infty} \frac{1}{n!} \frac{1}{n+2} (\prod_{i=1}^n \partial_{\sigma_i}) G_{\mu\nu}^a(x) \Big|_{x=0} (\prod_{i=1}^n x^{\sigma_i}). \end{aligned} \quad (5.22)$$

5.3.2.2 The Idea of the Background Field Method

Before moving on with computing the quark loop, let us quickly introduce the basic ideas of the background field method. A more profound introduction is given in [35].

Pictorially, the QED Lagrangian can be given as

$$\mathcal{L} = \text{wavy line} + \text{arrow line} + \text{wavy line with two arrows}. \quad (5.23)$$

If one is interested in processes with external photons only in which case the electrons solely appear as internal loop particles, it is possible to compute an effective QED Lagrangian

⁴ In Eq. (5.22), the convention $\prod_{i=1}^0(\text{anything}) = 1$ is used.

for these processes that is of the form [35]⁵

$$\begin{aligned} \mathcal{L}_{\text{eff}} &= \text{wavy line} + \text{loop with wavy line} + \text{loop with wavy line} + \text{loop with wavy line} + \dots \quad (5.24) \\ &= -\frac{1}{4} F_{\mu\nu}(x) F^{\mu\nu}(x) + a^\mu A_\mu(x) + b^{\mu\nu} A_\mu(x) A_\nu(x) + c^{\mu\nu\sigma} A_\mu(x) A_\nu(x) A_\sigma(x) + \dots \end{aligned}$$

This effective Lagrangian only depends on photon fields $A_\mu(x)$, whereas the fermion fields are *integrated out*. That is, their effective contribution through the loops is absorbed into the coefficients a^μ , $b^{\mu\nu}$, $c^{\mu\nu\sigma}$ etc.

For example, the prefactor $b^{\mu\nu}$ is computed by⁶

$$\begin{aligned} b^{\mu\nu} A_\mu(0) A_\nu(0) &= \text{loop with wavy lines and crosses} \quad (5.25) \\ &= (ie)^2 \int d^4z d^4z' \text{Tr} S^0(z' - z) \mathcal{A}(z) S^0(z - z') \mathcal{A}(z'), \end{aligned}$$

where $S^0(x - y)$ is the fermion Feynman propagator in position space. Here, the propagator with a cross marks the corresponding field as a *background field* (not to be confused with a counterterm) that comes with the Feynman rule [34]

$$\text{crossed wavy line} = ie \int d^4z \mathcal{A}(z) \quad (5.26)$$

in position space.

In the presence of this background field, the full fermion propagator, describing a fermion travelling from x to y , is given by [34]

$$\begin{aligned} S(x, y) &= x \longrightarrow y + x \xrightarrow{\text{cross}} y + x \xrightarrow{\text{cross}} \text{cross} y + \dots \\ &= S^0(x - y) + ie \int d^4z S^0(x - z) \mathcal{A}(z) S^0(z - y) \quad (5.27) \\ &\quad + (ie)^2 \int d^4z d^4z' S^0(x - z) \mathcal{A}(z) S^0(z - z') \mathcal{A}(z') S^0(z' - y) + \dots \end{aligned}$$

⁵ In principle, \mathcal{L}_{eff} also includes a fermion loop with no external photons. This diagram is equivalent to a constant and constant terms in Lagrangians have no effect on the computation of scattering amplitudes.

⁶ Note that the integral over $d^4z d^4z'$ needs to be proportional to $A_\mu(0)A_\nu(0)$, since there is nothing but A_μ to carry the Lorentz indices and there is no length scale that could appear as an argument of A_μ . Still, in the effective Lagrangian (5.24), the fields have all the same spatial argument x .

5.3.2.3 The Full Quark Propagator in a Gluon Background Field

The object of interest is a quark loop with two Higgs bosons and two gluons attached to it. Ignoring the gluons for the moment, the quark loop with two Higgs bosons only is given by Feynman rules as

$$\begin{array}{c} h_i \\ \text{---} \circlearrowleft \text{---} \\ x \quad y \\ \text{---} \circlearrowright \text{---} \\ h_j \\ \text{---} \text{---} \\ y_0 \end{array} = - \int d^4x d^4y H_i^0(x_0-x) \text{Tr} a_i S^0(x-y) a_j S^0(y-x) H_j^0(y-y_0) \quad (5.28)$$

in position space. Here, H_i^0 is the Feynman propagator of the Higgs boson field h_i , S^0 is the Feynman propagator of the quark and a_i is the coupling factor of the $h_i q \bar{q}$ coupling.⁷ In position space, this amplitude cannot readily be given in its amputated form, as the external propagator depends on integration variables. After performing a Fourier transformation on H_i^0 and choosing the coordinate system such that $y = 0$ it is found that the *amputated* amplitude (with the Higgs propagators dropped) reads [71]

$$i\hat{\Pi}_{ij}(q) \equiv h_i \text{---} \overset{q}{\circlearrowleft} \text{---} h_j = -a_i a_j \int d^4x e^{iq \cdot x} \text{Tr} S^0(x-0) S^0(0-x). \quad (5.30)$$

To include (all possible numbers of) gluons that are attached to the loop in addition to the Higgs boson simply replace $S^0(x-y)$ by $S(x,y)$ from Eq. (5.27). This will change $\hat{\Pi}_{ij}(q)$ to, say, $\Pi_{ij}(q)$. Defining the Fourier transformed propagators

$$S(p) \equiv \int d^4x e^{ip \cdot x} S(x, 0), \quad \tilde{S}(p) \equiv \int d^4x e^{-ip \cdot x} S(0, x), \quad (5.31)$$

and using the inverse versions of these relations to turn $S(x,y)$ into momentum space yields

$$i\Pi_{ij}(q) = -a_i a_j \int \frac{d^4p}{(2\pi)^4} \text{Tr} S(p) \tilde{S}(p-q). \quad (5.32)$$

Plugging the expansion (5.27) into Eq. (5.31) (and replacing $e \rightarrow g_s$, since we are now

⁷ For explicitness: In the DCxSM, the (Yukawa) couplings a_i of the Higgs mass eigenstates h_i with a quark q are given by

$$a_1 = -i \frac{m_q \cos \alpha}{v}, \quad a_2 = i \frac{m_q \sin \alpha}{v}, \quad (5.29)$$

where m_q is the quark mass, α the Higgs mass mixing angle and v the VEV of the Higgs field H .

concerned about gluons instead of photons) yields⁸

$$\begin{aligned}
S(p) &= S^0(p) + ig_s \int \frac{d^4 k}{(2\pi i)^4} S^0(p) \mathcal{A}(k) S^0(p-k) \\
&\quad + (ig_s)^2 \int \frac{d^4 k_1}{(2\pi)^4} \frac{d^4 k_2}{(2\pi)^4} S^0(p) \mathcal{A}(k_1) S^0(p-k_1) \mathcal{A}(k_2) S^0(p-k_1-k_2), \\
\tilde{S}(p) &= S^0(p) + ig_s \int \frac{d^4 k}{(2\pi i)^4} S^0(p+k) \mathcal{A}(k) S^0(p) \\
&\quad + (ig_s)^2 \int \frac{d^4 k_1}{(2\pi)^4} \frac{d^4 k_2}{(2\pi)^4} S^0(p+k_1+k_2) \mathcal{A}(k_2) S^0(p+k_1) \mathcal{A}(k_2) S^0(p),
\end{aligned} \tag{5.34}$$

where $S^0(p) = i/(\not{p} - m)$. In these expressions also the Fourier transform of the gluon field $A_\mu(x) = t^a A_\mu^a(x)$ appears, with t^a being the generators of SU(3). Using the expansion (5.22), it can be given as

$$\begin{aligned}
A_\mu(k) &= \int d^4 x e^{ik \cdot x} A_\mu(x) \\
&= - \sum_{n=0}^{\infty} \frac{1}{n!} \frac{1}{n+2} (\prod_{i=1}^n \partial_{\sigma_i}) G_{\mu\nu}(x)|_{x=0} \int d^4 x e^{ik \cdot x} x^\nu (\prod_{i=1}^n x^{\sigma_i}) \\
&= - \sum_{n=0}^{\infty} \frac{1}{n!} \frac{1}{n+2} (\prod_{i=1}^n \partial_{\sigma_i}) G_{\mu\nu}(x)|_{x=0} (-i) \frac{\partial}{\partial k_\nu} \left((-i)^n \prod_{i=1}^n \frac{\partial}{\partial k_{\sigma_i}} \right) \underbrace{\int d^4 x e^{ik \cdot x}}_{=(2\pi)^4 \delta(k)},
\end{aligned} \tag{5.35}$$

where $G_{\mu\nu}(x) = t^a G_{\mu\nu}^a(x)$.

5.3.2.4 Constructing the Loop Amplitude

The overall structure of both propagators $S(p)$ and $\tilde{S}(p)$ from Eq. (5.34) reads $S^0 + S^0 A S^0 + S^0 A S^0 A S^0 + \dots$. In the loop amplitude (5.32), the combination $S(p) \tilde{S}(p-q)$ appears, which then is of the structure

$$\begin{aligned}
S\tilde{S} &= (S^0 + S^0 A S^0 + S^0 A S^0 A S^0 + \dots)^2 \\
&= S^0 S^0 A S^0 A S^0 + S^0 A S^0 S^0 A S^0 + S^0 A S^0 A S^0 S^0 + (\text{irrelevant}).
\end{aligned} \tag{5.36}$$

⁸ For example, for the derivation of the second term of $S(p)$ consider

$$\begin{aligned}
&\int d^4 x e^{-ip \cdot x} \int d^4 z a(x-z) b(z) c(z) \\
&= \int d^4 x d^4 z e^{ip \cdot x} \int \frac{d^4 k_1}{(2\pi)^4} \frac{d^4 k_2}{(2\pi)^4} \frac{d^4 k_3}{(2\pi)^4} e^{-ik_1 \cdot x} e^{-i(k_1 - k_2 + k_3) \cdot z} a(k_1) b(k_2) c(k_3) \\
&= \int d^4 x \int \frac{d^4 k_2}{(2\pi)^4} \frac{d^4 k_3}{(2\pi)^4} e^{-i(k_2 + k_3 - p) \cdot x} a(k_2 + k_3) b(k_2) c(k_3) \\
&= \int \frac{d^4 k}{(2\pi)^4} a(p) b(k) c(p-k).
\end{aligned} \tag{5.33}$$

The other terms are derived analogously.

Since the object of interest in this work is a loop with exactly two external gluons, all terms with a number of gluon fields A other than two are irrelevant. Filling in the details, the amplitude reads

$$\begin{aligned}
i\Pi_{ij}(q) = & -(ig_s)^2 a_i a_j \int \frac{d^4 p}{(2\pi)^4} \frac{d^4 k_1}{(2\pi)^4} \frac{d^4 k_2}{(2\pi)^4} \quad (5.37) \\
& \text{Tr} (S^0(p) S^0(p - q + k_1 + k_2) \not{A}(k_2) S^0(p - q + k_1) \not{A}(k_1) S^0(p - q) \\
& + S^0(p) \not{A}(k_1) S^0(p - k_2) S^0(p - q + k_1) \not{A}(k_2) S^0(p - q) \\
& + S^0(p) \not{A}(k_1) S^0(p - k_1) \not{A}(k_2) S^0(p - k_1 - k_2) S^0(p - q)) \\
& + (\text{irrelevant}) .
\end{aligned}$$

Now, the expansion (5.35) can be plugged in. Only the first term $n = 0$ is required. Using $G_{\mu\nu}(0) = G_{\mu\nu}^a(0)t^a$ and $\text{Tr} t^a t^b = \delta^{ab}/2$, and dropping the irrelevant terms, yields⁹

$$\begin{aligned}
i\Pi_{ij}(q) = & -\frac{i^2 (ig_s)^2}{8} a_i a_j G_{\mu\nu}^a(0) G_{\rho\sigma}^a(0) \int \frac{d^4 p}{(2\pi)^4} \frac{\partial}{\partial k_{1\nu}} \frac{\partial}{\partial k_{2\sigma}} \quad (5.39) \\
& \text{Tr} (S^0(p) S^0(p - q + k_1 + k_2) \gamma^\mu S^0(p - q + k_2) \gamma^\rho S^0(p - q) \\
& + S^0(p) \gamma^\mu S^0(p - k_1) S^0(p - q + k_2) \gamma^\rho S^0(p - q) \\
& + S^0(p) \gamma^\mu S^0(p - k_1) \gamma^\rho S^0(p - k_1 - k_2) S^0(p - q)) \Big|_{k_1, k_2=0} .
\end{aligned}$$

In the first of the three terms, the names of the momenta $k_1 \leftrightarrow k_2$ have been swapped to enable a compact notation.

5.3.2.5 Computing the Loop Integral

One may replace [37]

$$G_{\mu\nu}^a G_{\rho\sigma}^a \rightarrow \frac{1}{12} G_{\kappa\eta}^a G^{a\kappa\eta} (g_{\mu\rho} g_{\nu\sigma} - g_{\mu\sigma} g_{\nu\rho}) \quad (5.40)$$

if one is only interested in spin-independent interactions. Furthermore, one can now plug in the explicit form of the Feynman propagators S^0 , perform the derivatives with respect to k_1 and k_2 and compute the Dirac trace. Finally, by a shift of the integration variable $p \rightarrow -p + q$ in the first term in the trace of Eq. (5.39), it can be shown that the first and the

⁹ Also the δ function identity

$$\int d^4 x f(x) \partial_\mu \delta(x) = -\partial_\mu f(x)|_{x=0}, \quad (5.38)$$

which is easily derived using integration by parts, is used in this step.

last term contribute equally. Specifically, the result is

$$i\Pi_{ij}(q) = \frac{i^2(i g_s)^2}{2} a_i a_j G_{\mu\nu}^a(0) G^{a\mu\nu}(0) \quad (5.41)$$

$$\cdot \int \frac{d^4 p}{(2\pi)^4} \left(2 \cdot \frac{2m^2(2p^2 - p \cdot q)}{(p^2 - m^2)^4((p - q)^2 - m^2)} + \frac{2m^2 + p \cdot (p - q)}{(p^2 - m^2)^2((p - q)^2 - m^2)^2} \right),$$

where m is the mass of the quark in the loop.

This loop integral can now be evaluated by the usual procedure. The identity [34]

$$\prod_{i=1}^n \frac{1}{A_i^{a_i}} = \frac{\Gamma(\sum_{i=1}^n a_i)}{\prod_{i=1}^n \Gamma(a_i)} \int_0^1 (\prod_{i=1}^n dx_i) \frac{\delta(1 - \sum_{i=1}^n x_i) \prod_{i=1}^n x_i^{a_i - 1}}{(\sum_{i=1}^n A_i x_i)^{\sum_{i=1}^n a_i}} \quad (5.42)$$

is used to introduce Feynman parameters x_i . By a shift $p \rightarrow p + qx$, the denominators can then be brought into the form $(l^2 - \Delta)^n$, where

$$\Delta \equiv m^2 - q^2 x(1 - x), \quad (5.43)$$

such that the integral formulas in [34] can be applied:

$$i\Pi_{ij}(q) = 3g_s^2 a_i a_j G_{\mu\nu}^a(0) G^{a\mu\nu}(0) \int_0^1 dx \int \frac{d^4 p}{(2\pi)^4} \left(\frac{8}{3} m^2 (1 - x)^3 \frac{2p^2 - p \cdot q}{((p - qx)^2 - \Delta)^5} \right. \\ \left. + x(1 - x) \frac{2m^2 + p \cdot (p - q)}{((p - qx)^2 - \Delta)^4} \right) \quad (5.44)$$

$$= \frac{ig_s^2}{96\pi^2} a_i a_j G_{\mu\nu}^a(0) G^{a\mu\nu}(0) \int_0^1 dx \frac{4m^2(1 - x)^3(2m^2 - q^2x) + 3q^2x^2(1 - x)^2\Delta}{\Delta^3}.$$

It was used that $\int d^4 p p^\mu f(p^2) = 0$ for any function f by symmetry.

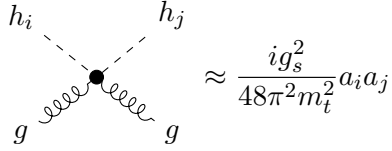
Recall that m is the quark mass and that only the top quark is considered, hence $m = m_t$. q is the loop momentum of the second loop of the diagrams in Fig. 5.10a as well as the momentum of the Higgs propagators. Thus, as in Sec. 5.2.2, the main contribution to the integral of the second loop comes from regions where q^2 is close to the squared Higgs masses m_1^2 and m_2^2 . Assuming $m_1 \ll m_t$ and $m_2 \ll m_t$ therefore yields $q^2 \ll m_t^2$, which makes the q dependence drop out completely,

$$i\Pi_{ij} \approx \frac{ig_s^2}{48\pi^2 m_t^2} a_i a_j G_{\mu\nu}^a(0) G^{a\mu\nu}(0). \quad (5.45)$$

The validity of this approximation is discussed and compared to the full two-loop result in [37]; for large Higgs masses, the approximation over-estimates the full two-loop result for the contribution to the Wilson C_S^g . We will discuss the contribution of these box diagrams with external gluons to the cross section in Chapter 6.

According to Eqs. (5.24) and (5.25), this expression for $i\Pi_{ij}$ can – after dropping $G_{\mu\nu}^a(0)G^{a\mu\nu}(0)$ – be plugged in as a vertex factor for the effective gluon–gluon–Higgs–Higgs vertex in Fig. 5.11.

In other words, the Feynman rule



$$\begin{array}{c} h_i \quad h_j \\ \diagdown \quad \diagup \\ \bullet \\ \diagup \quad \diagdown \\ g \quad g \end{array} \approx \frac{i g_s^2}{48 \pi^2 m_t^2} a_i a_j \quad (5.46)$$

can be adopted. This Feynman rule corresponds to a term

$$\mathcal{L} \supset \frac{1}{2} \frac{g_s^2}{48 \pi^2 m_t^2} a_i a_j h_i h_j G_{\mu\nu}^a G^{a\mu\nu} \quad (5.47)$$

in the effective Lagrangian [37].

Using this Feynman rule, the box diagrams with external gluons in Fig. 5.10 are thereby reduced to a 1-loop diagram that can be computed by the standard procedure.

5.4 Matching the Amplitude to the Effective Operators

Regarding their dependence on external momenta, the mathematical expressions of all the diagrams with external quarks have only two types of terms that contribute to spin-independent scattering: Terms proportional to $\bar{u}(p_2) u(p_2)$ (and otherwise independent of momenta) and terms proportional to $(p_1 \cdot p_2) \not{p}_1 \bar{u}(p_2) u(p_2)$, where p_1 is the DM four-momentum and p_2 the quark four-momentum. Thereby, the spin-independent part of the expression of any diagram with external quarks that was considered here can be brought into the form

$$i\mathcal{M} = i \left(A \bar{u}(p_2) u(p_2) + B (p_1 \cdot p_2) \bar{u}(p_2) \not{p}_1 u(p_2) \right) \quad (5.48)$$

with some momentum-independent coefficients A and B .

The effective Lagrangian that would produce such an amplitude reads

$$\mathcal{L}_{\text{eff}} = \frac{1}{2} A \chi^2 \bar{q} q + \frac{1}{2} B (\chi i \partial^\mu i \partial^\nu \chi) (\bar{q} i \partial_\mu \gamma_\nu q). \quad (5.49)$$

Note that it immediately follows from the definition of $\mathcal{O}_{\mu\nu}^q$ in Eq. (3.27) that [37]

$$\bar{q} i \partial_\mu \gamma_\nu q = \mathcal{O}_{\mu\nu}^q + i \bar{q} \left(\frac{\partial_\mu \gamma_\nu - \partial_\nu \gamma_\mu}{2} + \frac{1}{4} g_{\mu\nu} \not{\partial} \right) q. \quad (5.50)$$

Plugging this expression into Eq. (5.49) yields

$$\mathcal{L}_{\text{eff}} = \left(\frac{1}{2m_q} A + \frac{1}{8} m_\chi^2 B \right) m_q \chi^2 \bar{q} q + \frac{1}{2} B (\chi i \partial^\mu i \partial^\nu \chi) \mathcal{O}_{\mu\nu}^q. \quad (5.51)$$

Note that $\partial_\mu \gamma_\nu - \partial_\nu \gamma_\mu$ is antisymmetric in μ and ν whereas $\chi i \partial^\mu i \partial^\nu \chi$ is symmetric. Hence, this term does not contribute. Furthermore, the Dirac equation $\not{\partial} q = m_q q$ was employed.

By comparing this expression with the definition of the Wilson coefficients in Eq. (3.24),

the Wilson coefficients can be related to the coefficients A and B as follows:

$$C_S^q = \frac{1}{2m_q}A + \frac{m_\chi^2}{8}B, \quad (5.52)$$

$$C_T^q = \frac{m_\chi^2}{2}B. \quad (5.53)$$

By the procedure presented in Sec. 5.3.2, all triangle and box diagrams with external gluons are proportional to $G_{\mu\nu}^a G^{a\mu\nu}$ and independent of momenta. Thereby, they can be matched directly to the gluon term of Eq. (3.26) in the effective Lagrangian (3.24) in order to determine the Wilson coefficient C_S^g .

CHAPTER 6

Numerical Analysis

After the analytical calculation of the cross section according to Eq. (3.35), numerical results are obtained by fixing the values of all input parameters. The values of the SM parameters used in this work are given in Sec. 6.1.

There are two distinct types of numerical analyses performed in this chapter. The first one is based on a parameter scan, which produces parameter points that obey current theoretical and experimental constraints. In Sec. 6.2, this analysis is described and its results are presented.

In Sec. 6.3, an individual valid parameter point is selected and its behavior upon variation of different parameters is examined.

Note that the approach for computing the cross section of Direct Detection in this work takes into account all the diagrams of Fig. 5.2, but only the last diagram of Fig. 5.9. For a detailed discussion about the choice of diagrams and the applied approximations see Chapter 5 as well as Sec. 6.3.

6.1 Numerical Values of the Parameters

For the SM parameters we take the following values [11, 72],

$$\begin{aligned} m_u &= 0.19 \text{ GeV}, & m_c &= 1.4 \text{ GeV}, & m_t &= 172.5 \text{ GeV}, \\ m_d &= 0.19 \text{ GeV}, & m_s &= 0.19 \text{ GeV}, & m_b &= 4.75 \text{ GeV}, \\ m_e &= 0.511 \text{ MeV}, & m_\mu &= 105.658 \text{ MeV}, & m_\tau &= 1.777 \text{ GeV}, \\ m_W &= 80.398 \text{ GeV}, & v &= 246 \text{ GeV}, \\ m_Z &= 91.188 \text{ GeV}. \end{aligned} \tag{6.1}$$

Note that thereby also the weak coupling and the Weinberg angle are fixed as

$$g = 2m_W/v = 0.653, \quad \sin \theta_W = m_W/m_Z = 0.472. \tag{6.2}$$

Recall that m_1 and m_2 are the masses of the lighter and heavier Higgs boson, respectively. In this chapter, we denote them as m_h for the mass of the SM-like Higgs boson and as m_ϕ for the mass of the non-SM-like Higgs boson. For the SM-like Higgs mass the value

$$m_h = 125.09 \text{ GeV} \tag{6.3}$$

is used [19].

Furthermore, the computation of the cross section according to Eq. (3.35) requires numerical values for the mass of a nucleon as well as for the form factors and second moments. The

analysis of the subsequent sections is done for the proton p , i. e. it holds

$$\sigma \equiv \sigma_p, \quad (6.4)$$

where σ_p is given by Eq. (3.35). The proton mass is taken to be [11]

$$m_p = 0.938 \text{ GeV}. \quad (6.5)$$

The values for the form factors f_q^n and f_g^n as well as for the second moments $q^n(2)$ and $\bar{q}^n(2)$ are taken from [37],

$$\begin{aligned} f_u^p &= 0.01513, & f_d^p &= 0.0191, & f_s^p &= 0.0447, \\ f_g^p &= 0.92107, & & & & \\ w^p(2) &= 0.22, & c^p(2) &= 0.019, & & \\ \bar{w}^p(2) &= 0.034, & \bar{c}^p(2) &= 0.019, & & \\ d^p(2) &= 0.11, & s^p(2) &= 0.026, & b^p(2) &= 0.012, \\ \bar{d}^p(2) &= 0.036, & \bar{s}^p(2) &= 0.026, & \bar{b}^p(2) &= 0.012. \end{aligned} \quad (6.6)$$

If not stated otherwise, all results are given in the Feynman gauge $\xi = 1$, where ξ is the gauge parameter of all gauge bosons. The gauge dependence will be examined in Sec. 6.3.

6.2 Parameter Scan

Having fixed all SM parameters according to Sec. 6.1, the values for the remaining four parameters given in Eq. (2.18) are produced during a parameter scan, which is automatized by the code SCANNERS-2 [73–76]. The scan ranges were chosen as follows,

$$\begin{aligned} m_\phi &\in [30 \text{ GeV}, 1000 \text{ GeV}], \\ m_\chi &\in [30 \text{ GeV}, 1000 \text{ GeV}], \\ v_S &\in [1 \text{ GeV}, 1000 \text{ GeV}], \\ \alpha &\in [-\pi/2, \pi/2]. \end{aligned} \quad (6.7)$$

The parameter scan of SCANNERS-2 takes into account current bounds for the non-SM-like Higgs boson from LEP, Tevatron and the LHC as well as constraints on the DM candidate, using interfaces to HIGGSBOUNDS-5 [77–79], HIGGSIGNALS-2 [80] and MICROMEGAS [51]. In addition, MICROMEGAS computes the relic density, as introduced in Sec. 3.6, for every parameter point.

In Fig. 6.1, the parameter points of the scan are added to the plot from Fig. 3.3, which shows the limits of several liquid xenon based Direct Detection experiments as well as the neutrino floor. Note that the *effective* cross section, as defined in Eq. (3.39), is plotted. There are parameter points above the neutrino floor (which is plotted in gray), corresponding to a wide range of mass values for the color-coded non-SM Higgs mass m_ϕ . The majority of them lies within a relatively narrow DM mass range of about $m_h/2 < m_\chi < 80 \text{ GeV}$. We found only points below the prospective XENON10T limit, but some lie above the prospective limit of the upcoming DARWIN experiment [81].

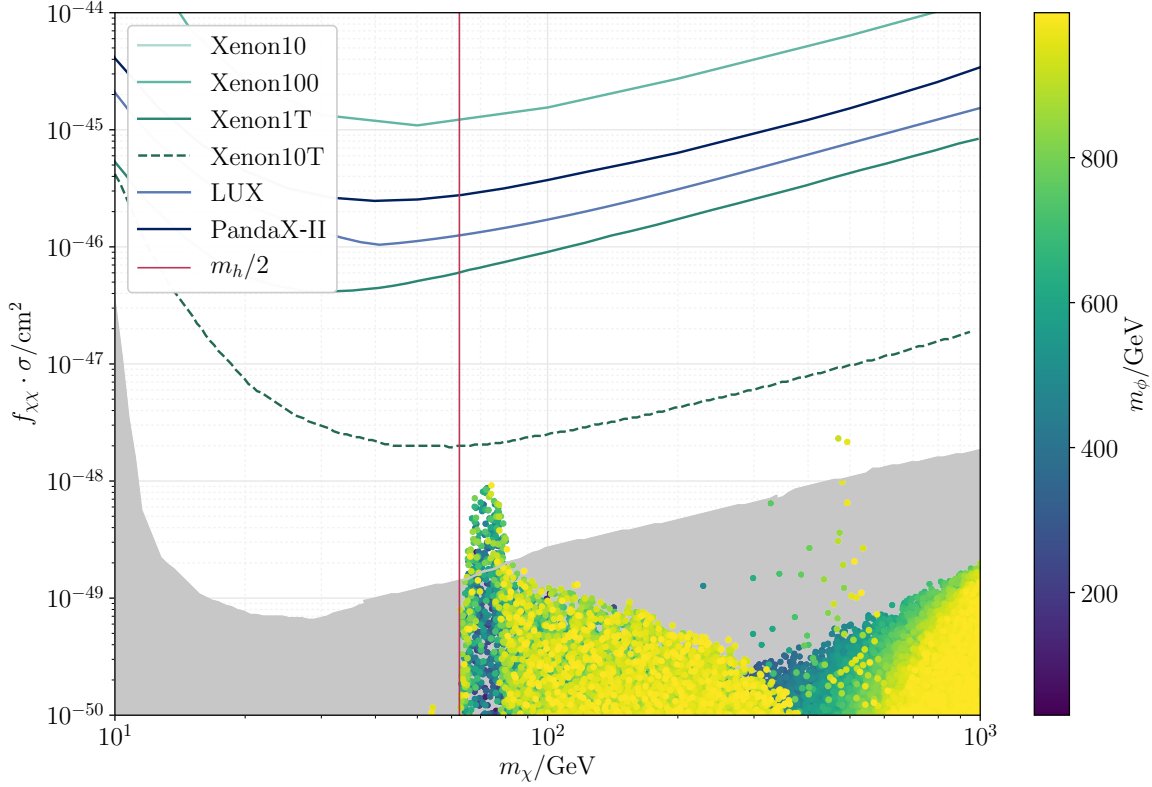


Figure 6.1: This plot shows the parameter sample together with the limits of liquid xenon based experiments from Fig. 3.3. The corresponding values of the effective spin-independent cross section $f_{\chi\chi} \cdot \sigma$ (see Sec. 3.6) are plotted against the DM mass m_χ . The color of the parameter points illustrates the mass of the non-SM-like Higgs boson m_ϕ . The neutrino floor is plotted in gray. The data for the limits and the neutrino floor was taken from [40–46], using the tool [47].

In Fig. 6.2, the cross section of all parameter points is plotted against the four non-SM parameters of the DCxSM. The plot in Fig. 6.2a is similar to Fig. 6.1, but with the cross section σ instead of the effective cross section $f_{\chi\chi} \cdot \sigma$ and with the axis bounds chosen in a way that all generated points are shown. For higher cross sections of about 10^{-49} cm^2 there is an edge at $m_\chi = m_h/2$. Note that the Higgs boson can decay into two DM particles if $m_\chi < m_h/2$. The Higgs to invisible searches at the LHC impose a constraint on the corresponding coupling of the DM–Higgs vertex. Since σ is proportional to this coupling, these constraints can be translated to constraints on σ , which forbids parameter points with $m_\chi < m_h/2$ for cross sections of a certain value (of about 10^{-50} cm^2 according to Fig. 6.2a) and above. For lower cross sections, DM masses of about 55 GeV and below are strongly constrained, presumably by astronomical observations. Moreover, from the color coding of Fig. 6.2a one can infer an anticorrelation between the cross section σ and the non-SM-like VEV v_S .

In Fig. 6.2b, only the parameter points that lie above the neutrino floor in Fig. 6.1 are plotted in color. By comparing the Figs. 6.2a and b with Fig. 6.1 it is obvious that it considerably depends on the value of the relic density factor $f_{\chi\chi}$ which points lie above the

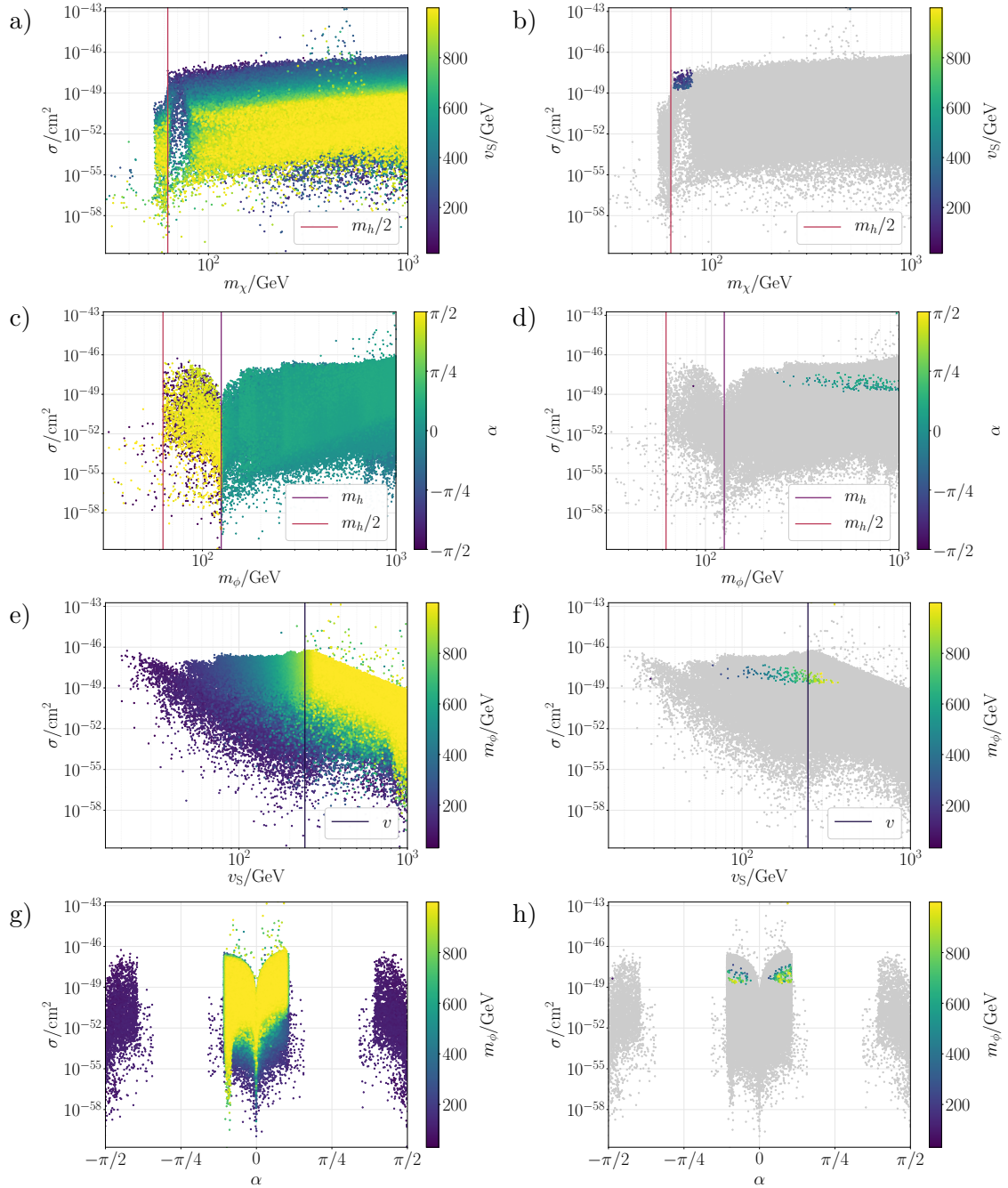


Figure 6.2: The cross section plotted against m_χ (a, b), m_ϕ (c, d), v_S (e, f) and α (g, h). On the left-hand side, all about 260 000 parameter points of the parameter scan fulfilling the theoretical and experimental constraints are plotted; the color illustrates the size of an additional parameter. On the right-hand side, only the parameter points that appear above the neutrino floor in Fig. 6.1 are plotted in color and all remaining parameter points in gray.

neutrino floor and which ones do not.

In Fig. 6.2c, the parameter points are plotted against the mass of the non-SM-like Higgs boson m_ϕ . For $m_\phi < m_h/2$, there are only isolated points since the decay of a SM-like Higgs boson into two non-SM-like Higgs bosons is strongly constrained by collider experiments. For $m_\phi < m_h$, only points with $\alpha \approx \pm\pi/2$ are found: The inverted mass hierarchy with additional light neutral Higgs bosons is only possible with singlet-like light Higgs bosons. Furthermore, there is a dip at $m_\phi = m_h$. It is already apparent in the tree level amplitude in Eq. (5.1), which is proportional to $m_h^2 - m_\phi^2$ (for finite t). This dip is also observed in the Vector Dark Matter Model [39].

In Fig. 6.2d, i. e. after dropping all points below the neutrino floor, there is a single parameter point left over for $m_\phi < m_h$, while most remaining points correspond to a wide span of rather large masses m_ϕ .

The behavior of the parameter points w. r. t. v_S is examined in Fig. 6.2e. As it can already be seen in Fig. 6.2a, the large cross sections are strongly constrained for large values of v_S . It can also be inferred from Fig. 6.2c that there is a correlation between m_ϕ and v_S .

Finally, in Fig. 6.2g, the parameter points are plotted against the Higgs mixing angle α . It follows from Eq. (2.12) and (2.13) that the mixing of the gauge eigenstates ϕ_H and ϕ_S is maximal for $\alpha = \pm\pi/4$, where basically no points appear in Fig. 6.2d. It was shown in [76] that large singlet admixtures to the SM-like Higgs boson are disfavored by the experimental constraints, which is also applicable to the DCxSM. For $\alpha = \pm\pi/2$, the gauge eigenstate of the SM-like Higgs boson ϕ_H is associated with the heavier Higgs mass m_2 , such that m_ϕ must be smaller than m_h . Therefore, the points in this region show up in a dark hue. At $\alpha = 0$ the mixing of the Higgs gauge eigenstates vanishes and so does the mixing of the SM-like Higgs doublet H and the non-SM-like singlet S (see Eq. (2.1) and note that $\lambda_{HS}|_{\alpha=0} = 0$ from Eq. (2.16)). Therefore, the Higgs portal to the SM is ‘‘closed’’ for $\alpha = 0$ and the cross section of Direct Detection vanishes. This becomes apparent as a dip in Fig. 6.2g.

From Fig. 6.2 it can be seen that most points above the neutrino floor correspond to Higgs mixing angles with $\alpha < \pi/4$, but the single point that shows up in the region $m_\phi < m_h$ in Fig. 6.2d corresponds to $\alpha \approx -\pi/2$.

6.3 Behavior with Respect to Selected Parameters and Gauge Dependence

In order to examine how the cross section depends on individual parameters, we choose a parameter point from our scan that lies well above the neutrino floor in Fig. 6.1. Specifically, the point with

$$\begin{aligned} m_\phi &= 546.93 \text{ GeV}, \\ m_\chi &= 72.53 \text{ GeV}, \\ v_S &= 152.05 \text{ GeV}, \\ \alpha &= 0.224 \end{aligned} \tag{6.8}$$

is chosen, which corresponds to the cross section

$$f_{\chi\chi} \cdot \sigma = f_{\chi\chi} \cdot 2.16 \times 10^{-48} \text{ cm}^2 = 8.63 \times 10^{-49} \text{ cm}^2. \tag{6.9}$$

There is a green and a blue curve in all plots of Figs. 6.3–6.5a. The green curve corresponds

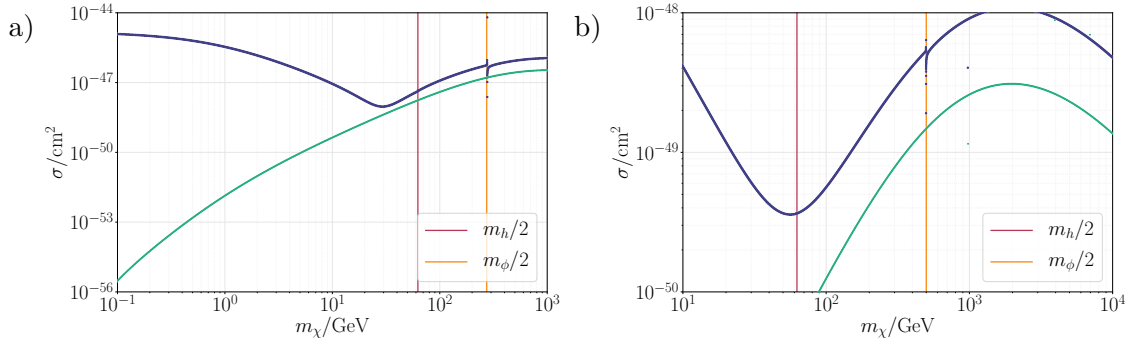


Figure 6.3: Dependence of selected parameter points on m_χ . In a, the parameter point of Eq. (6.8) was varied. In b, the selected parameter point is given by $m_\phi = 1$ TeV, $v_S = 2v$ and $\sin \alpha = 0.1$, as in [17].

to the approach of this work for the computation of the cross section, i. e. taking into account only the last diagram of Fig. 5.9. For the blue curve, all diagrams of Fig. 5.9 were taken into account. We will refer to this approach as “including all gluon diagrams”.

Fig. 6.3a shows the behavior of the selected parameter point upon variation of m_χ . While for m_χ values larger than 30 GeV the difference between the two approaches is roughly a factor of 3, the curves differ fundamentally for small masses m_χ . As it is argued in [82], the Goldstone nature of the DM candidate of the DCxSM entails that – in the limit of vanishing momentum transfer $t \rightarrow 0$ – only the U(1) breaking term of the Higgs potential 2.1 gives rise to non-vanishing loop corrections to the scattering between DM and a nucleon. Conversely, the Direct Detection cross section must vanish if U(1) is restored, which is equivalent to the limit $m_\chi \rightarrow 0$. This behavior is only revealed in our approach, but not if all gluon diagrams are taken into account.

Moreover, including all gluon diagrams gives rise to a pole at $m_\chi = m_\phi/2$ and – although it is hardly visible in Fig. 6.3a – also at $m_\chi = m_h/2$. These poles are introduced by the field-strength renormalization factors of the Higgs mediators and they are not canceled if all gluon diagrams are included (see the discussion in Sec. 5.3).

For comparison with the results of [17] consider Fig. 6.3b, where the parameter point to be varied is chosen accordingly. When including all gluon diagrams, as it is done in [17], their

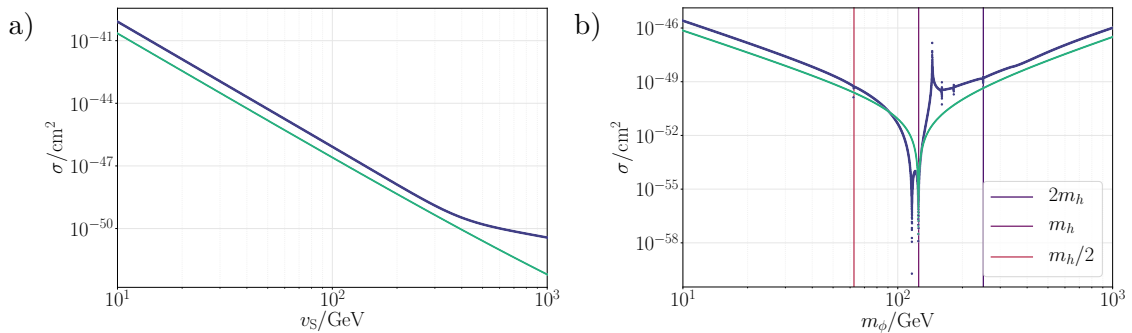


Figure 6.4: Dependence of the cross sections of selected parameter points on v_S and m_ϕ .

and our results differ by almost an order of magnitude.

While Fig. 6.4a, which illustrates the dependence of the cross section on v_S , only confirms the observation from Sec. 6.2 that a large value of the non-SM-like VEV suppresses the cross section, the dependence on m_ϕ shown in Fig. 6.4b reveals again a significant difference between the two approaches. While both have a pole for degenerate Higgs masses $m_\phi = m_h$ (this complies with the dip in Fig. 6.2b), including all gluon diagrams introduces several other poles, for example at $m_\phi = m_h/2$ and $m_\phi = 2m_h$.

In order to check our result for gauge invariance, we define the relative gauge dependence as

$$\Delta_\xi \sigma \equiv \frac{\sigma - \sigma|_{\xi=1}}{\sigma|_{\xi=1}}. \quad (6.10)$$

It is illustrated in Fig 6.5a. While in our approach there is no gauge dependence, including all gluon diagrams introduces a significant gauge dependence, which again can be traced back to the field-strength renormalization constants of the Higgs mediators.

Finally, we examine the contribution of the gluon box diagrams, that is the last diagram in Fig. 5.9, which is given in more detail in Fig. 5.10. Let $\sigma|_{\text{nogb}}$ be the cross section without the contribution of these gluon boxes, while σ is still the cross section computed in our approach, i. e. including the gluon box diagrams. The relative dependence of the cross section on the gluon box diagrams is then defined as

$$\Delta_{\text{gb}} \sigma \equiv \frac{\sigma - \sigma|_{\text{nogb}}}{\sigma|_{\text{nogb}}}. \quad (6.11)$$

This quantity is plotted against m_χ in Fig 6.5b. Obviously, the influence of the gluon box diagrams is in the sub-percentage region. Hence, not taking into account the gluon box diagrams and thereby treating all diagrams with external gluons in Fig. 5.9 consistently would not significantly alter the overall result.

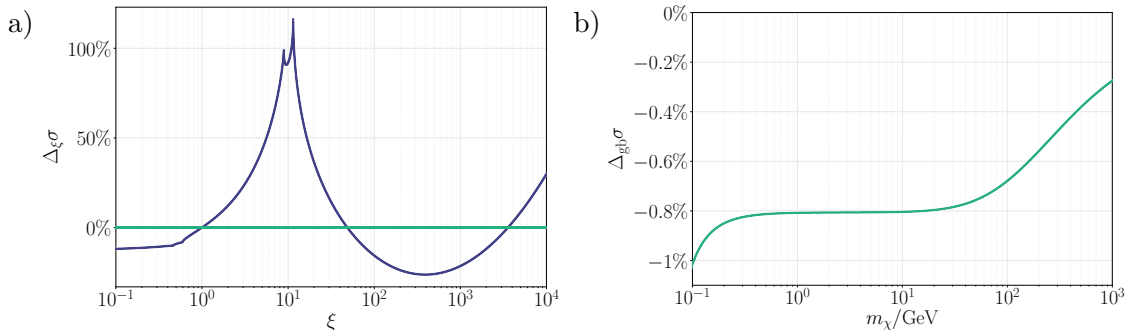


Figure 6.5: Gauge dependence and dependence on the gluon box diagrams. $\Delta_\xi \sigma$ and $\Delta_{\text{gb}} \sigma$ are defined in Eqs. (6.10) and (6.11), respectively.

CHAPTER 7

Conclusion

In this thesis the *Dark Complex Scalar Extension of the Standard Model* (DCxSM) was studied, which includes a DM candidate, and the spin-independent cross section for DM Direct Detection was computed. It was argued in Chapter 3 that the momentum transfer between the DM particle and the target nucleus in Direct Detection scattering processes is negligibly small and in Chapter 5 it was shown that the cross section therefore vanishes at tree level. Hence, it is required to also compute the higher-order electroweak corrections to this process, which was the major part of this work.

As a general feature of Quantum Field Theories, higher-order corrections introduce infinities, which need to be taken care of by renormalization. Chapter 4 was dedicated to the elaboration of the renormalization procedure specific to the Direct Detection process in the DCxSM. Moreover, the computation required the application of certain approximations for being able to match the analytical results to the effective Lagrangian, which is necessary for the incorporation of nuclear physics. They were worked out in Chapter 5.

Finally, after the analytical calculation of the Direct Detection cross section, the result has been numerically analyzed in Chapter 6 by performing a parameter scan. It turned out that for xenon based Direct Detection experiments there are parameter points above the background due to neutrino–xenon scattering. Hence, prospective experiments that reach sufficiently high sensitivities will either detect a signal which can be explained within the DCxSM or exclude certain parameter points of the DCxSM.

Furthermore, the standard approach in the literature – which takes into account a certain subset of the two-loop diagrams with external gluons – was compared to the approach of this work, where consistently only one-loop diagrams were taken into account.¹ In the former approach the behavior of the cross section fundamentally differs from what is expected due to the Goldstone nature of the DM candidate in the DCxSM, whereas in our approach the proper behavior (the vanishing of the cross section in the limit of vanishing DM mass) was observed.

Further research would be required in order to consistently take into account the diagrams with external gluons given in Fig. 5.9, which is only possible by additionally computing the corresponding diagram with the two-loop correction to the gluon–Higgs vertex.

¹ While this approach did also include the effective two-loop box and triangles diagrams with external gluons, it was shown that dropping their contributions does not significantly alter the result.

APPENDIX A

The Higgs Mass Mixing Angle

For the purpose of deriving Eqs. (2.15), let us abbreviate the Higgs mass mixing matrix as¹

$$\mathcal{M}^2 = \begin{pmatrix} a & c \\ c & b \end{pmatrix}, \quad \text{where} \quad a = \lambda_{\text{H}}v^2, \quad b = \lambda_{\text{S}}v_{\text{S}}^2, \quad c = \lambda_{\text{HS}}vv_{\text{S}}. \quad (\text{A.1})$$

Computing the matrix product $R\mathcal{M}^2R^{-1}$ explicitly, Eq. (2.13) can be given as

$$\begin{pmatrix} a \cos^2 \alpha + 2c \cos \alpha \sin \alpha + b \sin^2 \alpha & (b - a) \cos \alpha \sin \alpha + c (\cos^2 \alpha - \sin^2 \alpha) \\ (b - a) \cos \alpha \sin \alpha + c (\cos^2 \alpha - \sin^2 \alpha) & a \sin^2 \alpha - 2c \cos \alpha \sin \alpha + b \cos^2 \alpha \end{pmatrix} \\ \stackrel{!}{=} \begin{pmatrix} m_1^2 & 0 \\ 0 & m_2^2 \end{pmatrix}. \quad (\text{A.2})$$

These four equations in (A.2) (two of which are equal) define α . Since a shift $\alpha \rightarrow \alpha + \pi$ turns $R \rightarrow -R$ and therefore does not affect $R\mathcal{M}^2R^{-1}$ and the defining equations for α , one may assume $-\pi/2 \leq \alpha < \pi/2$.

From the vanishing off-diagonal elements in Eq. (A.2) follows

$$\tan 2\alpha = \frac{2c}{a - b} = \frac{2\lambda_{\text{HS}}vv_{\text{S}}}{\lambda_{\text{H}}v^2 - \lambda_{\text{S}}v_{\text{S}}^2}. \quad (\text{A.3})$$

Unfortunately, since $\tan 2\alpha$ is not injective on $[-\pi/2, \pi/2]$, this equation does not unambiguously determine α . However, the diagonal elements of Eq. (A.2) have not been used so far. Subtracting them from each other and plugging in $a - b$ from Eq. (A.3) yields

$$m_2^2 - m_1^2 = -(a - b) \cos 2\alpha - 2c \sin 2\alpha = -\frac{2c}{\sin 2\alpha}. \quad (\text{A.4})$$

Solving this equation for $\sin 2\alpha$ gives the second relation in (2.15). The identity for $\cos 2\alpha$ is trivially derived from the expression of $\tan 2\alpha$ and $\sin 2\alpha$.

¹ This derivation was inspired by [83].

APPENDIX B

Vanishing Propagator and Vertex Corrections

In Sec. 5.2.1, the electroweak propagator and vertex corrections to the DM Direct Detection process in the DCxSM have been discussed. There, only diagrams were considered where the mediator is a Higgs boson, i. e. either h_1 or h_2 . While Feynman rules do also give rise to diagrams with other electroweak mediators, they all vanish identically. In this appendix, we will consider these diagrams – which are given in Fig. B.1 – one by one and explain why they do not contribute.

In this section we are going to use the convention that p_1 and p_2 are the incoming and outgoing quark four-momenta, respectively. $q = p_2 - p_1$ is the momentum transfer and k is the loop momentum. That is, for the diagrams that are discussed in this section, the momenta are defined as in Fig. B.2.

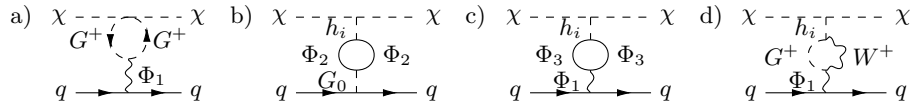


Figure B.1: One-loop electroweak propagator and vertex corrections with mediators other than the Higgs boson. Here, the following abbreviations were used:

$$\begin{aligned}
 i &= 1, 2, \\
 \Phi_1 &= \gamma, Z, \\
 \Phi_2 &= f, \eta_{\pm}, \\
 \Phi_3 &= f, W^+, G^+, \eta_{\pm}.
 \end{aligned}$$

Furthermore, $f = u, c, t, d, s, b, e, \mu, \tau$ stands for all charged fermions.

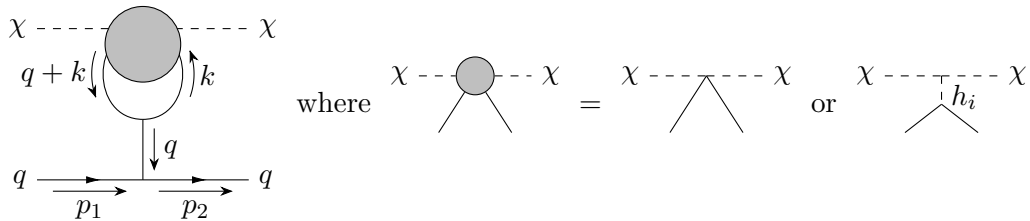


Figure B.2: The momentum convention that is used in this appendix. The blob describes the interaction of the DM particle with two arbitrary particles either via a four vertex (as in Fig. B.1a) or alternatively via a Higgs boson propagator (as in Fig. B.1b–d).

Using this convention, the diagrams in Fig. B.1 vanish for the following reasons:

Fig. B.1a:

From Eq. (2.10) it is apparent that the vertex factor of the $\chi^2 |G^+|^2$ vertex is scalar and constant.¹ On the other hand, both the vertices $\gamma |G^+|^2$ and $Z |G^+|^2$ are proportional to $q^\mu + 2k^\mu$ [84]. The term with k^μ vanishes by integration over the loop momentum, since the factor of k^μ will make the integrand odd. The momentum transfer q^μ forms a dot product with the vector boson Feynman propagator $D_F^{\mu\nu}(q)$, which yields $q_\mu D_F^{\mu\nu}(q) \sim q^\nu$ for any gauge. This q^ν will then be dotted into the γ^μ matrix of the $\bar{q}q\Phi_1$ vertex, where it produces the expression

$$\bar{u}_{p_2} \not{q} u_{p_1} = \bar{u}_{p_2} (\not{\psi}_2 - \not{\psi}_1) u_{p_1}, \quad (\text{B.1})$$

which vanishes after applying the Dirac equation $\bar{u}_p (\not{\psi} - m) = (\not{\psi} - m) u_p = 0$.

Fig. B.1b, $\Phi_2 = f$:

The vertex factor of the $\bar{f}f h_i$ vertex is scalar and constant for any fermion f . On the other hand, the vertex factor of the $\bar{f}f G^0$ vertex is proportional to γ^5 [84]. Hence, the trace of the loop has the structure

$$\text{Tr}(\not{k} + m) \gamma^5 (\not{q} + \not{k} + m) = 0, \quad (\text{B.2})$$

which vanishes, since $\text{Tr} \gamma^5 = \text{Tr} \gamma^5 \gamma^\mu = \text{Tr} \gamma^5 \gamma^\mu \gamma^\nu = 0$.

Fig. B.1b, $\Phi_2 = \eta_\pm$:

The two diagrams of B.1b with $\Phi_3 = \eta_+$ and $\Phi_3 = \eta_-$ precisely cancel each other, because η_+ and η_- have identical propagators and the vertices $\eta_+^2 h_i$ and $\eta_-^2 h_i$ have identical vertex factors, but the vertices $\eta_+^2 G_0$ and $\eta_-^2 G_0$ yield a relative minus sign [84].

Fig. B.1c, $\Phi_3 = f$:

Since the vertex factor of the $\bar{f}f h_i$ vertex is scalar and constant for any fermion f [84] and the vertex factor of the $\bar{f}f \Phi_1$ vertex ($\Phi_1 = \gamma, Z$) is proportional to $\gamma^\mu (1 + a\gamma^5)$ (for some scalar a) [84], the trace of the fermion loop has the structure

$$\text{Tr}(\not{k} + m) \gamma^\mu (1 + a\gamma^5) (\not{q} + \not{k} + m) = 4m(q^\mu + 2k^\mu). \quad (\text{B.3})$$

Here it was used that the trace over an odd number of γ matrices vanishes and so does the trace over a product of up to three γ matrices together with γ^5 . Thus, the argument that holds for the diagram in Fig. B.1a can also be applied in this case.

¹ In this appendix, “constant” means *momentum independent* and “scalar” means *not containing a γ matrix*.

Fig. B.1c, $\Phi_3 = W^+$:

The coupling between a Higgs boson h_i and two W^+ bosons is constant, scalar and proportional to $g^{\eta\kappa}$ [84]. The coupling between γ or Z and two W^+ is proportional to [84]

$$V_{\sigma\rho\mu}(q, k) \equiv -g_{\sigma\rho}(q + 2k)_\mu + g_{\rho\mu}(2q + k)_\sigma + g_{\mu\sigma}(k - q)_\rho. \quad (\text{B.4})$$

If $D_a^{\mu\nu}(p)$ is the propagator of vector bosons $a = \gamma, Z, W^+$, then the structure of the loop together with the $\Phi_1 = \gamma, Z$ propagator reads

$$L^\nu \equiv g_{\eta\kappa} D_W^{\sigma\eta}(k) D_W^{\rho\kappa}(q + k) V_{\sigma\rho\mu}(q, k) D_{\Phi_1}^{\mu\nu}(q). \quad (\text{B.5})$$

ν is the only free index of this expression, which can – after performing all possible contractions – only be carried by either q or k , since none of the objects in Eq. (B.5) contains a γ matrix. Thus, L^ν must be of the form

$$L^\nu = A(q^2, k^2)q^\nu + B(q^2, k^2)k^\nu, \quad (\text{B.6})$$

where A and B are arbitrary functions. Consequently, the argument that holds for the diagram in Fig. B.1a also works in this case.

Fig. B.1c, $\Phi_3 = G^+$:

The vertex factor of the $h_i |G^+|^2$ vertex is scalar and constant [84]. Thus, the argument for diagram B.1a also works in this case.

Fig. B.1c, $\Phi_3 = \eta_\pm$:

The vertex of h_i and two charged ghosts is scalar and constant [84], whereas the vertex of γ or Z and two charged ghosts is proportional to q^μ [84]. Thus, the argument for diagram B.1a also works in this case.

Fig. B.1d:

The vertex factor of the $h_i G^+ W^+$ vertex is proportional to $2q^\sigma + k^\sigma$. The vertex factor of the $\Phi_1 G^+ W^+$ vertex is a constant and proportional to $g^{\rho\mu}$ [84]. Similarly to the case B.1c for $\Phi_3 = W^+$, the structure of the loop together with the propagator of $\Phi_1 = \gamma, Z$ is given by

$$L^\nu \equiv (2q + k)_\sigma D_W^{\sigma\rho} g_{\rho\mu} D_{\Phi_1}^{\mu\nu}. \quad (\text{B.7})$$

Again, the free index can only be carried by either q or k and the argument of the case B.1c for $\Phi_3 = W^+$, can also be applied here.

Glossary

| | |
|-------------|---|
| 1PI | One-Particle Irreducible |
| CERN | European Organization for Nuclear Research |
| CKM mixing | Cabibbo–Kobayashi–Maskawa mixing |
| CP | Charge Conjugation and Parity |
| DCxSM | Dark Complex Scalar Extension of the Standard Model |
| DM | Dark Matter |
| EFT | Effective Field Theory |
| IR | Infrared |
| KOSY scheme | Mixing Angle Renormalization Scheme of Kanemura, Okada, Senaha and Yuan |
| LHC | Large Hadron Collider |
| MS | Minimal Subtraction |
| NLO | Next-to-Leading Order |
| NNLO | Next-to-Next-to-Leading Order |
| QCD | Quantum Chromodynamics |
| QED | Quantum Electrodynamics |
| QFT | Quantum Field Theory |
| SM | Standard Model of Elementary Particles |
| UV | Ultraviolet |
| VEV | Vacuum Expectation Value |
| WIMP | Weakly Interacting Massive Particle |

List of Figures

| | | |
|------|--|----|
| 3.1 | Channels for DM Detection | 7 |
| 3.2 | Kinematics of Direct Detection | 8 |
| 3.3 | Limits of Liquid Xenon Based Direct Detection Experiments | 17 |
| 4.1 | Classes of Higher-Order Corrections to Direct Detection | 19 |
| 4.2 | Counterterms required for Direct Detection | 20 |
| 4.3 | Sum of the Photon Propagator Correction and the QED Vertex Correction | 42 |
| 4.4 | Coupling of a Photon to a Fermion via a Z Boson | 43 |
| 4.5 | Cancellation of the Z Factors | 45 |
| 4.6 | One-Loop Corrections to the Higgs Propagator | 47 |
| 4.7 | One-Loop Corrections to the Higgs Tadpole | 47 |
| 4.8 | One-Loop Corrections to the Dark Matter Propagator | 47 |
| 4.9 | One-Loop Electroweak Corrections to the Quark Propagator | 47 |
| 4.10 | One-Loop Corrections to the Electroweak Gauge Boson Propagator | 48 |
| 5.1 | Schematic Direct Detection Scattering | 49 |
| 5.2 | One-Loop Electroweak Corrections to DM–Quark Scattering | 50 |
| 5.3 | Possible Mediators of Triangle Diagrams | 50 |
| 5.4 | One-Loop Electroweak Corrections to the Higgs Boson Propagator | 51 |
| 5.5 | One-Loop Electroweak Corrections to the DM–Higgs Boson Vertex | 51 |
| 5.6 | One-Loop Electroweak Corrections to the Quark–Higgs Boson Vertex | 51 |
| 5.7 | Triangle and Box Diagram Topologies for DM–Quark Scattering | 52 |
| 5.8 | DM–Gluon Interaction via a Higgs Boson Mediator and a Quark Loop | 54 |
| 5.9 | Possible Corrections to DM–Gluon Scattering | 54 |
| 5.10 | Triangle and Box Diagrams with External Gluons | 57 |
| 5.11 | Box Diagram with External Gluons with Effective Gluon–Higgs Coupling | 57 |
| 6.1 | Limits of Liquid Xenon Based Direct Detection Experiments with the DCxSM Parameter Sample | 69 |
| 6.2 | Parameter Scan | 70 |
| 6.3 | Dependence of a Selected Parameter Point on m_χ | 72 |
| 6.4 | Dependence of a Selected Parameter Point on v_S and m_ϕ | 72 |
| 6.5 | Gauge Dependence and Dependence on the Gluon Box Diagrams | 73 |
| B.1 | Vanishing One-Loop Electroweak Propagator and Vertex Corrections | 79 |
| B.2 | Momentum Convention for Examining Vanishing Propagator and Vertex Cor- rections | 79 |

List of Tables

| | |
|---------------------------------------|----|
| 4.1 Definitions of Φ_i | 46 |
|---------------------------------------|----|

List of Used Software

The purpose of following list of software that was used for this work is to be fully transparent about how this work was elaborated and to give the authors of this software the credit they deserve. The short descriptions of the software were taken from their websites or paper abstracts.

| | | |
|--------------|----------|--|
| COLLIER | [63] | A fortran library for the numerical evaluation of one-loop scalar and tensor integrals appearing in perturbative relativistic QFT. |
| FEYNARTS | [85] | A Mathematica package for the generation and visualization of Feynman diagrams and amplitudes. |
| FEYNCALC | [86, 87] | A Mathematica package for symbolic evaluation of Feynman diagrams and algebraic calculations in QFT and elementary particle physics. |
| HIGGSBOUNDS | [77–79] | A code that uses the experimental topological cross section limits from Higgs searches at LEP, the Tevatron and the LHC to determine if a given parameter point has been excluded at 95% C. L. |
| HIGGSSIGNALS | [80] | A code that performs a statistical test of the Higgs sector predictions of arbitrary models (using the HiggsBounds input routines) with the measurements of Higgs boson signal rates and masses from the Tevatron and the LHC. |
| LOOPTOOLS | [88, 89] | A package for evaluation of scalar and tensor one-loop integrals based on the FF package by G. J. van Oldenborgh. |
| MICROMEGAS | [51] | A code for the calculation of Dark Matter properties including the relic density, direct and indirect rates in a general supersymmetric model and other models of New Physics. |
| PACKAGE-X | [90] | A Mathematica package for the analytic computation of one-loop integrals. |
| SARAH | [91] | A Mathematica package for building and analyzing SUSY and non-SUSY models and writing model files for FeynArts. |
| SCANNERS-2 | [73–76] | A C++ tool for scanning the parameter space of arbitrary scalar extensions of the Standard Model. |
| TIKZ-FEYNMAN | [92] | A LaTeX package to draw Feynman diagrams. |

Bibliography

1. DIRAC, PAUL A.M.: ‘Quantum theory of emission and absorption of radiation’. *Proc. Roy. Soc. Lond. A* (1927), vol. A114: p. 243 (cit. on p. 1).
2. SHIFMAN, M.: *Advanced Topics in Quantum Field Theory: A Lecture Course*. Cambridge University Press, 2012 (cit. on p. 1).
3. OPPENHEIMER, J. R.: ‘Note on the Theory of the Interaction of Field and Matter’. *Phys. Rev.* (5 Mar. 1930), vol. 35: pp. 461–477. URL: <https://link.aps.org/doi/10.1103/PhysRev.35.461> (cit. on p. 1).
4. MANOUKIAN, E.B.: *Renormalization*. ISSN. Elsevier Science, 1983 (cit. on p. 1).
5. HIGGS, PETER W.: ‘Broken symmetries, massless particles and gauge fields’. *Phys. Lett.* (1964), vol. 12: pp. 132–133 (cit. on p. 1).
6. ENGLERT, F. and R. BROUT: ‘Broken Symmetry and the Mass of Gauge Vector Mesons’. *Phys. Rev. Lett.* (1964), vol. 13. Ed. by TAYLOR, J.C.: pp. 321–323 (cit. on p. 1).
7. GURALNIK, G.S., C.R. HAGEN, and T.W.B. KIBBLE: ‘Global Conservation Laws and Massless Particles’. *Phys. Rev. Lett.* (1964), vol. 13. Ed. by TAYLOR, J.C.: pp. 585–587 (cit. on p. 1).
8. CHATRCHYAN, SERGUEI et al.: ‘Observation of a New Boson at a Mass of 125 GeV with the CMS Experiment at the LHC’. *Phys. Lett.* (2012), vol. B716: pp. 30–61. arXiv: 1207.7235 [hep-ex] (cit. on p. 1).
9. AAD, GEORGES et al.: ‘Observation of a new particle in the search for the Standard Model Higgs boson with the ATLAS detector at the LHC’. *Phys. Lett.* (2012), vol. B716: pp. 1–29. arXiv: 1207.7214 [hep-ex] (cit. on p. 1).
10. KINOSHITA, T.: *Quantum Electrodynamics*. Advanced series on directions in high energy physics. World Scientific, 1990 (cit. on p. 1).
11. TANABASHI, M. ET. AL.: ‘Review of Particle Physics’. *Phys. Rev. D* (3 Aug. 2018), vol. 98: p. 0300012. URL: <https://link.aps.org/doi/10.1103/PhysRevD.98.030001> (cit. on pp. 1, 5, 67, 68).
12. ZWICKY, F.: ‘Die Rotverschiebung von extragalaktischen Nebeln’. *Helv. Phys. Acta* (1933), vol. 6: pp. 110–127. URL: <http://articles.adsabs.harvard.edu/pdf/1933AChPh...6..110Z> (cit. on p. 1).
13. BERTONE, GIANFRANCO and DAN HOOPER: ‘History of dark matter’. *Rev. Mod. Phys.* (2018), vol. 90(4): p. 045002. arXiv: 1605.04909 [astro-ph.CO] (cit. on pp. 1, 2, 16).
14. MEEKINS, JOHN F., GILBERT FRITZ, TALBOT A. CHUBB, H. FRIEDMAN, and RICHARD C. HENRY: ‘Physical Sciences: X-rays from the Coma Cluster of Galaxies’. *Nature* (1971), vol. 231: pp. 107–108 (cit. on p. 2).

15. STEIGMAN, GARY, BASUDEB DASGUPTA, and JOHN F. BEACOM: ‘Precise Relic WIMP Abundance and its Impact on Searches for Dark Matter Annihilation’. *Phys. Rev. D* (2012), vol. 86: p. 023506. arXiv: 1204.3622 [hep-ph] (cit. on p. 2).
16. IVANOV, IGOR P.: ‘Building and testing models with extended Higgs sectors’. *Prog. Part. Nucl. Phys.* (2017), vol. 95: pp. 160–208. arXiv: 1702.03776 [hep-ph] (cit. on p. 2).
17. ISHIWATA, KOJI and TAKASHI TOMA: ‘Probing pseudo Nambu-Goldstone boson dark matter at loop level’. *JHEP* (2018), vol. 12: p. 089. arXiv: 1810.08139 [hep-ph] (cit. on pp. 2, 3, 5, 6, 14, 16, 54, 72).
18. AZEVEDO, DUARTE, MATEUSZ DUCH, BOHDAN GRZADKOWSKI, DA HUANG, MICHAL IGLICKI, and RUI SANTOS: ‘Testing scalar versus vector dark matter’. *Phys. Rev.* (2019), vol. D99(1): p. 015017. arXiv: 1808.01598 [hep-ph] (cit. on p. 3).
19. AAD, GEORGES et al.: ‘Combined Measurement of the Higgs Boson Mass in pp Collisions at $\sqrt{s} = 7$ and 8 TeV with the ATLAS and CMS Experiments’. *Phys. Rev. Lett.* (2015), vol. 114: p. 191803. arXiv: 1503.07589 [hep-ex] (cit. on pp. 5, 67).
20. ARCADI, GIORGIO, ABDELHAK DJOUADI, and MARTTI RAIDAL: ‘Dark Matter through the Higgs portal’. (2019), vol. arXiv: 1903.03616 [hep-ph] (cit. on p. 6).
21. MO, H., F. van den BOSCH, and S. WHITE: *Galaxy Formation and Evolution*. Galaxy Formation and Evolution. Cambridge University Press, 2010 (cit. on p. 7).
22. SCHNEIDER, PETER: *Einführung in die extragalaktische Astronomie und Kosmologie*. Springer-Verlag, 2006 (cit. on p. 7).
23. MARRODÁN UNDAGOITIA, TERESA and LUDWIG RAUCH: ‘Dark matter direct-detection experiments’. *J. Phys.* (2016), vol. G43(1): p. 013001. arXiv: 1509.08767 [physics.ins-det] (cit. on pp. 7, 8, 10, 16).
24. BOVEIA, ANTONIO and CATERINA DOGLIONI: ‘Dark Matter Searches at Colliders’. *Ann. Rev. Nucl. Part. Sci.* (2018), vol. 68: pp. 429–459. arXiv: 1810.12238 [hep-ex] (cit. on p. 7).
25. CONRAD, JAN: ‘Indirect Detection of WIMP Dark Matter: a compact review’. *Interplay between Particle and Astroparticle physics (IPA2014) London, United Kingdom, August 18-22, 2014*. 2014. arXiv: 1411.1925 [hep-ph] (cit. on p. 7).
26. AARTSEN, M. G. et al.: ‘Search for Dark Matter Annihilations in the Sun with the 79-String IceCube Detector’. *Phys. Rev. Lett.* (13 Mar. 2013), vol. 110: p. 131302. URL: <https://link.aps.org/doi/10.1103/PhysRevLett.110.131302> (cit. on p. 7).
27. CHOI, K. et al.: ‘Search for Neutrinos from Annihilation of Captured Low-Mass Dark Matter Particles in the Sun by Super-Kamiokande’. *Phys. Rev. Lett.* (14 Apr. 2015), vol. 114: p. 141301. URL: <https://link.aps.org/doi/10.1103/PhysRevLett.114.141301> (cit. on p. 7).
28. BERNABEI, R. et al.: ‘The DAMA/LIBRA apparatus’. *Nucl. Instrum. Meth.* (2008), vol. A592: pp. 297–315. arXiv: 0804.2738 [astro-ph] (cit. on p. 8).

-
29. APRILE, E. et al.: ‘The XENON100 dark matter experiment’. *Astroparticle Physics* (Apr. 2012), vol. 35(9): pp. 573–590. arXiv: 1107.2155 [astro-ph.IM] (cit. on pp. 8, 9, 16).
 30. LIN, TONGYAN: *TASI lectures on dark matter models and direct detection*. 2019. arXiv: 1904.07915 [hep-ph] (cit. on pp. 8–12).
 31. SMITH, MARTIN C. et al.: ‘The RAVE Survey: Constraining the Local Galactic Escape Speed’. *Mon. Not. Roy. Astron. Soc.* (2007), vol. 379: pp. 755–772. arXiv: astro-ph/0611671 [astro-ph] (cit. on p. 8).
 32. BAUER, MARTIN and TILMAN PLEHN: ‘Yet Another Introduction to Dark Matter’. *Lect. Notes Phys.* (2019), vol. 959: pp.–. arXiv: 1705.01987 [hep-ph] (cit. on p. 9).
 33. PROFUMO, STEFANO [VERFASSERIN]: *An introduction to particle dark matter*. Advanced textbooks in physics. New Jersey: World Scientific, 2017 (cit. on p. 10).
 34. PESKIN, MICHAEL E. and DANIEL V. SCHROEDER: *An Introduction to quantum field theory*. Reading, USA: Addison-Wesley, 1995. URL: <http://www.slac.stanford.edu/~mpeskin/QFT.html> (cit. on pp. 11, 19–22, 24, 36, 38, 42, 43, 55, 59, 63).
 35. SCHWARTZ, MATTHEW D.: *Quantum Field Theory and the Standard Model*. Cambridge University Press, 2014. URL: <http://www.cambridge.org/us/academic/subjects/physics/theoretical-physics-and-mathematical-physics/quantum-field-theory-and-standard-model> (cit. on pp. 11, 15, 22, 24, 29, 58, 59).
 36. STEPPELER, PATRICK NORBERT: ‘Radiative corrections for the direct detection of neutralino dark matter and its relic density’. PhD thesis. Munster U., ITP, 2016. URL: https://www.uni-muenster.de/Physik.TP/archive/fileadmin/Arbeiten/steppeeler_phd.pdf (cit. on pp. 13–15).
 37. ERTAS, FATIHA and FELIX KAHLHOEFER: ‘Loop-induced direct detection signatures from CP-violating scalar mediators’. *JHEP* (2019), vol. 06: p. 052. arXiv: 1902.11070 [hep-ph] (cit. on pp. 15, 16, 53, 54, 57, 62–64, 68).
 38. HISANO, JUNJI: ‘Effective theory approach to direct detection of dark matter’. (2017), vol. arXiv: 1712.02947 [hep-ph] (cit. on pp. 15, 55).
 39. GLAUS, S., M. MÜHLEITNER, J. MÜLLER, S. PATEL, and R. SANTOS: ‘Electroweak Corrections to Dark Matter Direct Detection in a Vector Dark Matter Model’. *JHEP* (2019), vol. 10: p. 152. arXiv: 1908.09249 [hep-ph] (cit. on pp. 16, 18, 71).
 40. TAN, ANDI et al.: ‘Dark Matter Results from First 98.7 Days of Data from the PandaX-II Experiment’. *Phys. Rev. Lett.* (2016), vol. 117(12): p. 121303. arXiv: 1607.07400 [hep-ex] (cit. on pp. 16, 17, 69).
 41. AKERIB, D. S. et al.: ‘Results from a search for dark matter in the complete LUX exposure’. *Phys. Rev. Lett.* (2017), vol. 118(2): p. 021303. arXiv: 1608.07648 [astro-ph.CO] (cit. on pp. 16, 17, 69).
 42. ANGLE, J. et al.: ‘First Results from the XENON10 Dark Matter Experiment at the Gran Sasso National Laboratory’. *Phys. Rev. Lett.* (2008), vol. 100: p. 021303. arXiv: 0706.0039 [astro-ph] (cit. on pp. 16, 17, 69).

43. APRILE, E. et al.: ‘XENON100 Dark Matter Results from a Combination of 477 Live Days’. *Phys. Rev.* (2016), vol. D94(12): p. 122001. arXiv: 1609.06154 [astro-ph.CO] (cit. on pp. 16, 17, 69).
44. APRILE, E. et al.: ‘Dark Matter Search Results from a One Ton-Year Exposure of XENON1T’. *Phys. Rev. Lett.* (2018), vol. 121(11): p. 111302. arXiv: 1805.12562 [astro-ph.CO] (cit. on pp. 16, 17, 69).
45. MORIYAMA, S.: *Direct Dark Matter Search with XENONnT*. 2019. URL: http://www.lowbg.org/ugnd/workshop/sympo_all/201903_Sendai/slides/8am/8am_6.pdf (cit. on pp. 16, 17, 69).
46. BILLARD, J., L. STRIGARI, and E. FIGUEROA-FELICIANO: ‘Implication of neutrino backgrounds on the reach of next generation dark matter direct detection experiments’. *Phys. Rev.* (2014), vol. D89(2): p. 023524. arXiv: 1307.5458 [hep-ph] (cit. on pp. 16, 17, 69).
47. DESAI, ANAND and ALEX MOSKOWITZ: ‘DMTools – Dark Matter Limit Plot Generator’. (2013), vol. URL: <http://dmttools.brown.edu> (cit. on pp. 17, 69).
48. LIU, JIANGLAI, XUN CHEN, and XIANGDONG JI: ‘Current status of direct dark matter detection experiments’. *Nature Phys.* (2017), vol. 13(3): pp. 212–216. arXiv: 1709.00688 [astro-ph.CO] (cit. on p. 16).
49. AHLÉN, S. P., F. T. AVIGNONE, R. L. BRODZINSKI, A. K. DRUKIER, G. GELMINI, and D. N. SPERGEL: ‘Limits on Cold Dark Matter Candidates from an Ultralow Background Germanium Spectrometer’. *Phys. Lett.* (1987), vol. B195: pp. 603–608 (cit. on p. 16).
50. ADE, P.A.R. et al.: ‘Planck 2015 results. XIII. Cosmological parameters’. *Astron. Astrophys.* (2016), vol. 594: A13. arXiv: 1502.01589 [astro-ph.CO] (cit. on p. 17).
51. BÉLANGER, GENEVIÈVE, FAWZI BOUDJEMA, ANDREAS GOUDELIS, ALEXANDER PUKHOV, and BRYAN ZALDIVAR: ‘micrOMEGAs5.0 : Freeze-in’. *Comput. Phys. Commun.* (2018), vol. 231: pp. 173–186. arXiv: 1801.03509 [hep-ph] (cit. on pp. 17, 68, 86).
52. READ, J. I.: ‘The Local Dark Matter Density’. *J. Phys.* (2014), vol. G41: p. 063101. arXiv: 1404.1938 [astro-ph.GA] (cit. on p. 18).
53. POLCHINSKI, JOSEPH: ‘Renormalization and Effective Lagrangians’. *Nucl. Phys. B* (1984), vol. 231: pp. 269–295 (cit. on p. 21).
54. BOLLINI, C.G. and J.J. GIAMBIAGI: ‘Dimensional Renormalization: The Number of Dimensions as a Regularizing Parameter’. *Nuovo Cim. B* (1972), vol. 12: pp. 20–26 (cit. on p. 21).
55. AOKI, K. I., Z. HIOKI, M. KONUMA, R. KAWABE, and T. MUTA: ‘Electroweak Theory. Framework of On-Shell Renormalization and Study of Higher Order Effects’. *Prog. Theor. Phys. Suppl.* (1982), vol. 73: pp. 1–225 (cit. on p. 26).
56. KRAUSE, MARCEL: ‘On the Renormalization of the Two-Higgs-Doublet Model’. MA thesis. KIT, Karlsruhe, TP, 2016. URL: https://www.itp.kit.edu/_media/publications/masterthesismarcel.pdf (cit. on pp. 27, 31, 40).

-
57. FLEISCHER, J. and F. JEGERLEHNER: ‘Radiative corrections to Higgs-boson decays in the Weinberg-Salam model’. *Phys. Rev. D* (9 May 1981), vol. 23: pp. 2001–2026. URL: <https://link.aps.org/doi/10.1103/PhysRevD.23.2001> (cit. on p. 30).
 58. KRAUSE, MARCEL, ROBIN LORENZ, MARGARETE MUHLLEITNER, RUI SANTOS, and HANNA ZIESCHE: ‘Gauge-independent Renormalization of the 2-Higgs-Doublet Model’. *JHEP* (2016), vol. 09: p. 143. arXiv: 1605.04853 [hep-ph] (cit. on p. 31).
 59. KANEMURA, SHINYA, YASUHIRO OKADA, EIBUN SENAHA, and C.-P. YUAN: ‘Higgs coupling constants as a probe of new physics’. *Phys. Rev. D* (2004), vol. 70: p. 115002. arXiv: hep-ph/0408364 (cit. on pp. 31, 32).
 60. DENNER, ANSGAR, STEFAN DITTMAIER, and JEAN-NICOLAS LANG: ‘Renormalization of mixing angles’. *JHEP* (2018), vol. 11: p. 104. arXiv: 1808.03466 [hep-ph] (cit. on pp. 31, 32, 54).
 61. DENNER, ANSGAR and STEFAN DITTMAIER: ‘Electroweak Radiative Corrections for Collider Physics’. (2019), vol. arXiv: 1912.06823 [hep-ph] (cit. on pp. 35–37).
 62. HUBBARD, J.H. and B.B. HUBBARD: *Vector Calculus, Linear Algebra, and Differential Forms: A Unified Approach*. Prentice Hall, 1999 (cit. on p. 40).
 63. DENNER, ANSGAR, STEFAN DITTMAIER, and LARS HOFER: ‘Collier: a fortran-based Complex One-Loop LIbrary in Extended Regularizations’. *Comput. Phys. Commun.* (2017), vol. 212: pp. 220–238. arXiv: 1604.06792 [hep-ph] (cit. on pp. 40, 86).
 64. JEGERLEHNER, FRED: ‘Renormalizing the Standard Model’. (2019), vol. URL: <http://www-com.physik.hu-berlin.de/~fjeger/fj/doc/tasi.pdf> (cit. on p. 42).
 65. DENNER, ANSGAR: ‘Techniques for calculation of electroweak radiative corrections at the one loop level and results for W physics at LEP-200’. *Fortsch. Phys.* (1993), vol. 41: pp. 307–420. arXiv: 0709.1075 [hep-ph] (cit. on p. 42).
 66. DEMTRÖDER, W.: *Experimentalphysik 4: Kern-, Teilchen- und Astrophysik*. Springer-Lehrbuch. Springer Berlin Heidelberg, 2013 (cit. on p. 53).
 67. ABE, TOMOHIRO, MOTOKO FUJIWARA, and JUNJI HISANO: ‘Loop corrections to dark matter direct detection in a pseudoscalar mediator dark matter model’. *JHEP* (2019), vol. 02: p. 028. arXiv: 1810.01039 [hep-ph] (cit. on p. 53).
 68. SHIFMAN, MIKHAIL A., A. I. VAINSHTEIN, and VALENTIN I. ZAKHAROV: ‘Remarks on Higgs Boson Interactions with Nucleons’. *Phys. Lett.* (1978), vol. 78B: pp. 443–446 (cit. on pp. 55, 56).
 69. JI, XIANG-DONG: ‘Breakup of hadron masses and energy - momentum tensor of QCD’. *Phys. Rev.* (1995), vol. D52: pp. 271–281. arXiv: hep-ph/9502213 [hep-ph] (cit. on p. 55).
 70. BELANGER, G., F. BOUDJEMA, A. PUKHOV, and A. SEMENOV: ‘Dark matter direct detection rate in a generic model with micrOMEGAs 2.2’. *Comput. Phys. Commun.* (2009), vol. 180: pp. 747–767. arXiv: 0803.2360 [hep-ph] (cit. on p. 56).
 71. NOVIKOV, V. A., MIKHAIL A. SHIFMAN, A. I. VAINSHTEIN, and VALENTIN I. ZAKHAROV: ‘Calculations in External Fields in Quantum Chromodynamics. Technical Review’. *Fortsch. Phys.* (1984), vol. 32: p. 585 (cit. on pp. 57, 60).

72. DITTMAYER, S. et al.: ‘Handbook of LHC Higgs Cross Sections: 1. Inclusive Observables’. (Jan. 2011), vol. arXiv: 1101.0593 [hep-ph] (cit. on p. 67).
73. COIMBRA, RITA, MARCO O. P. SAMPAIO, and RUI SANTOS: ‘ScannerS: Constraining the phase diagram of a complex scalar singlet at the LHC’. *Eur. Phys. J.* (2013), vol. C73: p. 2428. arXiv: 1301.2599 [hep-ph] (cit. on pp. 68, 86).
74. FERREIRA, P. M., RENATO GUEDES, MARCO O. P. SAMPAIO, and RUI SANTOS: ‘Wrong sign and symmetric limits and non-decoupling in 2HDMs’. *JHEP* (2014), vol. 12: p. 067. arXiv: 1409.6723 [hep-ph] (cit. on pp. 68, 86).
75. COSTA, RAUL, MARGARETE MÜHLLEITNER, MARCO O. P. SAMPAIO, and RUI SANTOS: ‘Singlet Extensions of the Standard Model at LHC Run 2: Benchmarks and Comparison with the NMSSM’. *JHEP* (2016), vol. 06: p. 034. arXiv: 1512.05355 [hep-ph] (cit. on pp. 68, 86).
76. MÜHLLEITNER, MARGARETE, MARCO O. P. SAMPAIO, RUI SANTOS, and JONAS WITTBRODT: ‘The N2HDM under Theoretical and Experimental Scrutiny’. *JHEP* (2017), vol. 03: p. 094. arXiv: 1612.01309 [hep-ph] (cit. on pp. 68, 71, 86).
77. BECHTLE, PHILIP, OLIVER BREIN, SVEN HEINEMEYER, GEORG WEIGLEIN, and KARINA E. WILLIAMS: ‘HiggsBounds: Confronting Arbitrary Higgs Sectors with Exclusion Bounds from LEP and the Tevatron’. *Comput. Phys. Commun.* (2010), vol. 181: pp. 138–167. arXiv: 0811.4169 [hep-ph] (cit. on pp. 68, 86).
78. BECHTLE, PHILIP, OLIVER BREIN, SVEN HEINEMEYER, GEORG WEIGLEIN, and KARINA E. WILLIAMS: ‘HiggsBounds 2.0.0: Confronting Neutral and Charged Higgs Sector Predictions with Exclusion Bounds from LEP and the Tevatron’. *Comput. Phys. Commun.* (2011), vol. 182: pp. 2605–2631. arXiv: 1102.1898 [hep-ph] (cit. on pp. 68, 86).
79. BECHTLE, PHILIP, OLIVER BREIN, SVEN HEINEMEYER, OSCAR STÅL, TIM STEFANIAK, GEORG WEIGLEIN, and KARINA E. WILLIAMS: ‘HiggsBounds-4: Improved Tests of Extended Higgs Sectors against Exclusion Bounds from LEP, the Tevatron and the LHC’. *Eur. Phys. J. C* (2014), vol. 74(3): p. 2693. arXiv: 1311.0055 [hep-ph] (cit. on pp. 68, 86).
80. BECHTLE, PHILIP, SVEN HEINEMEYER, OSCAR STÅL, TIM STEFANIAK, and GEORG WEIGLEIN: ‘HiggsSignals: Confronting arbitrary Higgs sectors with measurements at the Tevatron and the LHC’. *Eur. Phys. J. C* (2014), vol. 74(2): p. 2711. arXiv: 1305.1933 [hep-ph] (cit. on pp. 68, 86).
81. AALBERS, J. et al.: ‘DARWIN: towards the ultimate dark matter detector’. *JCAP* (2016), vol. 11: p. 017. arXiv: 1606.07001 [astro-ph.IM] (cit. on p. 68).
82. GROSS, CHRISTIAN, OLEG LEBEDEV, and TAKASHI TOMA: ‘Cancellation Mechanism for Dark-Matter–Nucleon Interaction’. *Phys. Rev. Lett.* (2017), vol. 119(19): p. 191801. arXiv: 1708.02253 [hep-ph] (cit. on p. 72).
83. HABER, HOWARD E.: ‘Diagonalization of a 2×2 real symmetric matrix’. (2011), vol. URL: http://scipp.ucsc.edu/~haber/ph116A/diag2x2_11.pdf (cit. on p. 77).

-
84. ROMAO, JORGE C. and JOAO P. SILVA: ‘A resource for signs and Feynman diagrams of the Standard Model’. *Int. J. Mod. Phys.* (2012), vol. A27: p. 1230025. arXiv: 1209.6213 [hep-ph] (cit. on pp. 80, 81).
 85. HAHN, THOMAS: ‘Generating Feynman diagrams and amplitudes with FeynArts 3’. *Comput. Phys. Commun.* (2001), vol. 140: pp. 418–431. arXiv: hep-ph/0012260 [hep-ph] (cit. on p. 86).
 86. SHTABOVENKO, VLADYSLAV, ROLF MERTIG, and FREDERIK ORELLANA: ‘New Developments in FeynCalc 9.0’. *Comput. Phys. Commun.* (2016), vol. 207: pp. 432–444. arXiv: 1601.01167 [hep-ph] (cit. on p. 86).
 87. MERTIG, R., M. BOHM, and ANSGAR DENNER: ‘FEYN CALC: Computer algebraic calculation of Feynman amplitudes’. *Comput. Phys. Commun.* (1991), vol. 64: pp. 345–359 (cit. on p. 86).
 88. HAHN, T. and M. PEREZ-VICTORIA: ‘Automatized one loop calculations in four-dimensions and D-dimensions’. *Comput. Phys. Commun.* (1999), vol. 118: pp. 153–165. arXiv: hep-ph/9807565 [hep-ph] (cit. on p. 86).
 89. OLDENBORGH, G. J. van and J. A. M. VERMASEREN: ‘New algorithms for one-loop integrals’. *Zeitschrift für Physik C Particles and Fields* (Sept. 1990), vol. 46(3): pp. 425–437. URL: <https://doi.org/10.1007/BF01621031> (cit. on p. 86).
 90. PATEL, HIREN H.: ‘Package-X: A Mathematica package for the analytic calculation of one-loop integrals’. *Comput. Phys. Commun.* (2015), vol. 197: pp. 276–290. arXiv: 1503.01469 [hep-ph] (cit. on p. 86).
 91. STAUB, F.: ‘SARAH’. (2008), vol. arXiv: 0806.0538 [hep-ph] (cit. on p. 86).
 92. ELLIS, JOSHUA: ‘TikZ-Feynman: Feynman diagrams with TikZ’. *Comput. Phys. Commun.* (2017), vol. 210: pp. 103–123. arXiv: 1601.05437 [hep-ph] (cit. on p. 86).

Acknowledgements

Finally, I want to give thanks to everybody who supported me in accomplishing my master thesis.

- I want to thank Prof. Dr. M. Margarete Mühlleitner for giving me the opportunity to work on this interesting topic, for the kind integration into her workgroup and for the detailed feedback regarding my thesis.
- I also thank Prof. Dr. U. Nierste for agreeing to be the second reviewer of my master thesis.
- Special thanks go to Jonas Müller for the great, friendly and straightforward collaboration and for him being (or at least seeming) never annoyed when he took the time to discuss and answer my questions. I can only wish the future generations of bachelor and master students to get an advisor like him.
- I also want to thank Dr. Philipp Basler and Dr. Jonas Wittbrodt for their substantial assistance in setting up SCANNERS-2 for the DCxSM.
- Thanks to Martin Gabelmann who did more than once save my day by fixing a stubborn IT issue.
- I thank the members of the Dark Matter workgroup, Prof. Dr. Rui Santos, Dr. Shruti Patel and Dr. Seraina Glaus, for the helpful discussions in our regular meeting.
- Thanks to all members of the Institute of Theoretical Physics for providing a very friendly and enjoyable atmosphere, which made me look forward to go to work (almost) every morning.
- Thanks to Belinda Benz and Philipp Löffler for proof-reading this thesis. Moreover, a special thanks goes of course to Belinda for the countless discussions on Quantum Field Theory and her moral support which significantly contributed to the successful completion of this thesis.
- Last but definitely not least I want to thank my parents, Claudia and Adrian Römer, for giving me the possibility to study physics. Their almost unconditional support for anything I do is absolutely worth its weight in gold.